iScience

CellPress

Article

Seawater-Mediated Solar-to-Sodium Conversion by Bismuth Vanadate Photoanode- Photovoltaic Tandem Cell: Solar Rechargeable Seawater Battery

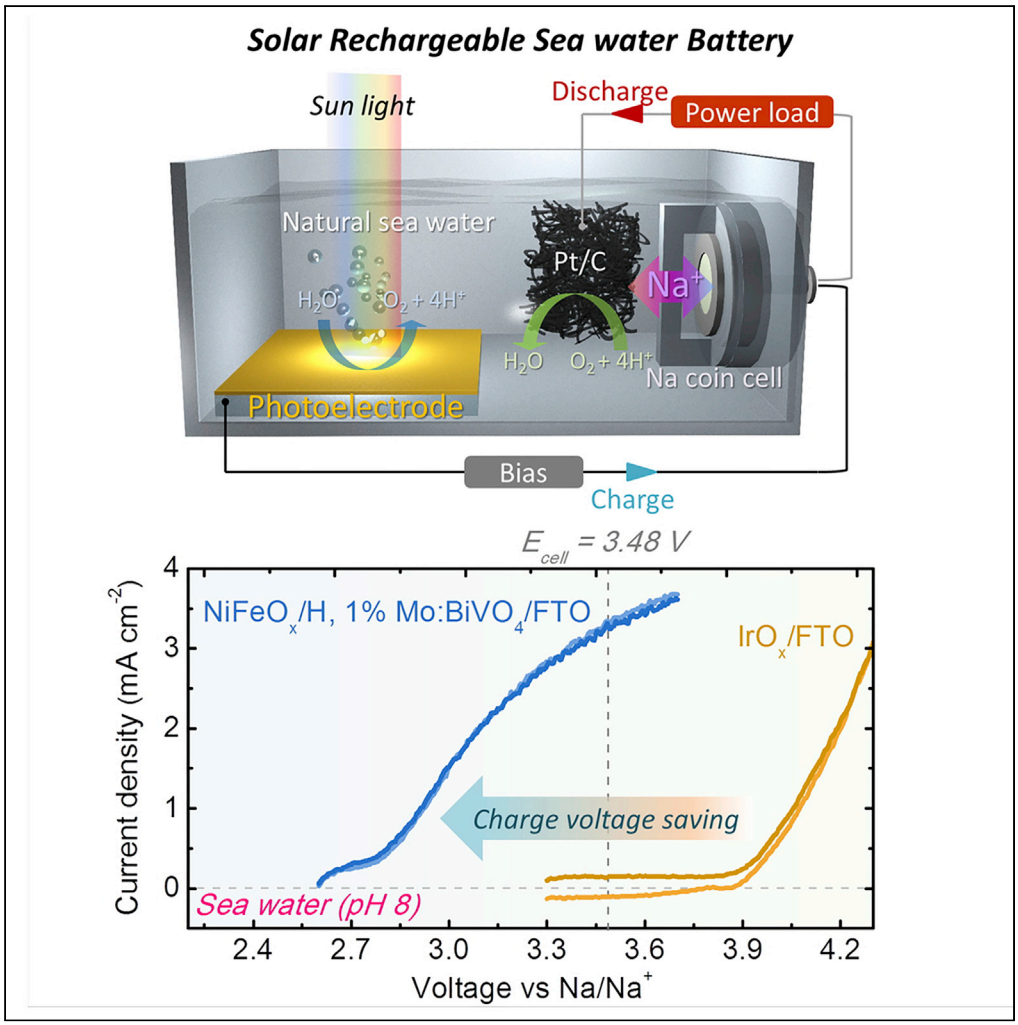

Jin Hyun Kim, Soo Min Hwang, Inchan Hwang, ..., Kwanyong Seo, Youngsik Kim, Jae Sung Lee

kihi6783@unist.ac.kr (J.H.K.)
ykim@unist.ac.kr (Y.K.)
jlee1234@unist.ac.kr (J.S.L.)

HIGHLIGHTS

Solar rechargeable battery using natural seawater as a medium was realized

Solar charge was achieved by metal oxide-based photoelectrodes, especially $BiVO_4$

$BiVO_4$-c-Si tandem cell achieved unbiased charge with a high efficiency up to 8%

Kim et al., iScience 19, 232–243
September 27, 2019
https://doi.org/10.1016/j.isci.2019.07.024

iScience

CellPress

Article

Seawater-Mediated Solar-to-Sodium Conversion by Bismuth Vanadate Photoanode- Photovoltaic Tandem Cell: Solar Rechargeable Seawater Battery

Jin Hyun Kim,[1,4,*] Soo Min Hwang,[1,4] Inchan Hwang,[1] Jinhyup Han,[1] Jeong Hun Kim,[1] Yim Hyun Jo,[2] Kwanyong Seo,[1] Youngsik Kim,[1,3,*] and Jae Sung Lee[1,5,*]

SUMMARY

Conversion of sunlight to chemical energy based on photoelectrochemical (PEC) processes has been considered as a promising strategy for solar energy harvesting. Here, we propose a novel platform that converts solar energy into sodium (Na) as a solid-state solar fuel via the PEC oxidation of natural seawater, for which a Na ion-selective ceramic membrane is employed together with photoelectrode (PE)-photovoltaic (PV) tandem cell. Using an elaborately modified bismuth vanadate-based PE in tandem with crystalline silicon PV, we demonstrate unassisted solar-to-Na conversion (equivalent to solar charge of seawater battery) with an unprecedentedly high efficiency of 8% (expected operating point under 1 sun) and measured operation efficiency of 5.7% (0.2 sun) and long-term stability, suggesting a new benchmark for low-cost, efficient, and scalable solid solar fuel production. The sodium turns easily into electricity on demand making the device a nature-friendly, monolithic solar rechargeable seawater battery.

INTRODUCTION

Utilization of abundant (23,000 TW year^{-1}) solar energy in an efficient, cost-effective manner is essential to leapfrog fossil fuel technologies and secure sustainable, climate-friendly future of our society (Cook et al., 2010; Kim et al., 2019; Lewis, 2016; Roger et al., 2017; Seitz et al., 2014). Yet its intermittent feature poses a huge challenge toward practical, large-scale dissemination (Kurtz et al., 2017; Pellow et al., 2015; Sivula and van de Krol, 2016; Yang et al., 2011). In this regard, converting solar energy into easily storable chemical energy is the most effective strategy as adeptly exemplified by the natural photosynthesis that captures sunlight and stores it in chemical bonds. Similarly, artificial photosynthetic systems include production of H_2 by photoelectrochemical (PEC) water splitting and of carbon-based chemicals by CO_2 reduction (Blankenship et al., 2011; Montoya et al., 2016; Nocera, 2017; Sivula and van de Krol, 2016). Such solar conversion to gaseous or liquid fuels production at a grid scale, however, still requires further advancements in solar-to-chemical conversion efficiencies (η_{STC}), device stability, and cost (Montoya et al., 2016; Nocera, 2017; Pellow et al., 2015; Seitz et al., 2014). In addition, the effective storage of gaseous fuels like H_2 is rather difficult.

Alternatively, solar-driven electric energy can be stored as chemical energy in electrochemical energy storage (EES) systems, such as rechargeable batteries or supercapacitors, by connecting with photovoltaic (PV) devices (Um et al., 2017; Xu et al., 2015a, 2015b). This simple method, however, has critical drawbacks, such as the high cost stemming from two separate modules and the unavoidable loss of overall energy conversion efficiency (Roger et al., 2017; Xu et al., 2015a; Yang et al., 2011). Recently, solar rechargeable cells (SRCs), which integrate a PEC cell and an EES cell into a single device, have been revived as a promising means for sunlight utilization (Cheng et al., 2017; Li et al., 2016a; Li et al., 2016c; Liao et al., 2016; Liu et al., 2016; Nikiforidis et al., 2016). The photo-generated electricity from a PEC component is stored *in situ* in chemical bonds within an EES component (*photo-charging*), and the chemical energy can be utilized to generate electric power on demand (*discharging*). Most of the reported SRCs have employed dissolved redox-active species, such as iodine, bromine, vanadium, or sulfur as a redox mediator due to their fast redox reaction kinetics (Li et al., 2017; Yu et al., 2016), with the photoelectrodes (PEs) immersed in electrolytes. More recently, quinone-based redox flow batteries (RFBs) charged by dual PEs of p/n-Si (Li et al., 2016a; Liao et al., 2016) or Ta_3N_5 combined with GaN/p-Si (Cheng et al., 2017) have demonstrated highly efficient solar-to-chemical energy conversion. Notwithstanding, the use of highly corrosive acidic electrolytes and expensive membranes or the environmental impact (toxicity) of redox couples themselves (e.g., bromine)

[1]Department of Energy Engineering, School of Energy and Chemical Engineering, Ulsan National Institute of Science & Technology (UNIST), Ulsan 44919, Republic of Korea

[2]Advanced Center for Energy, Korea Institute of Energy Research (KIER), Ulsan 44919, Republic of Korea

[3]Energy Materials and Devices Lab, 4TOONE Corporation, 50 UNIST-gil, Ulsan 44919, Republic of Korea

[4]These authors contributed equally

[5]Lead Contact

*Correspondence: kihi6783@unist.ac.kr (J.H.K.), ykim@unist.ac.kr (Y.K.), jlee1234@unist.ac.kr (J.S.L.)

https://doi.org/10.1016/j.isci.2019.07.024

still remain to be resolved for large-scale deployment. In addition, such SRCs including RFBs typically have a low discharge voltage less than 1.5 V, because of small difference in the formal potentials between redox-active anolyte and catholyte (Azevedo et al., 2016; Cheng et al., 2017; Li et al., 2016a; Liao et al., 2016).

Here, we report a novel approach to solar fuel production, where earth-abundant seawater is utilized as the infinite medium to store the sunlight energy in chemical bonds of highly electropositive sodium (Na) metal (−2.71 V versus standard hydrogen electrode), which is reduced from Na^+ ions present in seawater (~0.5 M), as a result of solar-driven PEC seawater splitting. To this end, we design a monolithically integrated system, named *solar rechargeable seawater battery* that employs a Na superionic conducting ceramic membrane (NASICON, $Na_3Zr_2Si_2PO_{12}$) to separate a charge storage electrode (Na metal anode) in an organic electrolyte from a PE and a cathode immersed in seawater while allowing only Na-ion transport between the two compartments, as illustrated in Figure 1A.

We have developed a cost-effective and ecofriendly seawater battery in the last few years (Abirami et al., 2016; Kim et al., 2014; Kim et al., 2016c). Like the discharge process of a typical secondary battery, the chemical energy stored in Na(s) turns to electricity.

Charge:

$$\mathrm{OER}: 2H_2O(l) \xrightarrow{\text{By PA or OEC}} 4H^+(aq) + O_2(aq) + 4e^-;\ E = 1.23\mathrm{V}\ \textit{vs.}\ \mathrm{RHE}$$
$$\mathrm{Na\ storage}: 4Na^+(aq) + 4e^- \rightarrow 4Na(s);\ E = -2.25\mathrm{V}\ \textit{vs.}\ \mathrm{RHE}$$

Discharge:

$$\mathrm{Na\ release}: 4Na(s) \rightarrow 4Na^+(aq) + 4e^-;\ E = -2.25\mathrm{V}\ \textit{vs.}\ \mathrm{RHE}$$
$$\mathrm{ORR}: 4H^+(aq) + O_2(aq) + 4e^- \xrightarrow{\text{By Pt/C}} 2H_2O(l) + 4e^-;\ E = 1.23\mathrm{V}\ \textit{vs.}\ \mathrm{RHE}$$

Overall reaction for charge and discharge will be expressed as:

$$4Na(s) + O_2(aq) + 4H^+(aq) \underset{\text{charge}}{\overset{\text{discharge}}{\rightleftharpoons}} 4Na^+(aq) + 2H_2O(l);\ E_{cell} = 3.48\mathrm{V}\ \textit{vs.}\ Na/Na^+$$
$$(\textit{path 1 or 2})$$

Specifically, the Na metal anode is oxidized to Na^+ ions, which are then transported into seawater through the NASICON membrane, whereas the reduction reaction of dissolved oxygen occurs on the cathode in seawater, powering an external load. On the other hand, the cell can be charged at a significantly reduced voltage by applying a suitable PE that enables the PEC seawater oxidation, when compared with typical electric charging based on seawater electrolysis. The energy diagram of the photo-charging process of the cell is depicted in Figure 1B, where an oxygen-evolving catalyst (OEC)-loaded $BiVO_4$ is exemplified as a PE for our scheme. We have picked $BiVO_4$ to be the major model PE for this work owing to its superior performance among metal oxide-based photoanodes (Kim and Lee, 2019). Upon illumination, photons (λ < 516 nm) captured by $BiVO_4$ generate electron-hole pairs. The photo-generated holes in the valence band (VB) are transferred to the PE-seawater junction, oxidizing seawater to O_2. Meanwhile, the electrons excited to the conduction band (CB) flow toward the anode through the external circuit, which decreases the potential required for Na^+ reduction following Na ion-transport from the seawater into the anode, as much as the energy difference between the Fermi level of the PE (~0.05 V_{RHE}) and the redox potential of O_2/H_2O (E_{O_2/H_2O}) in seawater (1.23 V_{RHE}).

Thus the photo-driven process at the PE-seawater interface enables the cell to be charged at ~2.25 V versus Na/Na^+, resulting in a theoretical potential gain of ~1.23 V (~35%). Furthermore, we demonstrate spontaneous, unbiased photo-charging of the device with $BiVO_4$-based PE-c-Si PV tandem cell, achieving a record-high η_{STC} of up to 8% under 1 sun illumination, which set a new benchmark for solar-to-chemical (Na) energy conversion. To set the scope of this work, previously reported SRCs and their performance in expected voltage saving (V_{saved}) versus redox potential (E_{redox}) are compared with ours in Figure 1C and Table S1.

RESULTS

Selection and Analysis of Photoanodes for PEC Seawater Splitting

We first tested the PEC seawater splitting activity of cheap and environmentally benign metal oxide semiconductor films, such as TiO_2, WO_3, Fe_2O_3, and $BiVO_4$, as PE candidates for efficient photolysis of seawater

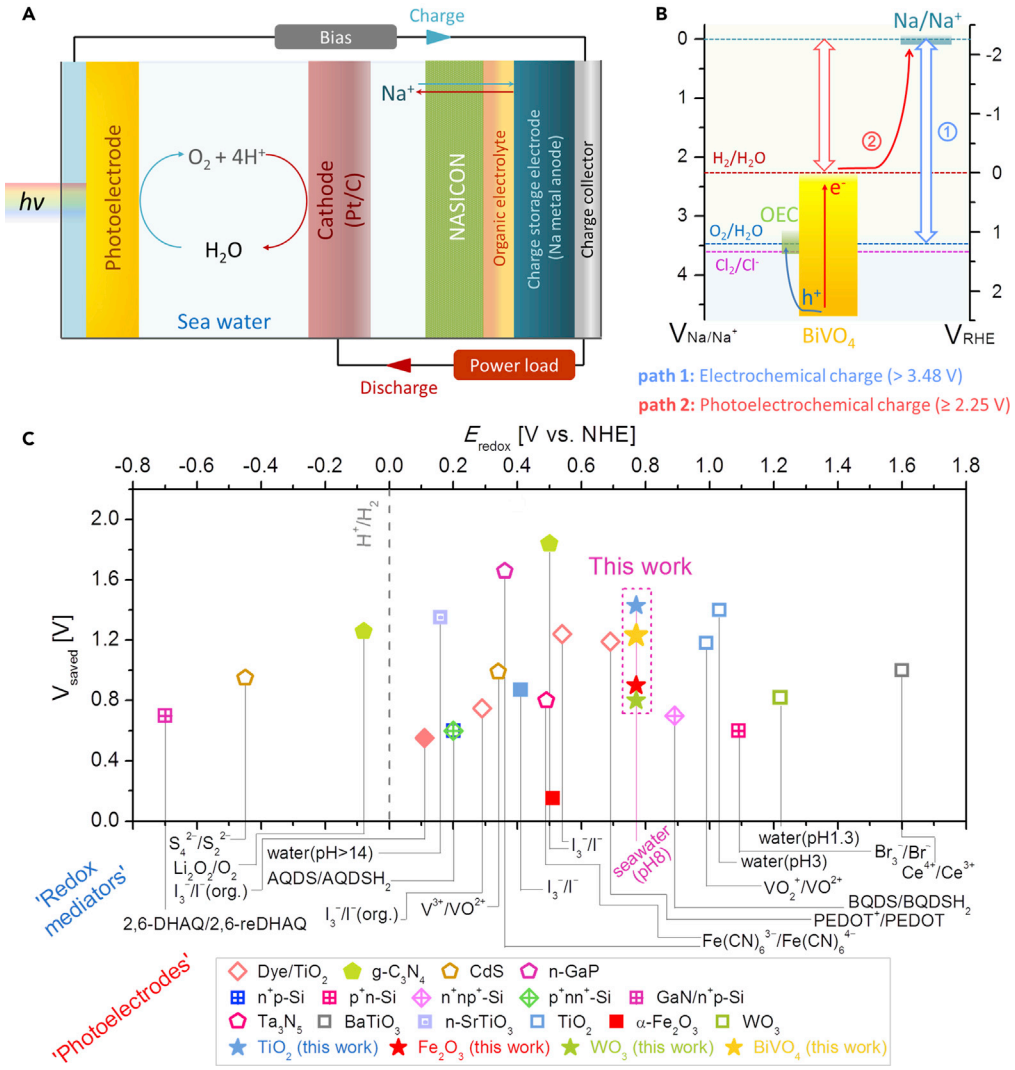

Figure 1. Cell Configuration and Photo-charging Process of the Solar Seawater Battery

(A) The cell structure of a solar rechargeable seawater battery, which employs a NASICON ceramic membrane to separate a charge storage electrode (Na metal anode) from a photoelectrode (PE) and a cathode immersed in seawater.

(B) Energy diagram of the photo-charging process, where OEC-loaded $BiVO_4$ PE is employed for solar seawater oxidation at the cathode compartment. The energy level is expressed with two different scales relative to reversible hydrogen electrode (RHE) of seawater (pH~8) and the redox potential of Na/Na^+. The PEC seawater splitting on the PE significantly reduces the potential required for battery charging (path 1 versus path 2).

(C) Redox potential (E_{redox})-voltage saved (V_{saved}) plot of various types of solar rechargeable batteries using redox mediators from literatures. The V_{saved} was calculated by subtracting the conduction band edge (E_{CB}/e) of photoelectrodes from the E_{redox} of redox mediators.

as described in Supplemental Information, Figures S1–S5 and 2. These materials have been extensively studied for PEC splitting of water, but rarely of seawater.

The J-V curves of the five PEs (together with the Pt rod electrode) relative to the Pt counterelectrode (left) and the Na counterelectrode (seawater cell; right) are shown in Figure 2A. The current density at 3.48 V (versus Na/Na^+) was 3.65 mA/cm^2 for $NiFeO_x$/H, 1% Mo:$BiVO_4$, 0.78 mA/cm^2 for H, 1% Mo:$BiVO_4$, 0.55 mA/cm^2 for TiO_2, 0.46 mA/cm^2 for WO_3, and 0.11 mA/cm^2 for Fe_2O_3. We tested galvanostatic photo-charging of the battery with the PEs at currents of 0.01 mA and 0.1 mA upon 1 sun illumination (Figure 2B). The actual charge voltages of these PEs are measured to be 3.32 V for Fe_2O_3, 3.05 V for WO_3, 2.70 V for TiO_2 and H, 1% Mo:$BiVO_4$, and 2.62 V for $NiFeO_x$/H, 1% Mo:$BiVO_4$ at a low current density of 0.05 mA/cm^2; the

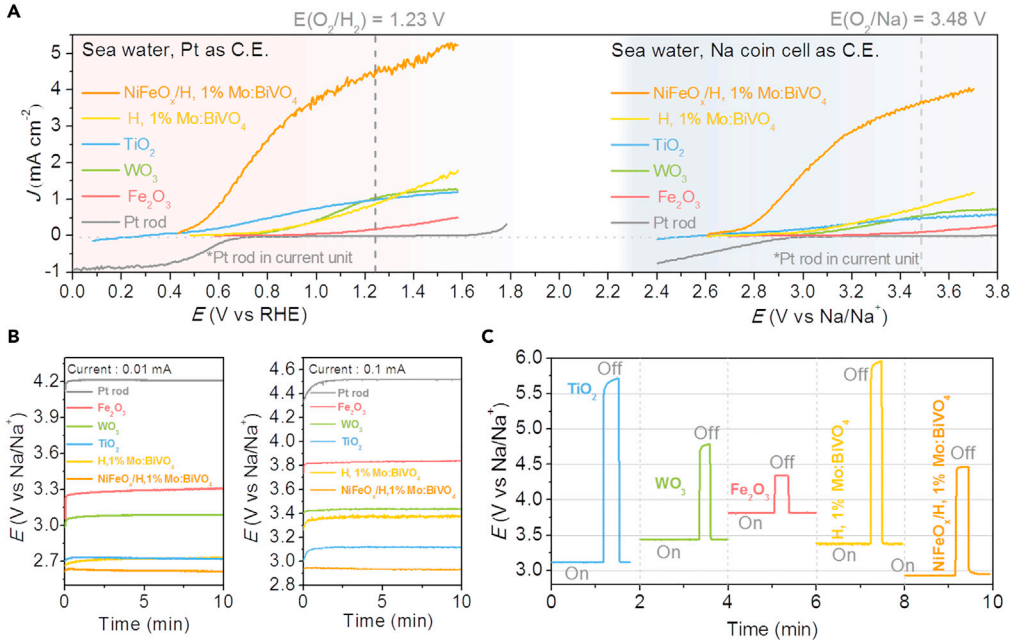

Figure 2. Performance of Semiconductor Oxide Photoelectrodes (TiO_2, WO_3, Fe_2O_3, $BiVO_4$) for Seawater Battery

(A–C) (A) J-V curves of TiO_2, WO_3, Fe_2O_3, and H, 1% Mo:$BiVO_4$ photoelectrode in three electrode configurations for Pt metal rod (left side) and Na coin cell as counterelectrode (two-electrode system, right side); (B) galvanostatic photo-charging at 0.01 and 0.1 mA for the photoelectrodes and Pt rod; (C) J-t curves for photo-charge at 0.1 mA (per electrode) with and without light illumination (denoted as on and off). The geometric area of photoelectrodes was 0.20 cm^2, and the Pt rod was 3 cm in length.

theoretical potential requirement is considered as at least 3.68 V (a minimum overpotential of 0.2 V assumed) to achieve photo-charge, which gives a potential saving of 0.36–1.06 V by using a light absorber. The photo-charge at a higher current density of 0.5 mA/cm^2 (0.1 mA per 0.20 cm^2PE) requires a higher potential, although the value is still mostly lower than 3.68–3.8 V for Fe_2O_3, 3.35 V for WO_3, 3.11 V for TiO_2, 3.11 V for H, 1% Mo:$BiVO_4$, and 2.91 V for $NiFeO_x$/H, 1% Mo:$BiVO_4$. The on-off tests clearly showed that the potential saving was achieved by a light-induced process on the PEs (Figure 2C).

Compared with previous reports on the photo-charge of redox couple-based SRCs (only 0.001–0.01 mA/cm^2) (Li et al., 2016b, 2017; Yu et al., 2014), our system with the $NiFeO_x$/H, 1% Mo:$BiVO_4$ PE showed significantly higher photocurrent densities (~3 mA/cm^2). In addition, the redox mediator (O_2/H_2O) of our system (pH-neutral natural seawater) (Li et al., 2017) is nature friendly compared with existing SRCs, such as I^-/I^{3-} (light absorber—N179/TiO_2, Yu et al., 2014; TiO_2, Li et al., 2016b; Fe_2O_3, Nikiforidis et al., 2016) and VO_2^+/VO^{2+} (light absorber—CdS/CdSe, Azevedo et al., 2016). Previous demonstrations of O_2/H_2O redox-based SRCs achieved modest potential savings, but TiO_2 (3.2–3.0 eV, J_{charge} ~0.01 mA/cm^2) (Kim et al., 2016a) and C_3N_4 (2.7 eV, J_{charge} ~ 0.05 mA/cm^2) (Liu et al., 2016) cannot achieve such a high current density as we did with $BiVO_4$ (2.4 eV, J_{charge} >1.0–3.0 mA/cm^2). Another important aspect of our $BiVO_4$ PE is transparency that other previous studies could not have (Li et al., 2017; Liu et al., 2016). Above its practical optical band gap (indirect, 2.4 eV, 516 nm), it has near 75% transmittance (Figure S1). Such merit benefits construction of a PE-PV tandem device for unbiased photo-charge of the system, which is demonstrated in a later section. Quinone redox batteries photo-charged by Si (Li et al., 2016a) and Ta_3N_5 PEs (Cheng et al., 2017) with current densities of ~10 mA/cm^2 only showed superior performance to our system (~3 mA/cm^2), but their systems require high alkalinity of the electrolyte.

Among the PEs tested, elaborately modified $BiVO_4$ exhibited the best performance in J-V curves of PEC seawater splitting and seawater battery charge (Figure 2A) and galvanostatic photo-charging (Figures 2B and 2C), and thus naturally became our choice for the PE. For its fabrication, a modified metal-organic decomposition method was employed to obtain 1 atom % Mo-doped $BiVO_4$ film on F-doped SnO_2 (FTO) glass, which was further treated with H_2 generated by $NaBH_4$ decomposition to

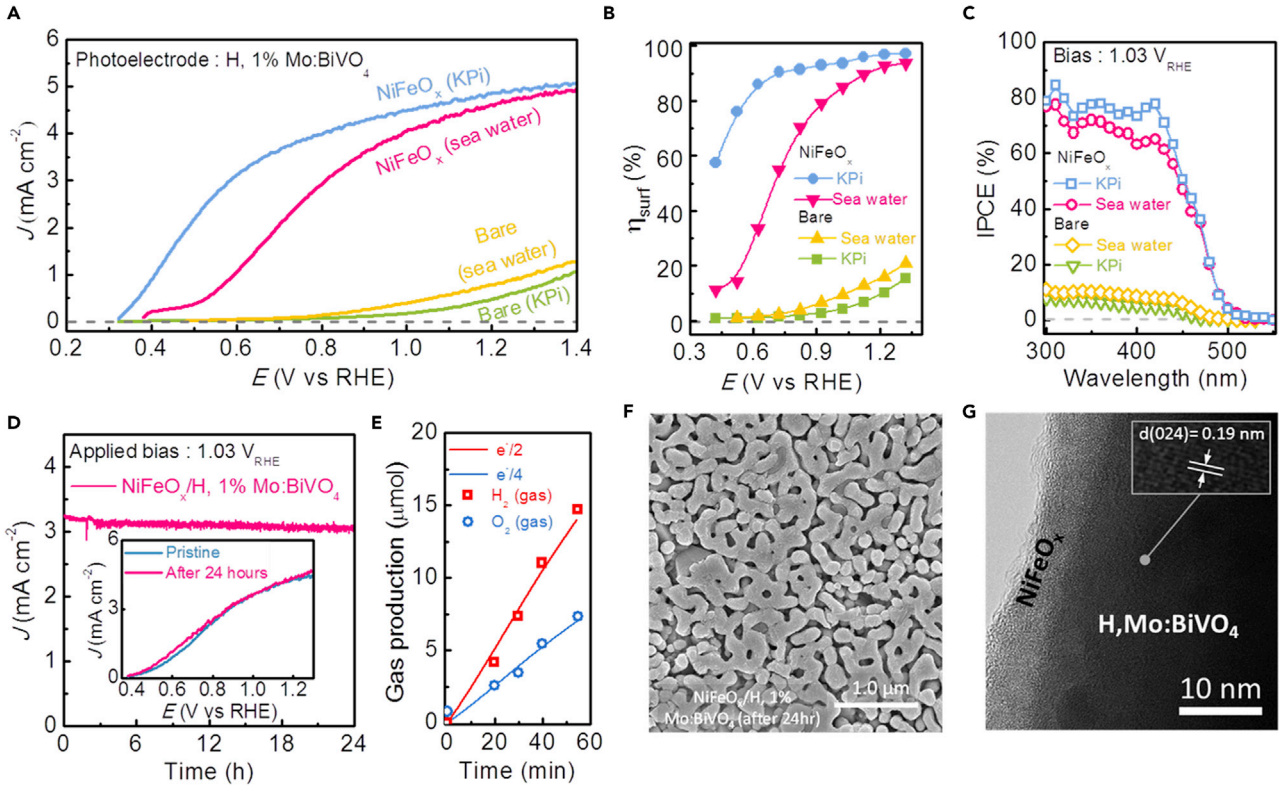

Figure 3. PEC Performance of $NiFeO_x/BiVO_4$ PE under Simulated Sunlight for Seawater Splitting

(A) J-V curves of $BiVO_4$ PE with and without the $NiFeO_x$ co-catalyst in KPi buffer (pH 7.0) and natural seawater (pH 8.0).

(B and C) Corresponding (B) surface charge separation efficiencies (η_{surf}) and (C) IPCE values.

(D) Photocurrent generation at a constant potential of 1.03 V_{RHE}. The inset shows the J-V curves before and after the stability test for 24 h.

(E) Gas evolution in natural seawater of a PEC cell composed of the $BiVO_4$ PE and Pt rod counterelectrode at an applied bias of 0.9 V_{RHE} (geometric area of the PE = 0.25 cm^2).

(F and G) (F) A scanning electron micrograph and (G) a transmission electron microscopic image after the stability test.

improve the bulk charge transfer characteristics. The extensive characterization data of the H, 1% Mo:$BiVO_4$ PE including ultraviolet-visible and X-ray diffraction are available in our recent works (Kim et al., 2016b; Pan et al., 2018). Furthermore, we loaded $NiFeO_x$ OEC on the $BiVO_4$ PE by photo-assisted electrodeposition. Electron microscopic images revealed that $NiFeO_x$-loaded, hydrogen-treated, Mo-doped $BiVO_4$ (denoted as $NiFeO_x/BiVO_4$ or $NiFeO_x$/H, 1% Mo:$BiVO_4$) PE featured a porous morphology consisting of connected particles (100–200 nm), on which ~5-nm-thick $NiFeO_x$ layer was formed (Figures S5 and S6).

The basic driving force of the solar charging is PEC oxidation of seawater by a photoanode,

$$2H_2O + 4h_{vb}^+ \rightarrow O_2 + 4H^+$$

where h_{vb}^+ is the hole generated in the VB of the semiconductor photoanode upon light absorption. The performance of the $NiFeO_x/BiVO_4$ PE for PEC seawater splitting under simulated AM 1.5G sunlight (100 $mWcm^{-1}$) is shown in Figure 3. The $NiFeO_x/BiVO_4$ PE showed a reduced onset potential by 0.35 V_{RHE} compared with the bare $BiVO_4$ PE in seawater. Although the $NiFeO_x/BiVO_4$ PE exhibited a slightly lower PEC performance in seawater (4.8 mA cm^{-2} at 1.23 V_{RHE}) than in 0.1 M potassium phosphate (KPi), a typical electrolyte for water splitting (5.0 mA cm^{-2}) (Figures 3A–3C), these values of current density are still comparable to those of reported benchmark metal oxide light absorbers (Kim et al., 2015; Lee and Choi, 2017; Sivula and van de Krol, 2016). It is noteworthy that the current densities recorded by our $NiFeO_x/BiVO_4$ are actually the best ever reported for seawater splitting, surpassing the previous record of 2.16 mA cm^{-2} by RhO_x/3% Mo:$BiVO_4$ at 1.0 V_{RHE} (Luo et al., 2011). The $NiFeO_x/BiVO_4$ PE exhibited

a stable performance for 24 h producing O_2 and H_2 gases with a molar ratio of 1:2 (Figures 3D and 3E), which is comparable to previous best $BiVO_4$ PEs operated in KPi buffer for 30–50 h (Kim and Choi, 2014; Kim et al., 2015). No notable change in the morphology was found after PEC operation for 24 h (Figures 3F, 3G, S2, and S3). The energy-dispersive X-ray and X-ray photoelectron spectroscopic data indicated that the chemical state of $NiFeO_x$ is in an oxyhydroxide form, i.e., $NiFeO_xH_y$, and oxidation states of all elements in $NiFeO_x/BiVO_4$ PE remain unaltered throughout the PEC reactions (Figures S4–S6, Table S2).

We performed controlled experiments to study the effect of electrolyte components on the PEC performance of the $NiFeO_x/BiVO_4$ PE by varying the concentration of NaCl or Na_2SO_4, both of which are known to be rather less effective in PEC water oxidation (Figures S7 and S8) (Shinagawa et al., 2017). To understand better this effect of electrolyte and the role of $NiFeO_x$ OEC overlayer, photoelectrochemical impedance spectroscopy (PEIS) was performed in Figures S9–S11. Loading OEC can provide a higher quasi-Fermi level (|Fermi level – quasi-Fermi level| = photovoltage) or a higher photovoltage by passivating defective surface states and providing alternative pathway for hole transfer through OEC instead of surface of the semiconductor, which tends to become recombination centers for holes. Maximum capacitance for surface states (C_{ss}) and minimum resistance at semiconductor||electrolyte interface (R_{CT}) determined by PEIS can be indicators that show how hole transfer dynamics changes with OEC loading (Wang et al., 2016). With OEC applied, surface state shifts closer to the Fermi level of $BiVO_4$ (Figure S10) by the "passivation effect" and the potential difference between Fermi level and quasi-Fermi level gets wider (Ma et al., 2014, 2016). Also, R_{CT} values throughout the anodic potential region markedly decrease owing to reduced recombination and facile hole transfer to electrolyte (Figures S10A versus S10C). The maximal C_{ss} increases because the $NiFeO_x$ could function as a hole storage layer as well as provide alternative active sites for water oxidation, therefore reducing the overpotential compared with the bare $BiVO_4$ photoanode. In seawater, potentials for maximum C_{ss} and lowest R_{CT} are all anodically shifted by ~0.2 V (Figures S10B versus S10D), which is equivalent to the extent that J-V curve shifts relative to those in KPi. However, there is a noticeable difference in terms of the position of maximum C_{ss} and minimum R_{CT} for KPi (potentials of maximum Css: < 0.3 V_{RHE}, minimum R_{CT}: 0.45 V_{RHE}) and seawater (potentials of max. Css: 0.45 V_{RHE}, min. R_{CT}: 0.66 V_{RHE}), which indicates that hole transfer from $NiFeO_x$ requires a higher potential (by 0.2 V) and is more sluggish in seawater. Interestingly, above 0.6–0.7 V_{RHE}, C_{SS} and R_{CT} values are almost the same for $NiFeO_x/BiVO_4$ both in KPi and seawater, which indicates that enough potential is applied for $NiFeO_x/BiVO_4$ to drive water oxidation.

This rather unexpected behavior should be explained with another observation—transient photocurrent (TPC) appears in the low-bias region for $NiFeO_x/BiVO_4$. The "spike" appears when hole resides in excess on the surface of semiconductor, indicating a sluggish hole transfer from semiconductor to electrolyte and a large amount of holes residing at this interface (Liu et al., 2014). In Figures S8A and S8B, TPC appearing at 0.4 V_{RHE} is minute and almost the same for $BiVO_4$ in KPi and seawater, but a very large TPC appears for $NiFeO_x/BiVO_4$ only in seawater. This suggests that seawater affects the efficacy of $NiFeO_x$ on $BiVO_4$ and the effect is much more dominant at low biases (0.3–0.6 V_{RHE}) than at high biases (above 0.8 V_{RHE}), which is consistent with the onset potential of bare $BiVO_4$ (~0.8 V_{RHE}). Thus, for $NiFeO_x$, hole transfer at low biases is more sluggish in seawater than KPi. From PEIS analysis, the hole storage capability and the surface impedance when hole transfer is initiated are almost the same, thus the characteristic of $NiFeO_x$ itself is unchanged in different electrolytes. However, hole transfer at $NiFeO_x$||electrolyte depends on the electrolyte, i.e., KPi is better than seawater in water oxidation kinetics and has a dominant effect in the low-bias region.

The above considerations have been presented schematically in Figure S11. For bare $BiVO_4$, electrolytes of KPi and seawater bring almost no difference in J-V curves, capacitance, or impedance. However, for $NiFeO_x/BiVO_4$, a large difference in the efficacy of the co-catalyst is in the low-bias region. Thus for the case of KPi, hole transfer from $NiFeO_x$ to electrolyte is facile throughout the bias region (Figure S11C). In seawater, $BiVO_4$ itself cannot participate in direct hole transfer from $BiVO_4$ to the electrolyte, but $NiFeO_x$ instead takes holes and transfers them to electrolyte, although it is more sluggish than in KPi. However, when a high bias is applied, direct hole transfer from $BiVO_4$ to electrolyte is also possible (Figure S11D).

Photoelectrode-Driven Solar Rechargeable Seawater Battery

The developed PE is now applied to solar charging of the seawater battery. In Figure 4A, we examined photo-charge of the solar seawater battery (picture images in Figure S12) by employing the optimized

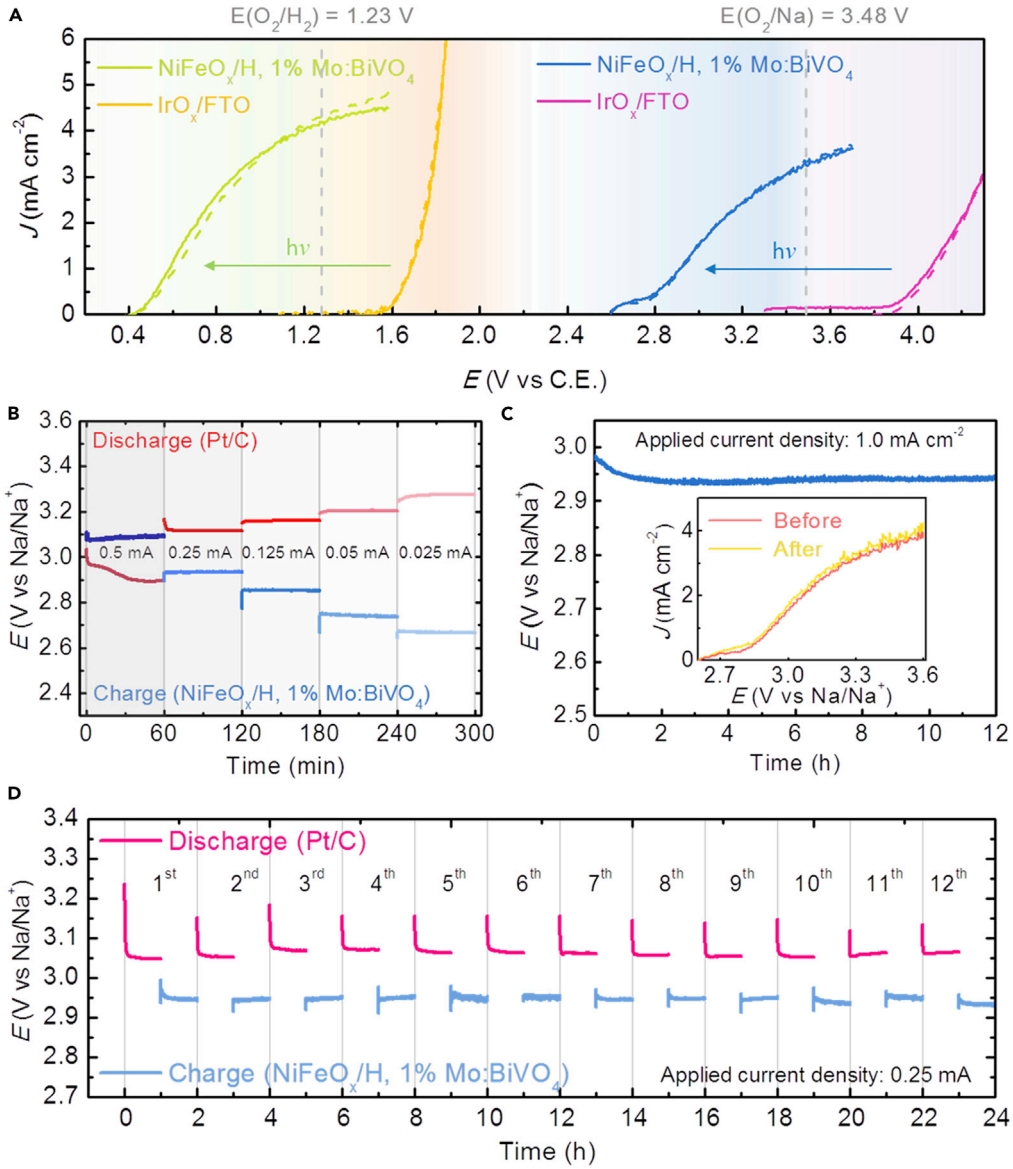

Figure 4. Photo-charge Performance of the Solar Seawater Battery with the $NiFeO_x/BiVO_4$ Photoelectrode

(A) J-V curves of three-electrode configuration with a Pt rod counterelectrode and two-electrode configuration (seawater cell) with a Na counterelectrode. Dotted curves are for backward bias scanning, and the vertical lines indicate the theoretical potential of water oxidation versus reversible hydrogen electrode and $E(Na/Na^+)$.

(B) Rate capability for photo-charging and discharging (using a Pt/C-coated cathode of 1.0 cm^2) at different currents of 0.025–0.5 mA.

(C) Long-term stability of the solar seawater battery during photo-charging at a current density of 1.0 mA cm^{-2}; the inset shows J-V curves before and after the test.

(D) Cycling performance at a current of 0.25 mA; a photo-charge current (+0.25 mA per 0.25 cm^2) and a discharge current (−0.25 mA per 1.0 cm^2).

$NiFeO_x/BiVO_4$ PE in comparison with a well-known OEC, IrO_x/FTO without light absorber (Figure S8). The IrO_x/FTO showed an onset potential of 1.55 V_{RHE} for the electrochemical seawater splitting and of 3.87 V versus Na/Na^+ for Na^+ reduction in the seawater cell. On the other hand, the photo-driven oxygen evolution reaction on the optimized $NiFeO_x/BiVO_4$ PE in seawater started at 0.35 V_{RHE} for water splitting and at 2.55 V versus Na/Na^+ for Na reduction. Although the onset potential (2.55 V) for charging the solar-seawater cell was a little larger than the value expected from the CB potential of $BiVO_4$ (~2.25 V), the

$BiVO_4$ PE clearly reduced the potential required for charging, resulting in almost ~1.3 V of potential saving compared with IrO_x/FTO, which was comparable to the theoretical potential difference (~1.28 V) between the flat band potential (E_{FB}) of the PE and the E_{O_2/H_2O} in seawater. It also represents the largest value among the cheap and stable metal oxide-based light absorbers reported in the literature, and is comparable to those of expensive and unstable CdTe or GaAs (Mayer, 2017).

The galvanostatic photo-charge and discharge were tested at different currents for 1 h each in Figure 4B, where the discharge process was performed using a 20 wt. % Pt/C-coated carbon electrode (see Methods). Discharge voltages of 3.27–2.89 V were measured for 0.025–0.5 mA of currents, and photo-charge voltages of 2.67–3.09 V at 0.025–0.5 mA of electric charge currents. It should be noted that the charge voltage for our solar rechargeable seawater battery was lower than that of the discharge voltage at current conditions below 0.5 mA, owing to the solar-driven seawater oxidation process by the PE, achieving apparent voltage efficiencies ($V_{discharge}/V_{charge}$) of 106%–122% unlike usual batteries, for which $V_{discharge}$ is always smaller than V_{charge}. The photo-charge uses solar energy to earn such a voltage increase to the extent of "potential saving" as described already.

The long-term photo-charging stability of the solar seawater cell with the $BiVO_4$ PE was evaluated at 1.0 mA cm^{-2}. As shown in Figure 4C, following an initial small decrease of the photo-charge voltage, it remained at ~2.95 V over 12 h without any appreciable decay. The J-V curves of the $NiFeO_x/BiVO_4$ PE also remained unchanged before and after the stability test (the inset). We further examined photo-charge/discharge cycling performance of the cell at a current of 0.25 mA for 1 h each (Figure 4D). The cell cycled in a stable manner with a photo-charge voltage of ~2.95 V and a discharge voltage of ~3.12 V for 12 cycles (total 24 h), showing an average voltage efficiency of 106%. This indicates that our $NiFeO_x/BiVO_4$ PE could achieve stable solar charge of the seawater battery with immensely increased voltage efficiency relative to usual electric charge, demonstrating an efficient solar-to-Na conversion.

The sunlight intensity is a critical parameter that affects the performance of PE, and thus, we investigated the effect of light intensity by varying it from 0.1 to 2.0 sun (Figure S13). For practical application of solar-seawater battery charge, there are many places or times of the day where solar energy intensity is lower than the standard condition of 1 sun (100 mW cm^{-2}). Although the photocurrent density generated in photo-charging was naturally reduced with decreasing light intensity, the solar energy conversion efficiency, i.e., photocurrents normalized by the incident light intensity, was considerably higher at a lower light intensity (Figure S13). For example, surface charge separation efficiency (η_{surf}) significantly increases at attenuated light intensity (Figure S14), indicating that the hole recombination rate at semiconductor||electrolyte interface is greatly reduced, especially at the low-bias region. Thus, at 0.5 V_{RHE}, the 0.1 sun condition showed nearly three times less recombination than under 2.0 sun. Chopping illumination showed less transient current (evolution of spike due to the recombination of surface accumulated charges, Figure S15) at low biases under attenuated light intensity, indicating that less amounts of holes accumulated on the surface of the $NiFeO_x/BiVO_4$ PE. As low amounts of incident photons generate less amounts of holes at the surface, they give rise to a low kinetic barrier for hole transfer to the electrolyte. Such characteristics pose a significant merit of the present system in practical operation under circumstances wherein solar energy intensity is low.

The actual overload for solar rechargeable seawater battery can be also reduced, because the overall current density is reduced by attenuated light intensity, which leads to an improved applied bias photon-to-current efficiency calculated by dividing the photocurrent with the incident light intensity (Figure S13). In the present device configuration, a photocurrent above 3 mA seems to induce inefficient photo-charging due to the overpotentials arising from the anode compartment, such as the resistance of NASICON membrane and the overpotential of Na reduction reaction. Of course, the problem could be easily resolved by increasing the capacity of the anode part.

Photoelectrode-PV Tandem Cell for Unbiased Solar-Powered Seawater Battery

Finally, we realized solar-energy-only-driven charging of the seawater battery by using a PE-PV tandem cell as depicted in Figures 5A and S16. To the best of our knowledge, this is the first dual light absorber, 4 photons (D4) scheme applied for aquatic Na-O_2 cell, which produces Na as a solid solar fuel (electricity

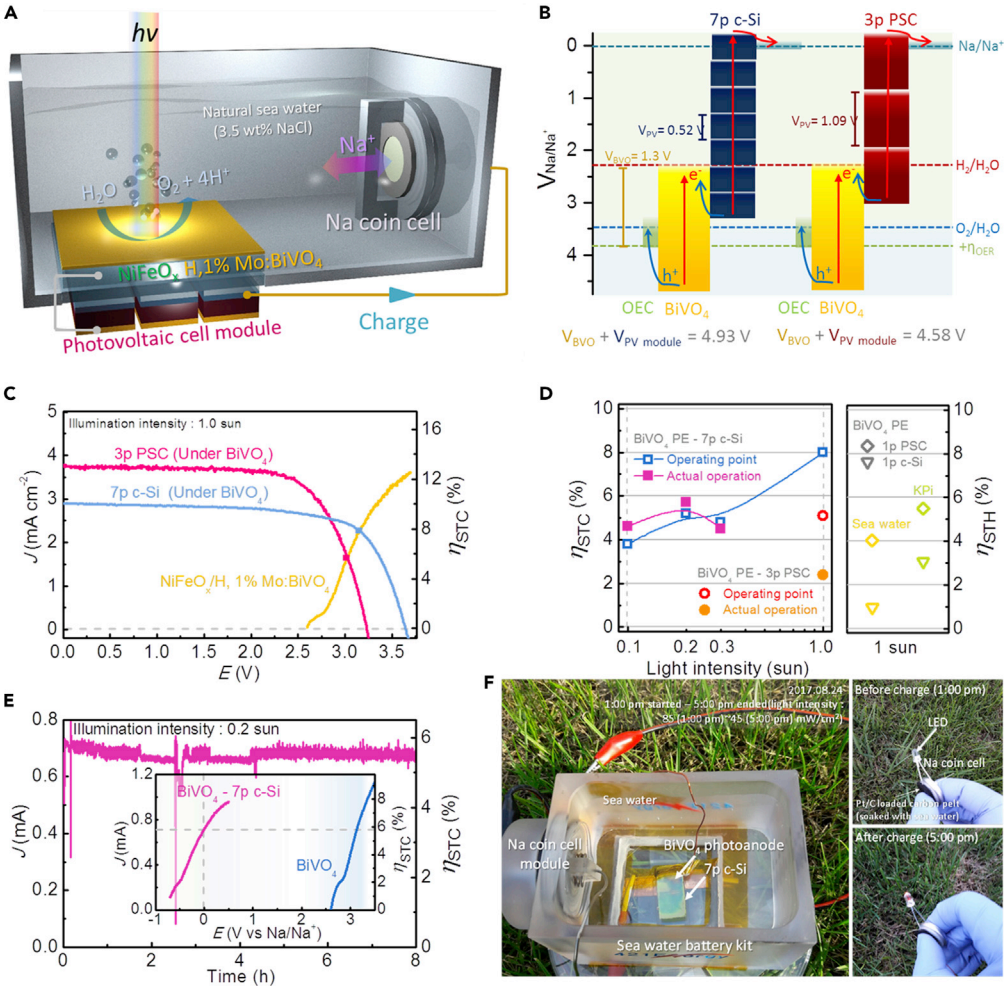

Figure 5. Unassisted Photo-charging of Solar Seawater Battery by a PE-PV Tandem Cell

(A) Scheme of solar rechargeable seawater battery with $NiFeO_x/BiVO_4$ PE in tandem with PSC or c-Si PVs for unassisted solar charging.

(B) Energy diagram of $BiVO_4$ PE and 7p c-Si or 3p PSC PV for unassisted solar charging. V_{PV} indicates photovoltage of individual solar cell and $V_{PV\ module}$ for whole module's photovoltage.

(C) Overlap of the J-V curves of the solar seawater cell and the PVs placed behind the PE under simulated 1 sun, showing the operating points (the PE active area: 0.25 cm^2; the PV active area: 2.27 cm^2).

(D and E) (D) Estimated solar-to-chemical conversion efficiency (η_{STC}) at the estimated operating points and actual operation of the tandem devices under various light intensities when compared with the solar-to-hydrogen conversion efficiency (η_{STH}) achieved by similar light absorbers under 1.0 sun condition (Figure S20). (E) Unassisted photo-charging of the solar-seawater tandem device with the 7p Si for 8 h under 0.2 sun. The inset shows the J-V curves before and after employing the tandem cell with c-Si PV (illuminated area: 2.30 cm^2).

(F) $BiVO_4$ PE-c-Si PV tandem assembly under natural sun. Conditions: solar intensity (85–45 mW/cm^2), seawater (Ilsan beach, Ulsan, Republic of Korea [GPS 35.497005, 129.430996, pH~8.0], active area: 2.7 cm^2 for the PE, charge time: nearly 4 h). Charge storage electrode: desodiated hard carbon anode; see Transparent Methods and Figure S23. The discharge test, where a Pt/C-loaded carbon electrode was used as cathode, was conducted by powering a red light-emitting diode bulb (see Video S1).

equivalent) instead of common gas fuels like H_2. For PVs, side-by-side series-connected 7 pieces of crystalline silicon solar cell (7p c-Si) or 3 pieces lead halide ($MAPbI_3$) perovskite solar cell (PSC) were used (details in Figures S17–S19), which showed open-circuit voltages (V_{OC}) of ~3.65 and ~3.25 V under $BiVO_4$ PE, respectively. Operating points (J_{op}) and solar-to-chemical conversion efficiency (η_{STC}) of these $BiVO_4$ PE-PVs under 1 sun condition were 2.29 $mAcm^{-2}$ and 8.0% for 7p c-Si, whereas they were J_{op} = 1.64 mA cm^{-2} and η_{STC} = 5.7% for 3p PSC (Figure 5B). Despite the relatively lower estimated η_{STC} and insufficient stability of PSC, its low cost makes it a promising option for practical systems (Kim et al.,

2019). In any case, these are unprecedentedly high efficiencies for SRCs outperforming recently reported devices of the integrated RFBs with p/n Si photoanode and photocathode (5.44–5.9%) (Li et al., 2016b; Liao et al., 2016), or Ta_3N_5 photoanode-GaN/Si photocathode (3.0%) (Cheng et al., 2017). The η_{STC} is also higher than solar-to-hydrogen conversion efficiency (η_{STH}) with the same PE-PV tandem assemblies; η_{STH} of 5.5% and 3.05% for the PE-1p PSC and the PE-1p c-Si, respectively, in 0.1 M KPi (Figure S20), and even higher than the reported most efficient metal oxide-based PE-PV tandem cell for water splitting ($BiVO_4$-Fe_2O_3-c-Si, η_{STH} of 7.7%) (Kim et al., 2016b). More recently, systems of higher efficiency have been demonstrated: triple junction III/V solar cell jointed with RFB with η_{STC} of 14.1% (Li et al., 2018) and PSC solar cell with DC-DC converter—Li ion battery of 9.8% (Ashim et al., 2017). However, our seawater battery system still has practical advantages of an environmentally benign electrolyte, a stable metal oxide light absorber, and a simple PV module.

In actual unassisted solar charging operation, we found that the photocurrent generated under 1 sun with the PE-PV tandem cell (~5 mA) overloaded the Na storage (anode) compartment. Thus, we conducted unbiased charging under attenuated light intensities (0.1–0.3 sun) (Figures 5C, S25, and S21). The c-Si tandem system enabled spontaneous seawater battery charge without any external bias under the attenuated light, showing good reproducibility close to the expected operating points with the maximum unbiased photocurrent of 0.7 mA at 0.2 sun, achieving an actual η_{STC} of ~5.7%. Owing to low capacity of Na coin cell, η_{STC} of PE-PV using PSC (Figure S22) was lower than expectation (Figure S20). Increasing overall size and reducing resistance of Na coin cell will greatly metigate such loss. The device operated in a stable manner for 8 h without notable degradation of the J_{ph} (Figure 5E and the inset), suggesting a unique and promising way for low-cost, efficient, and scalable solar energy deployment. We also tested a stand-alone mode of the solar-seawater tandem device as a solar seawater battery under real sunlight, demonstrating the spontaneous, unbiased photo-charging and successful powering of a red light-emitting diode bulb (Figure 5F and Video S1).

DISCUSSION

Our solar seawater tandem device is distinct from existing solar fuel production systems as much as it performs energy conversion from sunlight to Na in the form of a dense solid equivalent to electricity, instead of the usual gas or liquid fuels by harnessing the most earth-abundant natural resource, *seawater*, which plays roles in providing the Na^+ ion source as well as mediating seawater battery charging via seawater splitting. The monolithically combined system is more efficient relative to the simple connection of PV to the battery. As demonstrated in Figure S24, the simple connection of 9p c-Si as PV device (OEC-PV) with an IrO_2 electrode under attenuated 0.1 sun showed η_{STC} of 1.18%, whereas our PE-PV device showed nearly three times higher efficiency (η_{STC} = 3.92%). As PE has a larger band gap and a high photovoltage by itself (1.3 V), it is energetically more favorable to combine dual light absorbers (PV + PE) instead of PV only for maximizing solar energy harvesting. This approach to solar-to-Na (or electricity) production is considered intrinsically more efficient than solar-to-hydrogen production owing to better match of current density and potential (Figure S24). Thus, in solar hydrogen production by a PE-PV tandem cell, low photocurrents of the front photoanode limit the efficiency (Kim et al., 2016b). However, this seawater battery charge needs high voltage, whereas the current density is a low priority, and photoanodes provide higher photovoltage than most known PV devices. We were able to operate completely bias-free, spontaneous solar charge of seawater battery for 8 h. However, for practical applications, it should be much longer than 10 years (Rongé et al., 2015). Previous studies on the stability of PEs for water oxidation demonstrated stability for less than 2,000 h (Sun et al., 2015; Zhou et al., 2016), and thus the stability issue should be addressed in further developments of PEC devices in addition to efficiency.

Finally, solar-to-energy conversion efficiencies achieved by various light absorbers and battery systems are compared in Figure S25. It demonstrates that our novel solar rechargeable seawater battery shows a top efficiency, although it is made of earth-abundant, cheap, and nature-friendly materials and thus holds a high prospective for practical applications.

METHODS

All methods can be found in the accompanying Transparent Methods supplemental file.

SUPPLEMENTAL INFORMATION

Supplemental Information can be found online at https://doi.org/10.1016/j.isci.2019.07.024.

ACKNOWLEDGMENTS

This research was supported by the Basic Science Grant (NRF-2018R1A2A1A05077909), Climate Change Response project (2015M1A2A2074663, NRF-2017M1A2A2087630), Korea Center for Artificial Photosynthesis (KCAP, No. 2009-0093880), Korea-China Key Joint Research Program (2017K2A9A2A11070341) funded by MSIT, and Project No. 10050509 and KIAT N0001754 funded by MOTIE of Republic of Korea.

AUTHOR CONTRIBUTIONS

J.H.K. conceived the idea, performed synthesis and conducted electrochemical analysis for photoelectrodes and solar battery system, and characterized the materials. S.M.H and J.H. prepared Na coin cell and seawater battery testing instrument; I.H. prepared and characterized silicon solar cell and its module under supervision of K.S.; J.H.K. synthesized Fe_2O_3 and TiO_2; Y.H.J. prepared and characterized perovskite solar cell; Y.K. and J.S.L. supervised the project. J.H.K., S.M.H., Y.K., and J.S.L co-wrote the manuscript.

DECLARATION OF INTERESTS

The authors declare no competing financial interests.

Received: November 17, 2018
Revised: February 9, 2019
Accepted: July 15, 2019
Published: September 27, 2019

REFERENCES

Abirami, M., Hwang, S.M., Yang, J., Senthilkumar, S.T., Kim, J., Go, W.-S., Senthilkumar, B., Song, H.-K., and Kim, Y. (2016). A metal–organic framework derived porous cobalt manganese oxide bifunctional electrocatalyst for hybrid Na–Air/Seawater batteries. ACS Appl. Mater. Interfaces *8*, 32778–32787.

Ashim, G., Ke, C., Reza, K., Saad, A.S., Geetha, V., Rajesh, P., Roya, N., and Qiquan, Q. (2017). Highly efficient perovskite solar cell photocharging of lithium ion battery using DC–DC booster. Adv. Energy Mater. *7*, 1602105.

Azevedo, J., Seipp, T., Burfeind, J., Sousa, C., Bentien, A., Araújo, J.P., and Mendes, A. (2016). Unbiased solar energy storage: photoelectrochemical redox flow battery. Nano Energy *22*, 396–405.

Blankenship, R.E., Tiede, D.M., Barber, J., Brudvig, G.W., Fleming, G., Ghirardi, M., Gunner, M.R., Junge, W., Kramer, D.M., Melis, A., et al. (2011). Comparing photosynthetic and photovoltaic efficiencies and recognizing the potential for improvement. Science *332*, 805–809.

Cheng, Q., Fan, W., He, Y., Ma, P., Vanka, S., Fan, S., Mi, Z., and Wang, D. (2017). Photorechargeable high voltage redox battery enabled by Ta3N5 and GaN/Si dual-photoelectrode. Adv. Mater. *29*, 1700312–1700319.

Cook, T.R., Dogutan, D.K., Reece, S.Y., Surendranath, Y., Teets, T.S., and Nocera, D.G. (2010). Solar energy supply and storage for the legacy and nonlegacy worlds. Chem. Rev. *110*, 6474–6502.

Kim, G., Oh, M., and Park, Y. (2016a). Solar-rechargeable battery based on photoelectrochemical water oxidation: solar water battery. Sci. Rep. *6*, 33400.

Kim, J.-K., Mueller, F., Kim, H., Bresser, D., Park, J.-S., Lim, D.-H., Kim, G.-T., Passerini, S., and Kim, Y. (2014). Rechargeable-hybrid-seawater fuel cell. NPG Asia Mater. *6*, e144.

Kim, J.H., Hansora, D., Sharma, P., Jang, J.-W., and Lee, J.S. (2019). Toward practical solar hydrogen production – an artificial photosynthetic leaf-to-farm challenge. Chem. Soc. Rev. *48*, 1908–1971.

Kim, J.H., Jang, J.-W., Jo, Y.H., Abdi, F.F., Lee, Y.H., van de Krol, R., and Lee, J.S. (2016b). Hetero-type dual photoanodes for unbiased solar water splitting with extended light harvesting. Nat. Commun. *7*, 13380.

Kim, J.H., and Lee, J.S. (2019). Elaborately modified BiVO4 photoanodes for solar water splitting. Adv. Mater. *31*, e1806938.

Kim, T.W., and Choi, K.-S. (2014). Nanoporous BiVO4 photoanodes with dual-layer oxygen evolution catalysts for solar water splitting. Science *343*, 990–994.

Kim, T.W., Ping, Y., Galli, G.A., and Choi, K.-S. (2015). Simultaneous enhancements in photon absorption and charge transport of bismuth vanadate photoanodes for solar water splitting. Nat. Commun. *6*, 8769.

Kim, Y., Kim, H., Park, S., Seo, I., and Kim, Y. (2016c). Na ion- conducting ceramic as solid electrolyte for rechargeable seawater batteries. Electrochim Acta *191*, 1–7.

Kurtz, S., Haegel, N., Sinton, R., and Margolis, R. (2017). A new era for solar. Nat. Photon. *11*, 3–5.

Lee, D.K., and Choi, K.-S. (2017). Enhancing long-term photostability of BiVO4 photoanodes for solar water splitting by tuning electrolyte composition. Nat. Energy, 53–60.

Lewis, N.S. (2016). Research opportunities to advance solar energy utilization. Science *351*, aad1920.

Li, Q., Li, N., Liu, Y., Wang, Y., and Zhou, H. (2016a). High-safety and low-cost photoassisted chargeable aqueous sodium-ion batteries with 90% input electric energy savings. Adv. Energy Mater. *6*, 1600632–1600637.

Li, Q., Liu, Y., Guo, S., and Zhou, H. (2017). Solar energy storage in the rechargeable batteries. Nano Today *16*, 46–60.

Li, W., Fu, H.-C., Li, L., Cabán-Acevedo, M., He, J.-H., and Jin, S. (2016b). Integrated photoelectrochemical solar energy conversion and organic redox flow battery devices. Angew. Chem. Int. Ed. *55*, 13104–13108.

Li, W., Fu, H.-C., Zhao, Y., He, J.-H., and Jin, S. (2018). 14.1% efficient monolithically integrated solar flow battery. Chem *4*, 2644–2657.

Liao, S., Zong, X., Seger, B., Pedersen, T., Yao, T., Ding, C., Shi, J., Chen, J., and Li, C. (2016). Integrating a dual-silicon photoelectrochemical cell into a redox flow battery for unassisted photocharging. Nat. Commun. *7*, 11474.

Liu, G., Shi, J., Zhang, F., Chen, Z., Han, J., Ding, C., Chen, S., Wang, Z., Han, H., and Li, C. (2014). A tantalum nitride photoanode modified with a hole-storage layer for highly stable solar water splitting. Angew. Chem. Int. Ed. *53*, 7295–7299.

Liu, Y., Li, N., Liao, K., Li, Q., Ishida, M., and Zhou, H. (2016). Lowering the charge voltage of Li-O2 batteries via an unmediated

photoelectrochemical oxidation approach. J. Mater. Chem. A *4*, 12411–12415.

Luo, W., Yang, Z., Li, Z., Zhang, J., Liu, J., Zhao, Z., Wang, Z., Yan, S., Yu, T., and Zou, Z. (2011). Solar hydrogen generation from seawater with a modified BiVO4 photoanode. Energy Envrion. Sci. *4*, 4046–4051.

Ma, Y., Kafizas, A., Pendlebury, S.R., Le Formal, F., and Durrant, J.R. (2016). Photoinduced absorption spectroscopy of CoPi on BiVO4: the function of CoPi during water oxidation. Adv. Funct. Mater. *26*, 4951–4960.

Ma, Y., Pendlebury, S.R., Reynal, A., Le Formal, F., and Durrant, J.R. (2014). Dynamics of photogenerated holes in undoped BiVO4 photoanodes for solar water oxidation. Chem. Sci. *5*, 2964–2973.

Mayer, M.T. (2017). Photovoltage at semiconductor–electrolyte junctions. Curr. Opin. Electrochem. *2*, 104–110.

Montoya, J.H., Seitz, L.C., Chakthranont, P., Vojvodic, A., Jaramillo, T.F., and Nørskov, J.K. (2016). Materials for solar fuels and chemicals. Nat. Mater. *16*, 70–81.

Nikiforidis, G., Tajima, K., and Byon, H.R. (2016). High energy efficiency and stability for photoassisted aqueous lithium–iodine redox batteries. ACS Energy Lett. *1*, 806–813.

Nocera, D.G. (2017). Solar fuels and solar chemicals industry. Acc. Chem. Res. *50*, 616–619.

Pan, L., Kim, J.H., Mayer, M.T., Son, M.-K., Ummadisingu, A., Lee, J.S., Hagfeldt, A., Luo, J., and Grätzel, M. (2018). Boosting the performance of Cu2O photocathodes for unassisted solar water splitting devices. Nat. Catal. 412–420.

Pellow, M.A., Emmott, C.J.M., Barnhart, C.J., and Benson, S.M. (2015). Hydrogen or batteries for grid storage? A net energy analysis. Energy Envrion. Sci. *8*, 1938–1952.

Roger, I., Shipman, M.A., and Symes, M.D. (2017). Earth-abundant catalysts for electrochemical and photoelectrochemical water splitting. Nat. Rev. Chem. *1*, 0003.

Rongé, J., Bosserez, T., Huguenin, L., Dumortier, M., Haussener, S., and Martens, J.A. (2015). Solar hydrogen reaching maturity. Oil Gas Sci. Technol. *70*, 863–876.

Seitz, L.C., Chen, Z., Forman, A.J., Pinaud, B.A., Benck, J.D., and Jaramillo, T.F. (2014). Modeling practical performance limits of photoelectrochemical water splitting based on the current state of materials research. ChemSusChem *7*, 1372–1385.

Shinagawa, T., Ng, M.T.-K., and Takanabe, K. (2017). Electrolyte engineering towards efficient water splitting at mild pH. ChemSusChem *10*, 4155–4162.

Sivula, K., and van de Krol, R. (2016). Semiconducting materials for photoelectrochemical energy conversion. Nat. Rev. Mater. *1*, 15010.

Sun, K., Saadi, F.H., Lichterman, M.F., Hale, W.G., Wang, H.-P., Zhou, X., Plymale, N.T., Omelchenko, S.T., He, J.-H., Papadantonakis, K.M., et al. (2015). Stable solar-driven oxidation of water by semiconducting photoanodes protected by transparent catalytic nickel oxide films. Proc. Natl. Acad. Sci. U S A *112*, 3612.

Um, H.-D., Choi, K.-H., Hwang, I., Kim, S.-H., Seo, K., and Lee, S.-Y. (2017). Monolithically integrated, photo-rechargeable portable power sources based on miniaturized Si solar cells and printed solid-state lithium-ion batteries. Energy Envrion. Sci. *10*, 931–940.

Wang, Z., Fan, F., Wang, S., Ding, C., Zhao, Y., and Li, C. (2016). Bridging surface states and current-potential response over hematite-based photoelectrochemical water oxidation. RSC Adv. *6*, 85582–85586.

Xu, J., Chen, Y., and Dai, L. (2015a). Efficiently photo-charging lithium-ion battery by perovskite solar cell. Nat. Commun. *6*, 8103.

Xu, X., Li, S., Zhang, H., Shen, Y., Zakeeruddin, S.M., Graetzel, M., Cheng, Y.-B., and Wang, M. (2015b). A power pack based on organometallic perovskite solar cell and supercapacitor. ACS Nano *9*, 1782–1787.

Yang, Z., Zhang, J., Kintner-Meyer, M.C.W., Lu, X., Choi, D., Lemmon, J.P., and Liu, J. (2011). Electrochemical energy storage for green grid. Chem. Rev. *111*, 3577–3613.

Yu, M., McCulloch, W.D., Huang, Z., Trang, B.B., Lu, J., Amine, K., and Wu, Y. (2016). Solar-powered electrochemical energy storage: an alternative to solar fuels. J. Mater. Chem. A *4*, 2766–2782.

Yu, M., Ren, X., Ma, L., and Wu, Y. (2014). Integrating a redox-coupled dye-sensitized photoelectrode into a lithium–oxygen battery for photoassisted charging. Nat. Commun. *5*, 5111.

Zhou, X., Liu, R., Sun, K., Papadantonakis, K.M., Brunschwig, B.S., and Lewis, N.S. (2016). 570 mV photovoltage, stabilized n-Si/CoOx heterojunction photoanodes fabricated using atomic layer deposition. Energy Envrion. Sci. *9*, 892–897.

ISCI, Volume *19*

Supplemental Information

Seawater-Mediated Solar-to-Sodium Conversion by Bismuth Vanadate Photoanode- Photovoltaic Tandem Cell: Solar Rechargeable Seawater Battery

Jin Hyun Kim, Soo Min Hwang, Inchan Hwang, Jinhyup Han, Jeong Hun Kim, Yim Hyun Jo, Kwanyong Seo, Youngsik Kim, and Jae Sung Lee

Supplemental Information

Seawater-mediated solar-to-sodium conversion by bismuth vanadate photoanode - photovoltaic tandem cell: Solar rechargeable seawater battery

Jin Hyun Kim[1]†, Soo Min Hwang[1]†, Inchan Hwang[1], Jinhyup Han[1], Jeong Hun Kim[1], Yim Hyun Jo[2], Kwanyong Seo[1], Youngsik Kim[1,3]*, Jae Sung Lee[1]**

Transparent methods

Preparation of $BiVO_4$ films. All chemicals used in this study were of analytical grade and used without further purification. $BiVO_4$ film was prepared by a modified metal-organic decomposition (MOD) method with a slight modification from our previous procedure(Kim et al., 2015a). Thus, 0.2 M $Bi(NO_3)\cdot 5H_2O$ (99.8 %; Kanto Chemicals) dissolved in acetic acid (99.7 %; Kanto Chemicals), 0.03 M $VO(acac)_2$ (98.0 %; Sigma Aldrich) and 0.03 M $MoO_2(acac)_2$ (98.0 %; Sigma Aldrich) in acetyl acetone (>99.0 %; Kanto Chemicals) were prepared as a precursor solution. Then stoichiometric amount of each precursor was mixed to complete a precursor solution. For Mo doping, Bi:(V+Mo) = 1:1 atomic ratio was applied for 1 % Mo:$BiVO_4$ films. For fabrication of a $BiVO_4$ film, 60 µl of solution was dropped on a FTO glass (2 cm x 2.5 cm) and dried for 15 min in Ar atmosphere. The FTO glass (TEC 8; Pilkington) was cleaned by using water + ethanol with ratio of 1: 5, and washed with copious amount of ethanol and finally stored in 2-propanol before usage. The greenish transparent precursor film was calcined at 550 °C for 30 mins to form a yellow $BiVO_4$ film. After annealing process, 2 cm x 2.5 cm $BiVO_4$/FTO was split to obtain photoanodes with a net irradiation area of 0.25 cm^2 connected by silver paste and copper wire and sealed with epoxy resin.

Preparation of WO_3 films. The WO_3 film was prepared by a polymer-assisted direct deposition (PADD) method that we reported previously(Kim et al., 2016c). PADD solution was prepared with 1.85 g of ammonium metatungstate (AMT, 99.5%; Sigma Aldrich) dissolved in 5 ml of deionized water. 1 ml of the AMT precursor was mixed with Triton X-114 (99.0%; Sigma Aldrich) (200 µl) and 200 µl of deionized water was added. For film deposition, 5 µl of the PADD solution was spread on the surface of F-doped SnO_2 glass (FTO, TEC-8, Pilkington) using a doctor blade method and dried at 80 °C for 30 min, annealed at 550 °C for 2 h.

Preparation of TiO_2 films. The rutile TiO_2 photoanode was prepared by a typical hydrothermal method[46]. Thus, 30 mL of deionized water was mixed with 30 mL HCl (35.0 %; Matsunoen Chemicals) to reach a volume of 60 mL solution. After 5 min stirring, 1 mL of titanium (IV) butoxide (97.0 %; Sigma-Aldrich) was put in the solution. The mixture was stirred for another 5 min, and transferred to 100 mL Teflon-lined stainless steel autoclave with a fluorine doped tin oxide (FTO, TEC 8, Pilkington) glass. The hydrothermal synthesis was conducted at 150 °C for 10

h in an electric oven. After synthesis, the autoclave was cooled down to room temperature, and as-made sample was rinsed with deionized water and dried in ambient air. Finally the sample was annealed at 500 °C for 3 h in a muffle furnace.

Preparation of Fe_2O_3 films. The hematite (α-Fe_2O_3) photoanode was prepared by a simple solution-based hydrothermal method[47]. As a starting material, iron oxyhydroxide (β-FeOOH) nanorods were grown on a fluorine doped tin oxide (FTO, TEC 8, Pilkington) glass at 100 °C for 6 h in an aqueous solution containing of 0.15 M $FeCl_3 \cdot 6H_2O$ (97.0 %; Sigma-Aldrich) 1 M $NaNO_3$ (≥99.0 %; Sigma-Aldrich), and HCl (35.0%; Matsunoen Chemicals) to adjust pH 1.0. After rinsing with deionized water, the film was dried at ambient temperature and pressure to get yellow thin film. The film was put into a muffle furnace at 800 °C and pulled after 20 min to finally obtain red-colored α-Fe_2O_3.

Preparation of IrO_x film on FTO glass. Cl_6IrNa_2 (Sigma Aldrich) was used as received. 20 mg of the precursor was dissolved in acetyl acetone (15 ml). 10 µl of the precursor solution was dropped on FTO glass (TEC 8; Pilkington) with size of 2.5 cm X 1.0 cm and dried in ambient atmosphere and finally put into 80 °C oven for full dryness. After 10 min, coated FTO glass was calcined at 500 °C for 60 min.

Hydrogen treatment of metal oxide films. Hydrogen treatment was conducted using borohydride decomposition method reported by Hao *et al*.[48] First, 16 mmol of $NaBH_4$ (>98%; Sigma Aldrich) was put in a 200 ml alumina crucible and another smaller alumina bottle (15 ml) was put on the $NaBH_4$ powder. In this smaller bottle, as-prepared metal oxide film (2 cm x 2.5 cm) was placed and finally 200 ml alumina crucible was covered with an alumina cover. This reactor was put in already-heated furnace at 500 °C for 30 min. Then the crucible was immediately taken out from the furnace and naturally cooled down.

$NiFeO_x$ co-catalyst deposition on the $BiVO_4$ film. The $NiFeO_x$ co-catalysts were deposited utilizing photo-assisted electrodeposition (PED) under AM 1.5G illumination according to the reported procedure(Li et al., 2016a). 30 mg of $FeSO_4 \cdot 7\ H_2O$ (≥99 %; Sigma Aldrich) and 10 mg of $NiSO_4 \cdot 6H_2O$ (99 %; Sigma Aldrich) were put in glass bottle and 100 ml of 0.5 M $KHCO_3$ (pH of 8.3, 30 min Ar gas purged before usage) was put in, resulting in transparent and yellow solution. Existence of bicarbonate anion deters premature oxidation of Fe^{2+} ion to iron hydroxide precipitation (which looks like orange colored dust-like particles). For deposition, photoelectrodeposition (PED) was conducted using as prepared precursor solution and photoelectrode (PE). Under illumination (AM 1.5G, 100 mW/cm^2), linear sweep voltammetry was applied with bias of -0.3 V to 0.5 V versus reference electrode (Ag/AgCl) for 4~6 times with pretreatment of -0.3 V for 5 seconds. Sequential linear sweep voltammetry gave reduced current density and over-deposition of $NiFeO_x$ could occur at certain point. After deposition, the PE was taken out and washed with copious about of DI water. Right after taken out, the PE might look in a slight darkened color ($Ni(OH)_2$ species) but gradually change to identical color of photoelectrode before $NiFeO_x$ deposition. PEs were stored in an Ar gas-filled bottle before usage.

Characterizations. XRD measurements were carried out with X-ray diffractometer using Ni-filtered Cu Kα (λ=1.54178 **Å**) radiation from a rotating anode source (X'Pert PRO MPD, PANalytical, 30 mA, 40 kV). UV-Vis absorbance was measured with a UV/Vis spectrometer (UV-

2401PC, Shimadzu). As a reference, $BaSO_4$ powder attached on FTO was used. The morphology of the samples was observed using a field-emission scanning electron microscope (FESEM, JEOL JMS-7400F, operated at 10 keV), and composition was examined by energy-dispersive X-ray spectroscopy (EDX). The chemical state of $BiVO_4$ and other films were probed by X-ray photoelectron spectroscopy (XPS) with an ESCALAB 250Xi spectrometer. Detailed microscopic structure and corresponding energy-dispersive X-ray spectroscopy (EDX) data were observed using Cs-corrected high-resolution scanning transmission electron microscope (HR-[S]TEM, JEOL, JEM 2200FS, 200 kV).

Measurements of photoelectrochemical performance. Photoelectrochemical (PEC) measurements of PEs were performed with a standard three-electrode configurations; photoanode as the working electrode, Pt mesh as the counter electrode and Ag/AgCl (3M NaCl) as the reference electrode. The scan rate for the current-voltage (J-V) curve was 20 mV/sec. For electrolyte, 0.1 M potassium phosphate (K_2HPO_4 or KPi) buffer (pH 7.0) was used as a standard electrolyte. Also, the natural seawater from Ilsan beach, Ulsan, Republic of Korea (GPS 35.497005, 129.430996) was filtered before the use and the pH was measured to be around 8 at room temperature. Quantitative information on the major ions existing in the seawater can be found elsewhere[24]. To measure the degree of charge separation, 0.5 M Na_2SO_3 (>98%, Sigma Aldrich) was added to the 0.1 M KPi. Potentials were recorded with correction by the Nernst relation $E_{RHE} = E_{Ag/AgCl} + 0.0591\ pH + 0.209$, in which $E_{Ag/AgCl}$ is applied bias potential and 0.209 is a conversion factor from the Ag/AgCl electrode to the RHE scale. All electrochemical data were recorded by using a potentiostat (IviumStat, Ivium Technologies). A 300 W Xenon lamp was used to make simulated 1 sun light irradiation condition (AM 1.5G, 100 mW/cm^2) by using a solar simulator (Oriel 91160) with an AM 1.5G filter calibrated with a reference cell certified by the National Renewable Energy Laboratories, USA.

Incident photon to current efficiency (IPCE) measurement was conducted using the 300 W Xe lamp as the light source with liquid IR filter and a monochoromator (Oriel Cornerstone 130 1/8 m monochromator) with a bandwidth limit of 5 nm. The intensity of light was measured before IPCE measurements by photodiode detector (Oriel 70260). Calculation of IPCE was carried out by the formula;

$$IPCE(\%) = \frac{1240 \times \mathrm{J}}{\lambda \times P} \times 100$$

where J = photocurrent density (mA cm^{-2}), P = light power density (mW cm^{-2}) at λ, and λ = wavelength of incident light (nm).

The Mott-Schottky plot was used to determine electrochemical properties using the equation;

$$\frac{1}{C^2} = \frac{2(V - V_f - kT/e)}{e\varepsilon\varepsilon_o N_D A^2}$$

where C = capacitance of photoanode (metal oxide + electrolyte double layer, etc), e = charge of electron (C), ε = dielectric constant of $BiVO_4$ ε_o = permittivity of vacuum, V = applied bias (*vs*. RHE), V_f = flat band potential (*vs*. RHE), k = Boltzmann constant, N_D = donor density for n-type semiconductor (cm^{-3}), A = surface area of photoanode and T = the temperature (K).

Photoelectrochemical impedance spectroscopy. Photoelectrochemical impedance Spectroscopy (PEIS) was conducted with the same configuration of PEC measurements at -0.3 – 0.6 V vs. Ag/AgCl with an AC frequency range 10^{-1} to 10^{4} Hz under AM 1.5G irradiation. The spectra were analyzed by the Z-View program (Scribner Associates Inc.) with using Randel circuit as equivalent circuit.

Photoelectrochemical H_2 and O_2 evolution. Using Ar as a carrier gas, the amounts of H_2 and O_2 gases evolved from the PEC cell were analyzed using a gas chromatograph (HP5890, molecular sieve 5 L column) equipped with a thermal conductivity detector (TCD). Light source and electrolyte were the same as those used for above PEC measurements, and the gas products were sampled every 20 mins.

Preparation of Si or lead halide perovskite PV device. PV devices of c-Si (1 piece or 7 pieces in series connection)(Um et al., 2017) or lead halide perovskite (1 piece or 3 pieces in series connection)[50] were prepared according to the procedures reported in our previous works.

Preparation of the NASICON membrane, charge-storage electrode, and counter electrode. A NASICON-type $Na_3Zr_2Si_2PO_{12}$ ceramic was used as the Na-ion conductive membrane in this work. The disc-type NASICON ceramics were fabricated according to our previous work[24]. Briefly, for a typical synthesis, $Na_3PO_4{\cdot}12H_2O$ (Daejung, 99%), ZrO_2 (Kanto, 99.9%), and SiO_2 (Daejung, 99%) powders were mixed and first-calcined at 400 °C for 5 h in air. The calcined powder was ground and then calcined at 1100 °C for 12 h in air, followed by grounding and drying. The as-dried powder was cold-isostatic pressed into disks, sintered at 1280 °C for 10 h in ambient air, and then processed into discs with a diameter of 15 mm and a thickness of 0.8 mm for use of the membrane. The ionic conductivity of the NASICON discs was measured to be approximately 9×10^{-4} $S{\cdot}cm^{-1}$ at room temperature. As a Na-ion-storage electrode, a hard carbon electrode was prepared by coating a slurry comprising hard carbon (MeadWestvaco Corporation), carbon black Super-P (TIMCAL), and poly(vinylidene fluoride) (PVDF, 10 wt%, Sigma Aldrich) powders at a weight ratio of 90:1:9 in *N*-methyl-2-pyrrolidone (NMP, Sigma Aldrich) onto an Al foil (15 µm-thick) with a doctor blade and subsequent drying at 120 °C for 6 h in an oven. The electrode was roll-pressed and dried in a vacuum oven. The loading level of hard carbon on the electrode (14Φ) was around 6 mg cm^{-2}. Carbon fiber felts (XF30A, Toyobo) with a thickness of 4 mm were used as the counter electrode (cathode) for discharging. Prior to the use, the carbon felts were subjected to heat-treatment at 500 °C for 3 h in ambient air, in order to make the surface hydrophilic. To enhance the discharge reaction kinetics, a commercially available Pt/C (20 wt% Pt on Vulcan XC-72, Premetek) electrocatalyst was loaded on heated carbon felts (HCFs). Specifically, the catalyst slurry was prepared by mixing the Pt/C powder (90 wt%) and PVDF binder (10 wt%) in NMP and coated on HCFs with a diameter of 16 mm, followed by drying at 80 °C in an oven. The loading level of Pt per unit of carbon felt volume was around 5 $mg{\cdot}cm^{-3}$.

Coin cell preparation. A coin-type seawater cell module (*421Energy Co., Ltd*) was used by employing PE and Pt/C-coated HCF as photo-charge and discharge electrodes, respectively. First, the charge storage compartment was assembled by attaching the NASICON disc to the open-structured top part and sealing with the bottom part, which contains a Whatman GF/D microfiber filter paper soaked with an organic electrolyte of 1 M $NaCF_3SO_3$ (Sigma Aldrich) dissolved in tetraethylene glycol dimethyl ether (Sigma Aldrich) and an anode of either Na

metal (99.9%, Sigma Aldrich) or hard carbon. The assembly was carried out in a glove box under high-purity Ar atmosphere (O_2 and H_2O <1 ppm).

Solar seawater cell test. For photo-charge and discharge tests, the PE and Pt/C-coated carbon electrode were put in seawater and connected to potentiostat (IviumStat, Ivium Technologies), respectively. Galvanostatic charge-discharge voltage profiles were recorded at current of 0.01-0.5 mA per electrode (geometric size of 0.25 cm^2 for PE and 1.0 cm^2 for Pt/C-coated HCF) at room temperature in ambient air. For the hard carbon electrode, the electrochemical properties of the half-cell (Na|hard carbon) were evaluated by using 2032 coin-type half-cells at a current rate of 25 mA g^{-1} in the voltage window of 0–2 V vs. Na/Na^+. The spontaneous, unassisted photo-charging test of the solar-seawater tandem device was examined under actual outdoor sun illumination from 1:00 pm (~85 mW cm^{-2}) to 5:00 pm (~45 mW cm^{-2}). Prior to the bias-free, outdoor test for red-LED lighting, a seawater coin-cell module containing a hard carbon anode was cycled 5 times at a current of 0.2 mA in a two-electrode configuration (hard carbon|seawater), by which the anode was subjected to the formation of solid-electrolyte interphase layer on the surface during the first charging and repeated sodiation/desodiation processes, finally making the anode almost fully-discharged (desodiated) state (state-of-charge~0%) (**Figure S23**). It should be noted that as a representative anode material for Na-ion storage, hard carbon possesses a capacity above 250 mAh/g and a low sodiation/desodiation potential, close to the redox potential of Na (**Figure S23b**).

Calculation of surface/bulk charge separation efficiency

For quantitative assessment of charge separation efficiency, photocurrent comparison between water oxidation/hole scavengers (H_2O_2, SO_3^{2-}) was used.

Water oxidation: $2H_2O + 4h^+ \rightarrow 4H^+ + O_2$, E^o=1.23 V_{RHE}

Sulfite oxidation: $SO_3^{2-} + h^+ \rightarrow SO_3^-$, E^o=0.73 V_{RHE}

Light absorption by a photocatalyst generates absorbed photocurrent (J_{abs}) that undergoes two major losses of bulk and surface recombination. Hence the measured photocurrent during water oxidation (J^{H2O}) is expressed by;

$J^{H2O} = J_{abs} \times \eta_{bulk} \times \eta_{surf}$

where η denotes the charge separation yield in the bulk of semiconductor (η_{bulk}) or on the surface (η_{surf}). Since the surface charge separation yield of SO_3^{2-} is almost 100% (η_{surf} = 1), as discussed above, the photocurrent from its oxidation can be expressed as follows:

$J^{SO3} = J_{abs} \times \eta_{bulk}$

For calculation of J_{abs} value, below correlation between absorbance and radiation (Kim et al., 2016b; Kim et al., 2014b).

$P_d = P_0 10^{-A}$

$P_{abs} = P_0(1-10^{-A})$

P_0 (unit : $mWcm^{-2}nm^{-1}$) is provided power by solar simulator (in this case, AM 1.5G), P_{abs} is power of light actually absorbed by photoanode and P_d is power of light not absorbed to photoanode but dissipated (reflection & penetration). A is absorbance of photoanode (in this case, $BiVO_4$) and LHE (light harvesting efficiency) is defined as $1-10^{-A}$. So light which is not absorbed at photoanode will be 10^{-A}. Integrated $P_{abs}(\lambda)$ ($mWcm^{-2}nm^{-1}$) along with wavelength λ

gives total power (unit of $mWcm^{-2}$) which is power of light absorbed by photoanode (maximum power of photoanode). Below formula shows such relationship for photon absorption (J_{abs}).

$$J_{abs}(\frac{mA}{cm^2}) = \int_{\lambda_1}^{\lambda_2} \frac{\lambda}{1240} P_{abs}(\lambda) d\lambda \qquad (\frac{mW}{cm^2})$$

J_{abs} is avg. 5.45 mA/cm^2 for 1% Mo:$BiVO_4$ films, while J_{max} = 7.5 mA/cm^2 for 100 % of LHE till 2.4 eV (516nm) threshold is assumed. Bulk and surf separation efficiencies were calculated by:

$\eta_{bulk} = J^{SO3} / J_{abs}$

$\eta_{surf} = J^{H2O} / J^{SO3}$

Calculation of the theoretical cell voltage of rechargeable seawater batteries

Using natural seawater as the catholyte, seawater batteries involve the redox reactions of Na^+ ions on the anode side and the redox reactions of the seawater on the cathode during charge and discharge processes (Abirami et al., 2016; Kim et al., 2016a; Kim et al., 2016d). Featuring an open-structured cathode being exposed to ambient air, the seawater batteries use oxygen gases to discharge electricity: the oxygen gases are provided from the surrounding atmosphere into the seawater catholyte (*aeration*). Thus, dissolved oxygen in seawater participates in the redox reactions of seawater catholyte, leading to the oxygen evolution reaction/oxygen reduction reaction (OER/ORR) at the cathode during the charge/discharge processes. According to the simulated Pourbaix diagram in Figure S3, the OER is thermodynamically favored over hypochlorite formation reaction in seawater with pH~8 upon charging; however, both the reactions would compete with each other at high charging currents, due to the relatively sluggish kinetics of the OER. Assuming the partial pressure of oxygen in seawater at 100% saturation (P_o~0.206 atm), the pH value of natural seawater (pH~8), and the concentration of Na^+ in seawater (~0.47 M), the half-cells and overall reactions and theoretical cell voltage (E_{cell}) are expressed below; the cathode half-cell reaction (water redox reactions) is expressed in the form of neutral and alkaline ones, but equivalent to Eq. 1.

$$4Na\ (s) + O_2\ (aq) + 2H_2O\ (l) \underset{charge}{\overset{discharge}{\rightleftharpoons}} 4NaOH\ (aq);\ E_{cell}\sim 3.48\ V$$

Anode: $4Na^+ + 4e^- \leftrightarrow 4Na$

$$e_{anode} = e^o_{Na^+/Na} + \frac{RT}{4F} ln\left(\frac{a^4_{Na^+}}{a^4_{Na}}\right) = e^o_{Na^+/Na} + \frac{RT}{4F} ln\left(\frac{[Na^+]^4}{[Na]^4}\right) + \frac{RT}{4F} ln\left(\frac{\gamma^4_{Na^+}}{\gamma^4_{Na}}\right)$$

$$= -2.71 + 0.0591\, log[Na^+] + \frac{0.0591}{4} log(\gamma^4_{Na^+})$$

Cathode: $O_2 + 2H_2O + 4e^- \leftrightarrow 4OH^-$(*aerated*, based on 4-electron transfer)

$$e_{catho} = e^o_{O_2/H_2O} + \frac{RT}{4F} ln\left(\frac{a_{O_2} a^2_{H_2O}}{a^4_{OH^-}}\right)$$

$$= e^o_{O_2/H_2O} + \frac{RT}{4F} ln\left(\frac{[O_2][H_2O]^2}{[OH^-]^4}\right) + \frac{RT}{4F} ln\left(\frac{\gamma_{O_2}\gamma^2_{H_2O}}{\gamma^4_{OH^-}}\right)$$

$$= 1.229 + \frac{0.0591}{4} log(P_{O_2}) - 0.0591pH + \frac{0.0591}{4} log\left(\frac{\gamma_{H_2O}^2}{\gamma_{OH^-}^4}\right)$$

Overall: $e_{overall} = e_{cathode} - e_{anode}$

$$= 3.939 + \frac{0.0591}{4} log(P_{O_2}) - 0.0591pH - 0.0591\, log[Na^+] + \frac{0.0591}{4} \log(\frac{\gamma_{H_2O}^2}{\gamma_{Na^+}^4 \gamma_{OH^-}^4}) \approx 3.48 \text{ V}$$

The activity coefficients for H_2O, Na^+, and OH^- are assumed to be 1, yielding $e_{overall}$ of 3.48 V

Selection of the photoelectrode for the solar seawater battery and proof of concept demonstration of the photo-charging

To establish the concept of solar-seawater battery with a photoelectrode, well-known *n*-type metal oxide semiconductors, such as TiO_2, WO_3, Fe_2O_3 and $BiVO_4$ (detailed preparation procedure can be found in Materials and Methods section), were examined as the potential photoelectrodes (PEs) that can oxidize seawater upon illumination (**Figure S1**). Considering the band structure of those materials (**Figure S1A**), the degree of reduction in the voltage for charging the battery depends on the positions of the conduction band (CB) and valence band (VB) of the PE, relative to the redox potential of H_2O. With Pt as electrocatalyst, the potential needed to initiate charge reaction is estimated to be 3.48 V (*vs*. Na/Na^+) plus the overpotential of water oxidation (η_{OER}) in seawater (> ~0.3 V), which gives approximately 3.78 V. Since photoelectrodes perform water oxidation by capturing photons to generate photo-voltage, the potential difference between the CB and E(Na/Na^+) will be the potential needed to charge the battery. This photo-driven process lowers the charge voltage, as compared to the case of using an electrocatalyst (TiO_2 = 1.95 V, WO_3 = 2.65 V, Fe_2O_3 = 2.55 V, $BiVO_4$ = 2.25 V). It should be considered that the practical potential saving will likely to be potential difference between E(flat band) and E(Na/Na^+), which will decrease potential saving usually by 0.2~0.4 V. Water is preferentially oxidized owing to its favored thermodynamics in neutral pH condition (Luo et al., 2011). The J-V curve of the photoelectrodes in seawater shows little difference from that in potassium biphosphate buffer (KPi) electrolyte (**Figure S1B-S1F**), which indicates that existence of Cl^- anion does not affect significantly the hole transfer on photoelectrode, which will be discussed in **Figure S9**.

XPS characterization of the NiFeOx/H, 1% Mo:$BiVO_4$ photoelectrode (Fig. S9-S11)

C1s spectrum was detected for all $BiVO_4$ films and C-C at 284.8 eV due to presence of adventitious carbon was the most dominant peak(Kim et al., 2015a). Small peak of carbonate (288.5 eV) was observed due to similar reason for 1% Mo:$BiVO_4$ and H, 1% Mo:$BiVO_4$ while it was suspected that deposition of $NiFeO_x$ might have induced carbonate on the surface(Kim et al., 2015a). Fitting in normalized intensity showed that there was not significant relative intensity change made by the formation of carbonate, unlike carbonate (Co-Ci) electrocatalyst case we previously reported(Kim et al., 2015b). Stability test in seawater and XPS analysis indicates that $NiFeO_x$ deposited $BiVO_4$ film works in absence of bicarbonate anion.

Reduction treatment induced a noticeable shoulder peak of M-O (529.9 eV for $BiVO_4$) that is positioned between 531.1 eV (oxygen vacancy)(Kim et al., 2015a; Qin et al., 2014), ~ 531.7 eV (-OH(Kim et al., 2015a; Kim et al., 2015b)), suggesting possible hydrogen attachment or oxygen vacancy formation by the reduction treatment.

Further deposition of $NiFeO_x$ showed very clear peak of –OH (531. 3~531.5 eV), which is from formation of oxyhydroxide, very similar to previously reported semi-water-permeable metal oxyhydroxides and their derivatives (Co-Pi, Co-Ci, Ni-Ci, FeOOH, NiOOH, $NiFeO_x$)(Kim et al., 2015a; Kim et al., 2015b; Kim et al., 2015c; Kuang et al., 2016; Morales-Guio et al., 2015; Pilli et al., 2011; Pilli et al., 2015; Seabold and Choi, 2012).

$NiFeO_x$-loaded photoelectrode exhibited Fe 2p and Ni 2p spectra but with slight change before and after ~12 h of the PEC reaction in seawater. Fe showed a strong peak at 711.0 eV due to Fe^{3+}, with a little shoulder peak due to Fe^{2+} (Morales-Guio et al., 2015). Small peaks between two Fe^{3+} peaks (as $NiFeO_x$) would be Ni LMM (713.6 eV) and Sn 3p (716.5 eV), indicating exposed FTO surface in our photoelectrode(Morales-Guio et al., 2015). After reaction in seawater, contents of Ni was greatly reduced while Fe^{3+} and Sn 3p remain similar, indicating that Ni elemental ratio decreased during the PEC reaction. Also, the intensity of Sn 3p peak did not greatly increase, indicating no noticeable corrosion, *i.e.* leaching of $BiVO_4$ and exposal of FTO were not noted during 12 h of PEC operation. Indeed, elemental ratio of Ni:Fe of 1:2 in pristine condition became 1:5 after the PEC reaction. Since activity of $NiFeO_x$/H, 1% Mo:$BiVO_4$ film was changed little before and after PEC operation, it appears that Ni:Fe ratio is quickly set to such a value at an early stage of PEC operation. Deposition of only Fe or Ni showed significantly lower PEC performance, thus a small amount of Ni is essential for a high water oxidation activity in seawater. Oxidation state from XPS spectra would be 2^+ to 3^+ and in a hydroxide form instead of oxide.

Effect of the anions in seawater on the PEC performance

We studied the effect of other anions on the PEC properties in seawater; they might cause any side reactions, making the system unsustainable in a long-term operation. Besides water and Na^+ ions, seawater typically has plenty of Cl^- ions (~0.54 M) and not a few SO_4^- ions (~0.028 M); in particular, Cl^- might undergo chlorine gas evolution upon illumination, followed by the formation of HClO or OCl^- depending to the pH (Eq. S2 to S4).

Thus, we conducted comparison tests to examine the effects of Cl^- and SO_4^- ions on the J-V curve of the $NiFeO_x$/H, 1% Mo:$BiVO_4$ PE. First, we varied the amount of 5 M NaCl (*aq*) added to a KPi buffer (pH 7) or the concentration of the NaCl in a sole NaCl (*aq*) electrolyte in the range of 1 mM -5.0 M. The addition of NaCl (*aq*) to the KPi buffer did not affect the J-V (**Figure S12A**). The PEC performance in NaCl (*aq*) was relatively poor compared to that in the KPi buffer (Figure S12B). For the case of SO_4^- ions, addition of showed similar tendency to Cl^- but J-V curve measured with sole Na_2SO_4 showed better performance, which is still lower than KPi (**Figure S12C, S12D**). Thus, it appears that Cl^- and SO_4^- ions do not have adverse effects on the PEC property, but the buffer capacity of those anions are lacking greatly compared to known electrolytes (phosphate, borate, carbonate et al) for $NiFeO_x$-coated H, 1% Mo:$BiVO_4$ PE (Sayama et al., 2003).

It has been reported that Cl^- might undergo photoelectrocatalytic oxidation and indirect O_2 evolution (Chen et al., 2014; Huang et al., 2014; Luo et al., 2011). Such Cl^--assisted catalytic

(indirect) water splitting is considered to result from the Cl^- oxidation by photogenerated holes to form Cl_2 (Eq. S2), followed by the disproportionation (Eq. S3, S4) and the photodissociation of HClO or ClO^- (Eq. S5, S6). We found no noticeable side reactions, such as Cl_2 gas evolution, from the gas evolution test (**Figure 2E**), which may be attributed to the relatively low concentration of Cl^-, neutral pH, and/or high solubility of Cl_2 (*g*) in seawater; the high Cl^- content and high acidity (low pH) make the Cl^- oxidation thermodynamically more favorable than water oxidation(Dionigi et al., 2016),(Iguchi et al., 2018). For $NiFeO_x$ based oxygen evolution catalyst, Cl_2 evolution apart from O_2 evolution was unlikely since more than ~0.48 V higher voltage (thus nearly 1.71 V_{RHE}) is required than the water oxidation (~1.5 V $_{RHE}$) in seawater (at pH 8.0)(Dionigi et al., 2016), which might attribute to $NiFeO_x/BiVO_4$ having similar characteristics for surface oxidation reaction. Therefore, we tentatively concluded that the PEC reaction on our $NiFeO_x$ OEC-loaded $BiVO_4$ PE in seawater selectively perform O_2 evolution over indirect Cl^- oxidation; however, detailed mechanistic investigation is required through in-situ/ex-situ quantitative analyses.

$$2Cl^- + 2h^+ \xrightarrow{h\nu} Cl_2 \quad (2)$$

$$Cl_2 + H_2O \rightarrow H^+ + Cl^- + HClO \quad (3)$$

$$HClO \rightarrow ClO^- + H^+ \quad (4)$$

$$2HClO \xrightarrow{h\nu} 2H^+ + 2Cl^- + O_2 \quad (5)$$

$$2ClO^- \xrightarrow{h\nu} 2Cl^- + O_2 \quad (6)$$

On the other hand, the addition of the KPi into natural seawater improves the photocurrent density owing to its buffer capacity, as shown in **Figure S12E**.

Unbiased photo-charging of solar-seawater battery with PE-PV tandem configurations

Solar-to-energy (Na) conversion efficiency (η_{STC}) of solar-seawater battery is defined as the efficiency for unbiased photo-charging, considering the theoretical cell voltage of 3.48 V:

$$STC\ \ (\%) = \frac{3.48 \times J_{ph} \times \mathrm{FE}}{P}$$

where J_{ph} is photocurrent (mA cm^{-2}), *FE* is faradaic efficiency for fuel products (Na) and *P* is solar illumination power (AM 1.5G, 100 mW cm^{-2}). Thus, the system requires only J_{ph} of 2.87 mA cm^{-2} for achieving a η_{STC} of 10%. This J_{ph} is achievable using already existing PEs, for our case, the $BiVO_4$-based PE that shows J_{ph} over 3.5 $mAcm^{-2}$. In this work, the use of the $BiVO_4$-based PE lowers the voltage required for battery charging by ~1.3 V relative to >3.85 V for the IrO_2/FTO. But the battery still requires an electric potential more than 2.6 V in practice,, which can be supplied by employing multiple solar cells connected in series, such as 7 crystalline Si solar cells (7p c-Si) or 3 perovskite solar cells (3p PSC), placed behind the $NiFeO_x$/BiVO4 PE as schematically depicted in **Figure 6A.** The photovoltaic performance of the two types of PV devices under direct light irradiation and as a second light absorber behind the $NiFeO_x$/H, 1% Mo:$BiVO_4$ PE are shown in Figure **S21-S23**.

The operating point of the PE-PV tandem device is determined at the cross point of IV corves of PV device and photoelectrode as demonstrated in **Figure S24.** Thus, our PE-PV driven solar seawater battery has the operating efficiencies of 5.7 % for $BiVO_4$ – 3p PSC and 8.0 % for $BiVO_4$ – 7p c-Si, which is a new benchmarks for solar rechargeable batteries. As shown in **Figure S24E**,

our self-charging SRSB also show the highest ratio of solar-to-energy conversion efficiency and power conversion efficiency (PCS) of solar cells.

Supplemental Tables

Table S1. Summary of reported solar rechargeable batteries employing photoelectrodes, related to Figure 1.

Cell chemistry [anode|cathode]	Photoelectrodes Chemistry	E_{CB}(or E_{VB})/e [V vs. NHE]	Redox mediators Chemistry	E_{redox} [V vs. NHE]	V_{saved}* [V] (photo-charging mode)	η_{STC} (η_{SCE})$^{\perp}$ [%]@1-sun	References#
Aq. redox [Fe^{3+}/Fe^{2+}|Ce^{4+}/Ce^{3+}]	$BaTiO_3$	+0.6@pH 0	Ce^{4+}/Ce^{3+}	+1.6@pH 0	~1.0 (unbiased)	0.01(N/A) @0.75-sun	S1(Sharon and Sinha, 1982)
Aq. redox [Ni| $Fe(CN)_6^{3-}$/ $Fe(CN)_6^{4-}$]]	*n*-GaP (single crystal)	–1.3@pH 7	$Fe(CN)_6^{3-}/Fe(CN)_6^{4-}$	+0.36@pH 7	~1.66 (unbiased)	N/A	S2(Yoshiro et al., 1983)
Aq. Co-air [$Co(OH)_2/Co$|O_2]	*n*-GaP (single crystal)	–1.75@pH 14	O_2/OH^-	+0.4@pH 14	~2.1 (unbiased)	3(N/A)	S3(Akuto et al., 2001)
Aq. metal hydride-air [$LaNi_{3.76}Al_{1.24}H_n$|O_2]	*n*-$SrTiO_3$	–1.19@pH>14	O_2/OH^-	+0.16@pH>14	~1.35 (unbiased)	N/A	S4(Akuto and Sakurai, 2001)
Org. ClO_4-battery [PEDOT|PPy]	Dye(Z907)/TiO_2	–0.46	$PEDOT^+$/PEDOT	+0.69	~1.19 (unbiased)	N/A(~0.1)	S5(Liu et al., 2012)
Org. Li redox flow [WO_3|I_3^-/I^-]	Dye(N719)/TiO_2	–0.46	I_3^-/I^-(org.)	+0.38	~0.84 (unbiased)	N/A	S6(Yan et al., 2012)
Org. Li redox flow [$DMFc^+/DMFc^{\S}$|I_3^-/I^-]	Dye(Z907)/TiO_2	–0.46	I_3^-/I^-(org.)	+0.38	~0.84 (unbiased)	0.15	S7(Liu et al., 2013)
Hybrid Li redox flow [Li_2WO_4|I_3^-/I^-]	Dye(N719)/TiO_2	–0.46	I_3^-/I^-(org.)	+0.38	~0.84 (unbiased)	N/A	S8(Yan et al., 2013)
Aprotic Li–O_2 [Li|O_2]	Dye(N719)/TiO_2	–0.46	I_3^-/I^-	+0.5	~0.96 (photo-assisted)	N/A	S9(Yu et al., 2014)
Hybrid Li redox [Li|I_3^-/I^-]	Dye(Z907)/TiO_2	–0.46@pH 4.6	I_3^-/I^-	+0.5	~0.96 (photo-assisted)	N/A	S10(Yu et al., 2015)
Org. Na redox flow [S_4^{2-}/S_2^{2-}|I_3^-/I^-]	Dye(N719)/TiO_2	–0.46	I_3^-/I^-(org.)	+0.29	~0.75 (unbiased)	1.7(1.6$^{\parallel}$)	S11(Mahmoudzadeh et al., 2016)
Aq. redox flow [AQDS/$AQDSH_2^{\ddagger}$|I_3^-/I^-]	Dye(Z907)/TiO_2	–0.18~–0.7 @pH 0~8.55	I_3^-/I^-	+0.54 @pH 0~8.55	0.72~1.24 (unbiased)	N/A	S12(McCulloch et al., 2016)
Org. Li redox flow [PB§|EV^{2+}/EV^+–I_3^-/I^-]	Dye(Z907)/TiO_2	–0.44	I_3^-/I^-(org.)	+0.11	~0.55 (photo-assisted)	N/A	S13(Fan et al., 2017)
Aq. V redox flow [V^{3+}/V^{2+}|VO_2^+/VO^{2+}]	TiO_2	–0.18@pH 0	VO_2^+/VO^{2+}	+0.99@pH 0	~1.18 (unbiased)	N/A	S14(Wei et al., 2014)
Aq. V redox flow [V^{3+}/V^{2+}|VO_2^+/VO^{2+}]	TiO_2/WO_3	–0.18@pH 0	VO_2^+/VO^{2+}	+0.99@pH 0	~1.18 (unbiased)	N/A	S15(Liu et al., 2014a)

Aq. V redox flow [V^{3+}/V^{2+}|VO_2^+/VO^{2+}]	TiO_2	–0.18@pH 0	VO_2^+/VO^{2+}	+0.99@pH 0	~1.18 (unbiased)	N/A	S16(Liu et al., 2015a)
Aq. V redox flow [V^{3+}/V^{2+}|VO_2^+/VO^{2+}]	TiO_2/WO_3	–0.18@pH 0	VO_2^+/VO^{2+}	+1.0@pH 0	~1.18 (unbiased)	N/A	S17(Liu et al., 2015b)
Aq. V redox flow [V^{3+}/V^{2+}|VO_2^+/VO^{2+}]	TiO_2	–0.18@pH 0	VO_2^+/VO^{2+}	+0.99@pH 0	~1.18 (unbiased)	N/A	S18(Wei et al., 2016)
Aq. V redox flow [V^{3+}/V^{2+}|VO_2^+/VO^{2+}]	TiO_2	–0.18@pH 0	VO_2^+/VO^{2+}	+0.99@pH 0	~1.18 (unbiased)	0.6(N/A)	S19(Wei et al., 2017)
Hybrid LIB [Li|$LiFePO_4$]	TiO_2	–0.46	I_3^-/I^- ($LiFePO_4$)	+0.41	~0.87 (photo-assisted)	N/A	S20(Li et al., 2015b)
Aq. Na redox flow [S_4^{2-}/S^{2-}|I_3^-/I^-]	TiO_2	–0.44	I_3^-/I^-	+0.5	~1.05 (photo-assisted)	N/A	S21(Li et al., 2016b)
Li-ion battery [Li|$LiFePO_4$]	Dye(N719)	–1.5	$LiFePO_4/FePO_4$	+0.45	~1.95 (photo-assisted)	0.08(N/A)	S22(Paolella et al., 2017)
Solar-water [WO_3|Water]	TiO_2	–0.36@pH 3	0.01M Li_2SO_4 (aq); pH~3	+1.03@pH 3	~1.4 (unbiased)	N/A	S23(Kim et al., 2016a)
Aprotic Li–O_2 [Li|O_2]	g-C_3N_4	–1.34	I_3^-/I^-	+0.5	~1.84 (photo-assisted)	N/A	S24(Liu et al., 2015c)
Aprotic Li-O_2 [Li|O_2]	g-C_3N_4	–1.34	Li_2O_2/O_2	–0.08	~1.26 (photo-assisted)	N/A	S25(Liu et al., 2016)
Hybrid Li-S (primary) [H_2|S_4^{2-}/S_2^{2-}]	Pt/CdS	–1.4@pH 13	S_4^{2-}/S_2^{2-}	–0.45@pH 13	~0.95 (unbiased)	N/A	S26(Li et al., 2015a)
Aq. V redox flow [V^{3+}/V^{2+}|V^{3+}/VO^{2+}]	i) CdS ii) CdS/CdSe	i) –0.65@pH 0 ii) –0.45@pH 0	V^{3+}/VO^{2+}	+0.34@pH 0	i) ~0.99; ii) ~0.79 (unbiased)	i) 0.3 ‖ (N/A) ii) 0.85 ‖ (N/A)	S27(Azevedo et al., 2016)
Aq. redox flow [AQDS/$AQDSH_2$‡|Br_3^-/Br^-]	Dual-Si†[1)] i) n^+p-Si ii) p^+n-Si	buried junction	i) AQDS/$AQDSH_2$ ii) Br_3^-/Br^-	i) +0.20 ii) +1.09	total ~1.2 i) ~0.6; ii) 0.6 (unbiased)	5.9(3.2)	S28(Liao et al., 2016)
Aq. redox flow [AQDS/$AQDSH_2$|BQDS/$BQDSH_2$]‡	Dual-Si†[2)] i) p^+nn^+-Si ii) n^+np^+-Si	buried junction	i) AQDS/$AQDSH_2$ ii) BQDS/$BQDSH_2$	i) +0.20 ii) +0.89	total ~1.3 i) ~0.6; ii) ~0.7 (unbiased)	1.87 ‖ (1.7)	S29(Li et al., 2016c)
Aq. redox flow [2,6-DHAQ/2,6-reDHAQ‡|$Fe(CN)_6^{3-}/Fe(CN)_6$⁴⁻]	Dual-PEC i) GaN/n^+p-Si ii) Ta_3N_5	i) buried junction ii) E_{CB}~–0.3 @pH 12	i) 2,6-DHAQ/ 2,6-reDHAQ ii) $Fe(CN)_6^{3-}$/ $Fe(CN)_6^{4-}$	i) –0.7@pH 14 ii) +0.5@pH 12	total ~1.5 i) ~0.7; ii) ~0.8 (unbiased)	3(N/A)	S30(Cheng et al., 2017)
Hybrid Li redox	α-Fe_2O_3	+0.36@pH 7.9	I_3^-/I^-	+0.51@pH 7.9	~0.15	N/A	S31(Nikiforidi

[Li|I_3^-/I^-]					(photo-assisted)		s et al., 201 6)
Aq. redox flow [AQDS/AQDSNa$_2$‡|Fe(CN)$_6^{3-}$/ Fe(CN)$_6^{4-}$]	Polyaniline-coated α-F e_2O_3	–0.5@pH 14	Fe(CN)$_6^{3-}$/ Fe(CN)$_6^{4-}$	+0.49@pH 14	~1.0 (unbiased)	0.08(N/A)	S32(Wedege et al., 2016)
H_2O_2 fuel cell [Ni|Fe_3 (Co(CN) $_6$) $_3$]	WO_3	+0.40@pH 1.3	0.55 M NaCl (aq); pH 1.3	+1.22@pH 1.3	~0.82 (unbiased)	i) 0.55(0.28) ii) 0.94 @0.1sun (N/A)	S33(Mase et al., 2016)
Seawater cell [Na|seawater]	TiO_2	-0.66@pH 8	seawater	+0.77@pH 8	1.43 (photo-assisted)	N/A	This work
Seawater cell [Na|seawater]	Fe_2O_3	-0.11@pH 8	seawater	+0.77@pH 8	0.88 (photo-assisted)	N/A	This work
Seawater cell [Na|seawater]	WO_3	–0.06@pH 8	seawater	+0.77@pH 8	0.83 (photo-assisted)	N/A	This work
Seawater cell [Na|seawater]	i) $BiVO_4$ ii) $BiVO_4$/7p c-Si (tandem) iii) $BiVO_4$/3p PSC (tandem)	–0.46@pH 8	seawater	+0.77@pH 8	i) ~1.23 (photo-assisted) ii) total~4.88 (unbiased) iii) total~4.48 (unbiased)	i) N/A ii) 8.0(N/A) ii) 5.7(N/A)	This work

* V_{saved}: Saved voltage values (or measured photovoltage) estimated from the energy difference between the formal potential (E_{redox}) of redox mediators and the conduction band minimum (E_{CB}) of photoelectrodes. Unless otherwise noted in corresponding references, the band edge positions of photoelectrode are approximated by considering the operating conditions (e.g., pH) and typical values from literatures [x]. For the cases using 'buried junction(s)', the band edge position(s) of the photoelectrode(s) are not shown, but the photovoltage is extracted from the data in references.

⊥ η_{STC} (η_{SCE}): overall solar-to-energy efficiency (overall solar-to-electricity efficiency)

§ DMFc: [Fe($C_{10}H_{15}$)$_2$]

‡ AQDS: 9,10-anthraquinone-2,7-disulfonic acid
BQDS/BQDSH_2: 1,2-benzoquinone-3,5-disulfonic acid
2,6-DHAQ: 2,6-dihydroxyanthraquinone

$ Prussian blue; $Fe_4[Fe(CN)_6]_3$

† 1) Photocathode: C/TiO_2/Ti/n^+p-Si; photoanode: Pt/p^+n-Si
2) Photocathode: p^+nn^+-Si/Ti/TiO_2/Pt; photoanode: n^+np^+-Si/Ti/TiO_2/Pt

|| Those values mean the roughly calculated η, based on the information (graphs) in corresponding references.

#S1-S33 are numbering in Figure 1c and right side numbering is for reference in supplementary information

Table S2. Surface composition of elements in photoelectrodes analyzed by XPS spectra, related to Figure S4,5,6.

	1% Mo:$BiVO_4$	H, 1% Mo:$BiVO_4$	$NiFeO_x$/H, 1% Mo:$BiVO_4$ [a]	$NiFeO_x$/H, 1% Mo:$BiVO_4$ [b]
Bi 4f	6.83	7.05	1.41	2.91
O 1s	39.19	36.58	31.98	34.68
V 2p	5.66	5.08	1.30	1.71
Sn 3d	2.21	1.51	2.25	2.97
C 1s	45.66	48.03	53.35	50.73
Mo 3d	0.46	0.25	0.00	0.00
Ni 2p			3.39	1.01
Fe 2p			6.33	5.99

[a]Pristine
[b]After PEC reaction for 24 h.

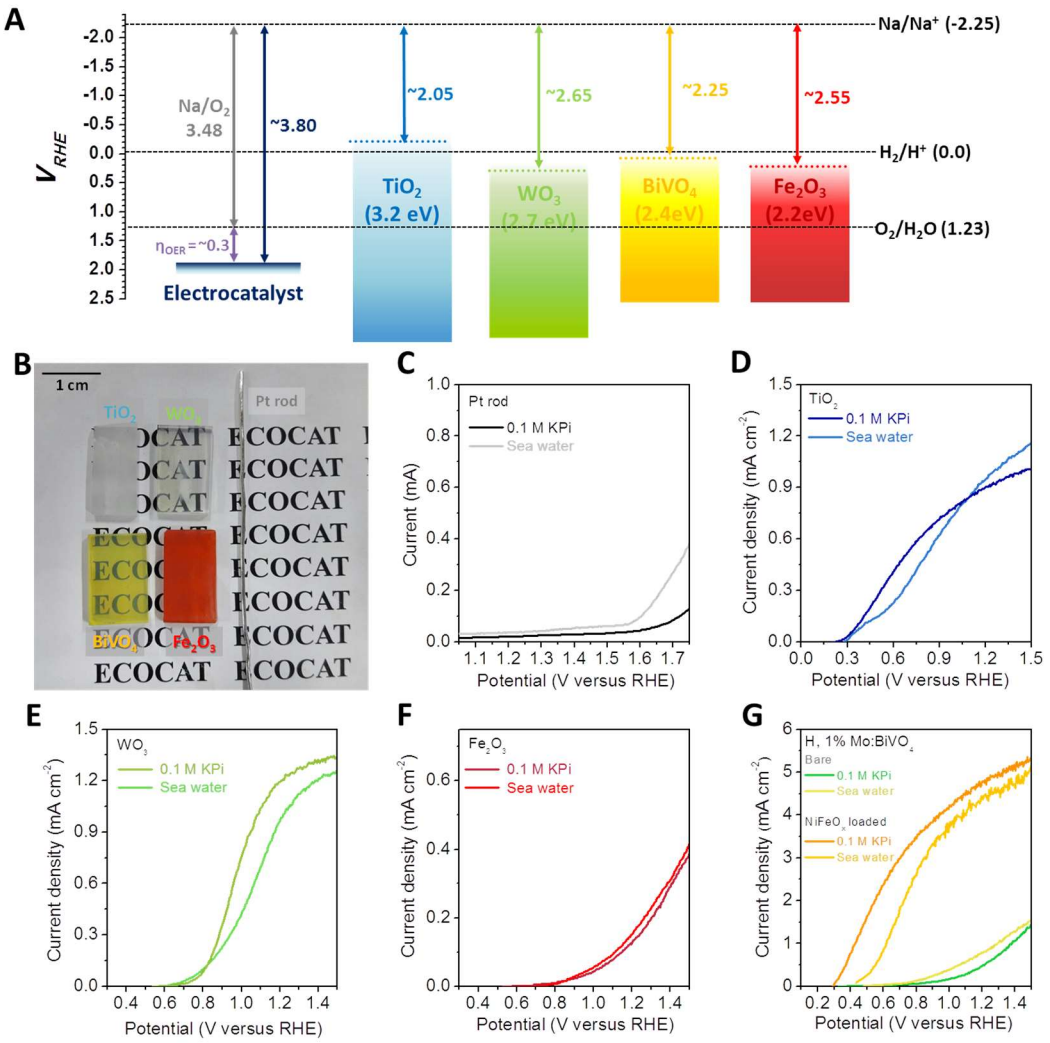

Figure S1. Band gap alignment of metal oxide light absorbers, related to Figure 2. (A) Energy diagram of the photo-charging process of semiconductor photoelectrodes for theoretically needed potential for seawater photocharging compared with Pt electrocatalyst; (B) picture images of used photoelectrode films (TiO_2, WO_3, Fe_2O_3, $BiVO_4$) and Pt rod as a model electrocatalyst; J-V curve of (C) Pt rod (3 cm^2), (D) TiO_2, (E) WO_3, (F) Fe_2O_3 and (G) H, 1% Mo:$BiVO_4$ with and without $NiFeO_x$ deposition in different electrolytes (0.1 M KPi (pH 7.0) and natural seawater (pH 8.0)). The photoelectrodes were tested under 1 sun irradiation (100 mW cm^{-2}).

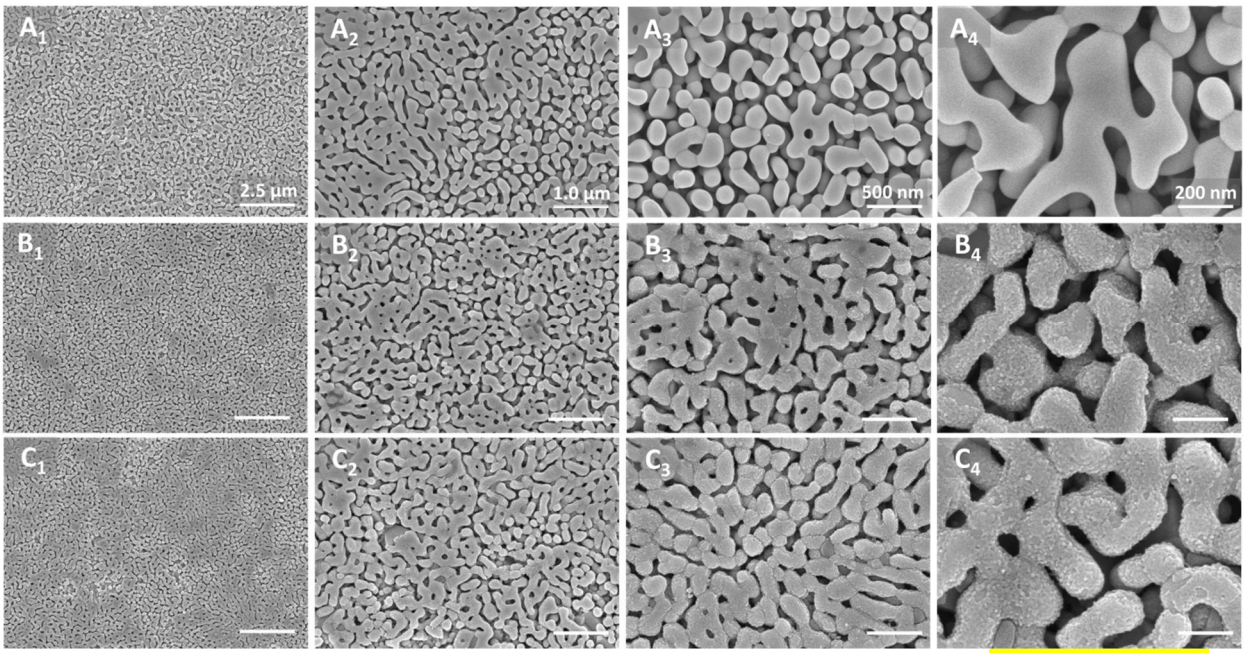

Figure S2. Scanning electron micrographs of $BiVO_4$ based photoelectrodes, related to Figure 3. (A) hydrogen treated Mo-doped $BiVO_4$ film (H, 1% Mo:$BiVO_4$), (B) $NiFeO_x$ loaded H, 1% Mo:$BiVO_4$ (right after deposition) and (C) $NiFeO_x$ loaded H, 1% Mo:$BiVO_4$ (after ~24 h of PEC reaction in sea water at applied bias of 1.03 V_{RHE}).

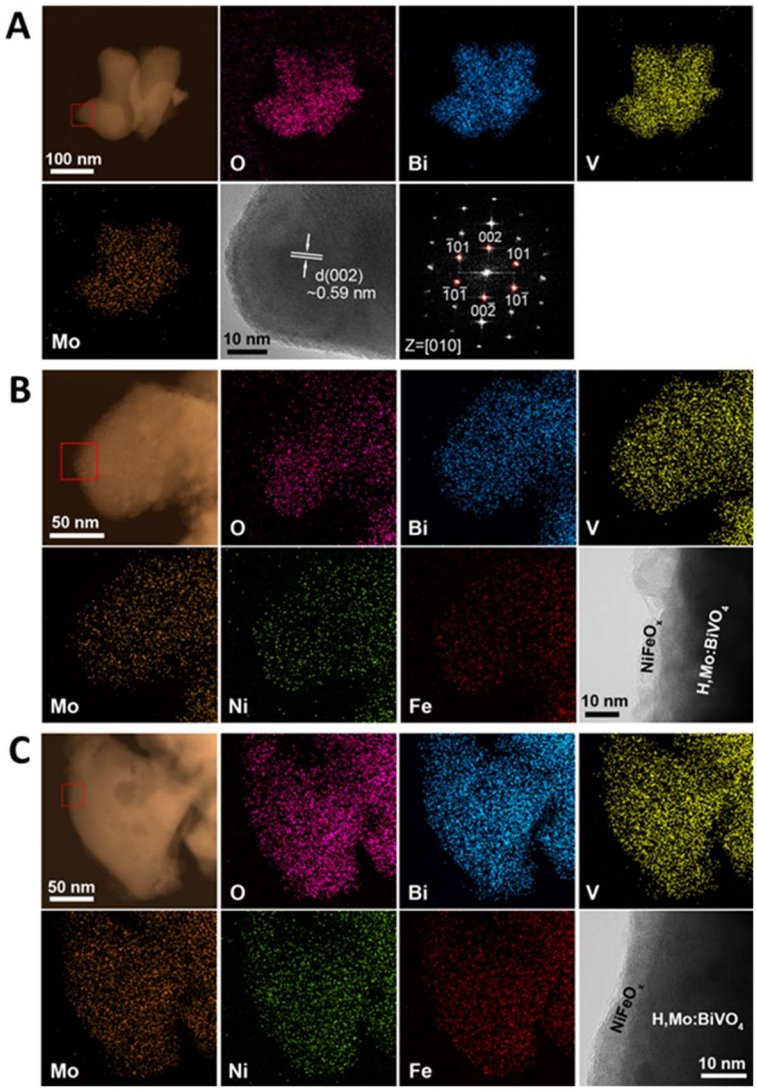

Figure S3. TEM-EDS mapping data of $BiVO_4$ based photoelectrodes,related to Figure 1. (A) bare and (B, C) $NiFeO_x$-coated H,Mo:$BiVO_4$ films. (b) and (C) show the microstructural characteristics before and after 12 h stability testing, respectively. Each HRTEM image displays the region highlighted by red box in the corresponding bright-field scanning TEM image. The last image in (A) shows a fast Fourier transform (FFT) pattern of the HRTEM image with a zone axis of [010].

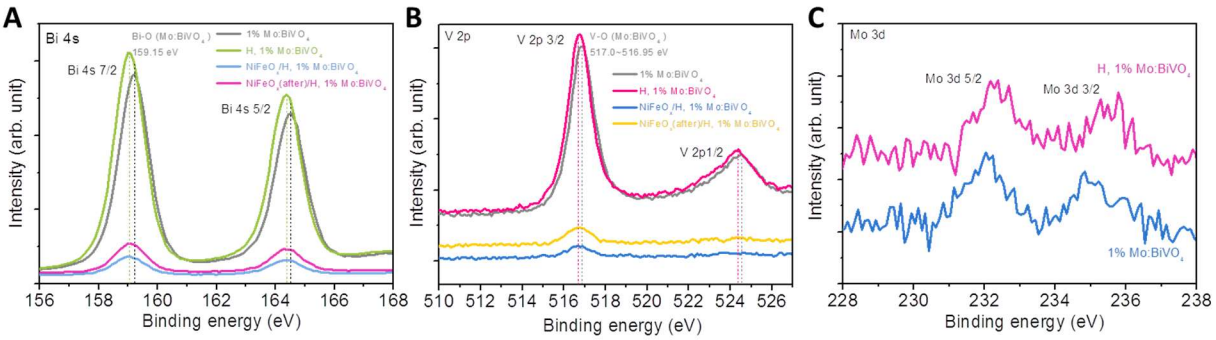

Figure S4. X-ray photoelectron spectra (XPS) of $BiVO_4$, related to Figure 3. (A) Bi 4f, (B) V 2p and (C) Mo 3d of 1% Mo:$BiVO_4$, H, 1% Mo: $BiVO_4$, $NiFeO_x$/H, 1% Mo: $BiVO_4$ right after OEC

deposition, and $NiFeO_x$/H, 1% Mo: $BiVO_4$ after PEC operation in seawater for 12 h under an applied bias of ~1.03 V_{RHE}.

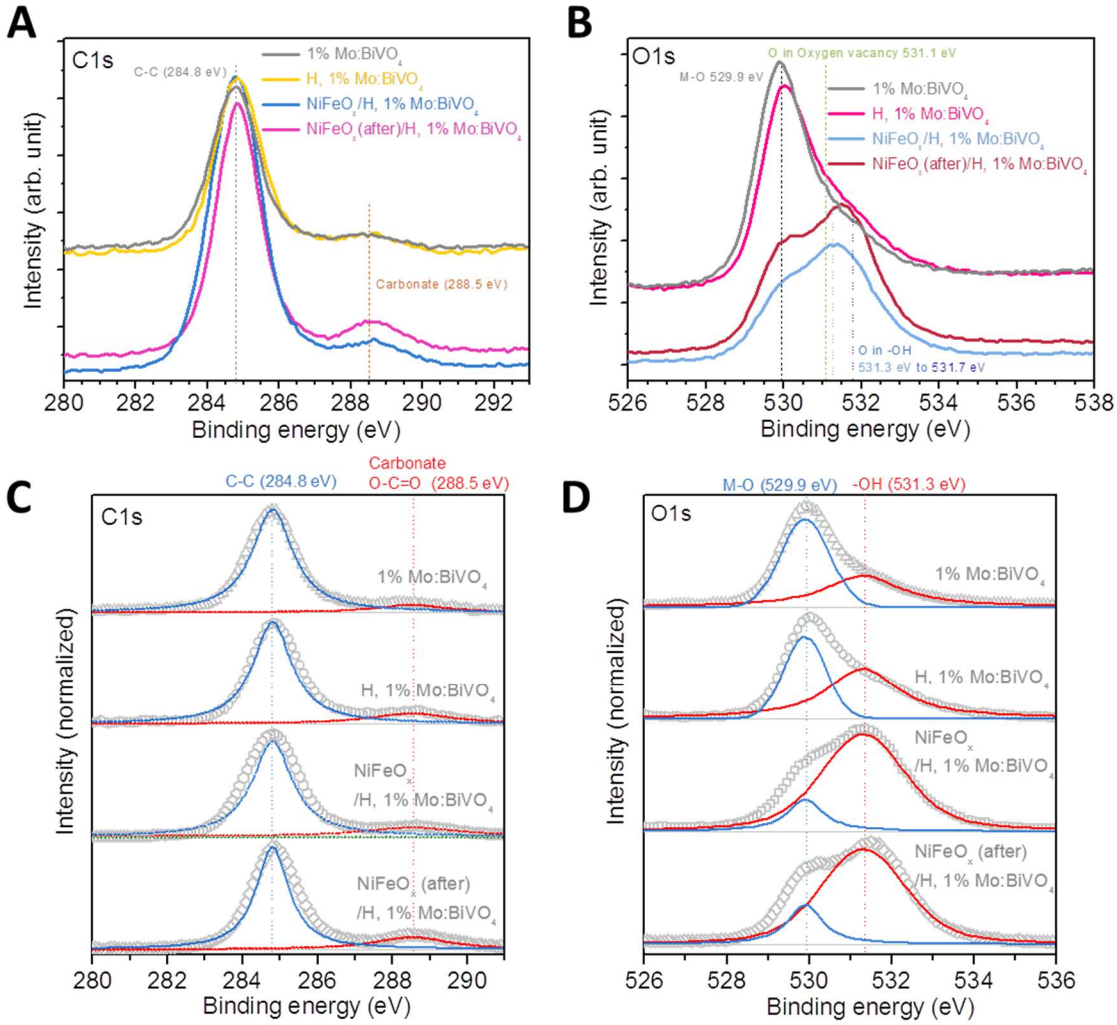

Figure S5. X-ray photoelectron spectra (XPS) of surface of $BiVO_4$ based photoelectrodes, related to Figure 3. (A, C) O 1s, (B, D) C 1s of 1% Mo:$BiVO_4$, H, 1% Mo: $BiVO_4$, $NiFeO_x$/H, 1% Mo: $BiVO_4$ (right after deposition), and $NiFeO_x$/H, 1% Mo: $BiVO_4$ after PEC operation in sea water for +12 h under applied bias of ~1.03 V_{RHE}).

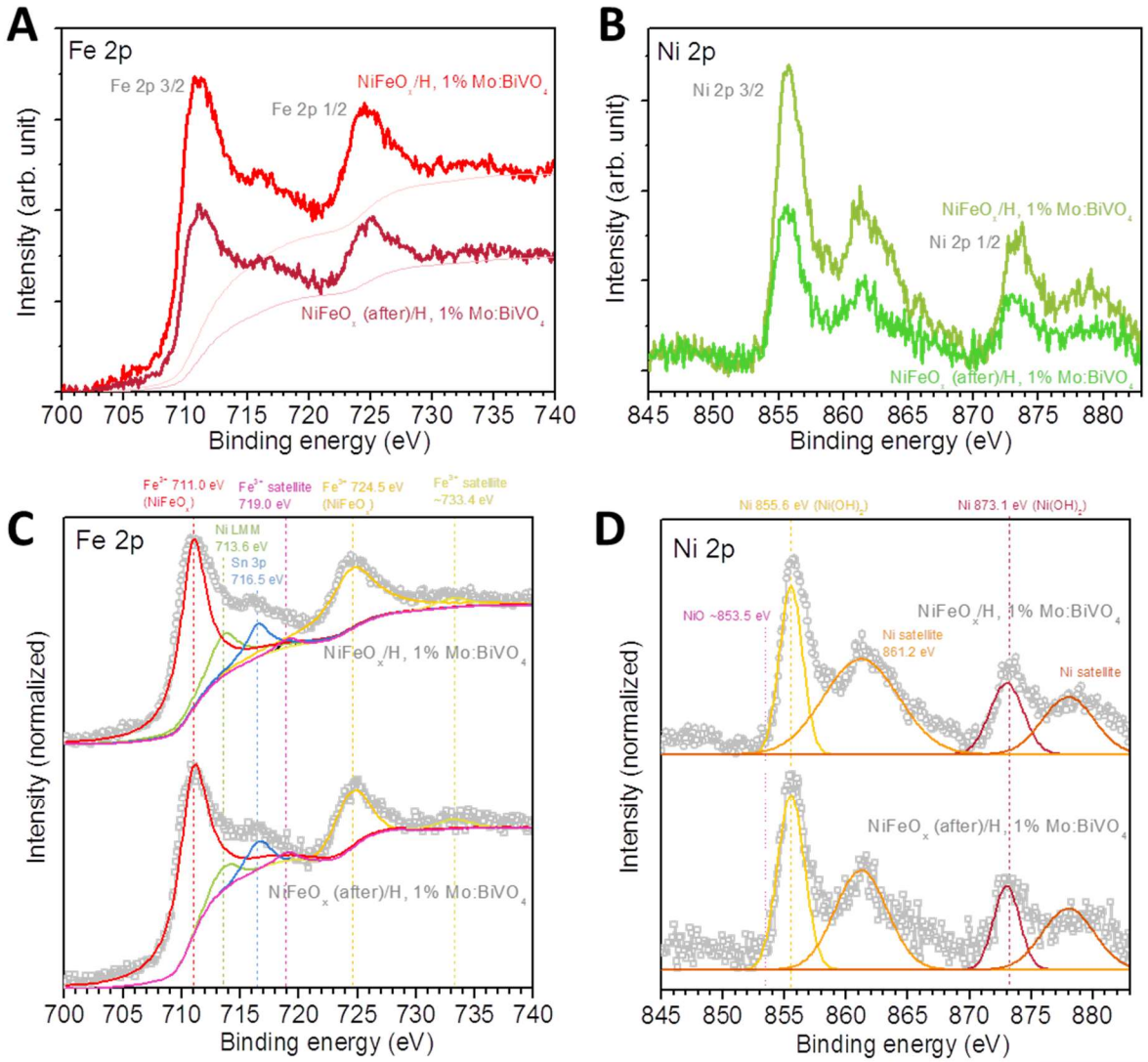

Figure S6. X-ray photoelectron spectra (XPS) of $BiVO_4$ based photoelectrodes, related to Figure 3. (A, C) Fe 2p, (B, D) Ni 2p of 1% Mo:$BiVO_4$, H, 1% Mo: $BiVO_4$, $NiFeO_x$/H, 1% Mo: $BiVO_4$ right after OEC deposition, and $NiFeO_x$/H, 1% Mo: $BiVO_4$ after PEC operation in seawater for 12 h under an applied bias of ~1.03 V_{RHE}. .

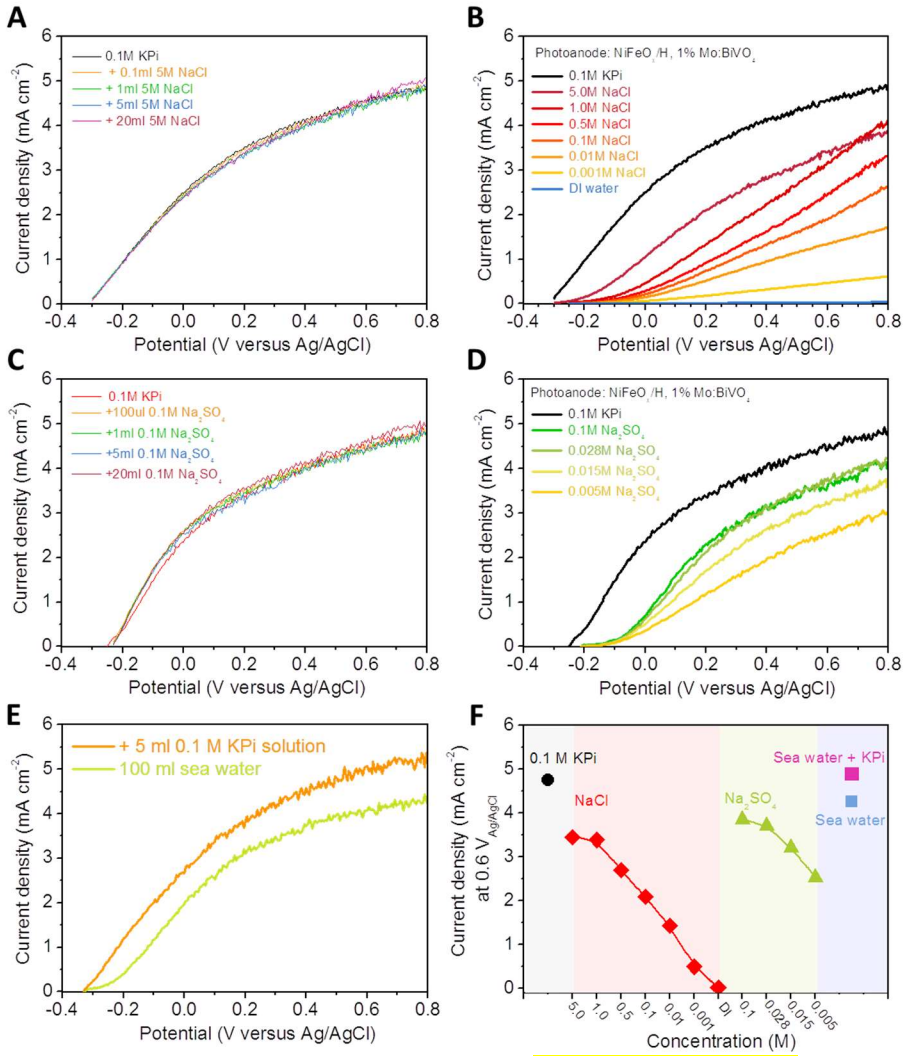

Figure S7. Effects of anions in electrolyte, related to Figure 3. J-V curve of $NiFeO_x$/H, 1% Mo:$BiVO_4$ photoelectrode with (A) addition of NaCl (*aq*) solutions to 0.1 M KPi, (B) various concentrations of NaCl as an electrolyte, (C) addition of Na_2SO_4 solution to 0.1 M KPi and (D) various concentrations of Na_2SO_4 as an electrolyte. The addition of both NaCl and Na_2SO_4 did not change the pH of 0.1 M KPi (pH 7.0). (E) J-V curve of $NiFeO_x$/H, 1% Mo:$BiVO_4$ photoelectrode in natural sea water and after addition of 5 ml KPi buffer solution. (F) Performance summary of KPi, NaCl, Na_2SO_4 and sea water as an electrolyte for PEC water splitting.

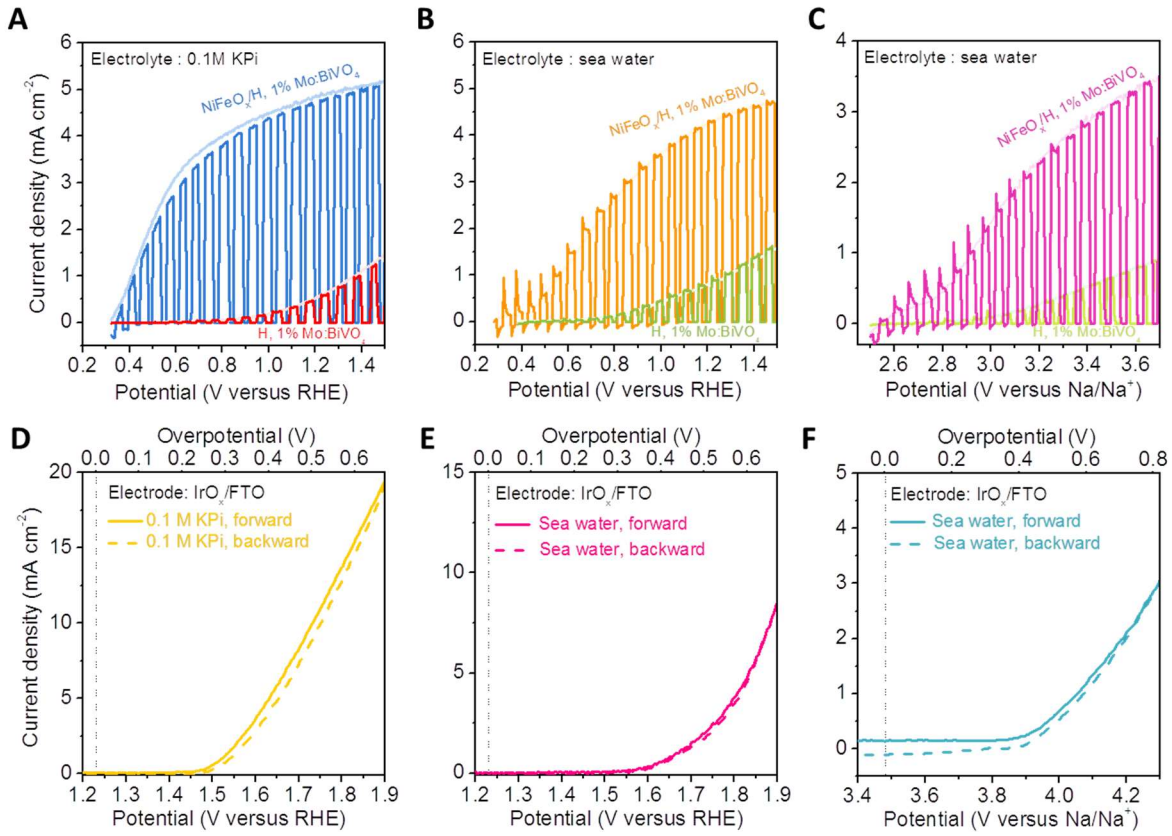

Figure S8. Effect of electrolytes on the (photo)electrochemical performance, related to Figure 3. ((A-C) $BiVO_4$ PE with/without $NiFeO_x$ OEC and (D-F) IrO_x/FTO electrode). Electrolyte condition was for (A, D) 0.1 M KPi (pH 7.0), (b, e) seawater (pH ~8.0) and (C, F) seawater cell (Na|seawater).

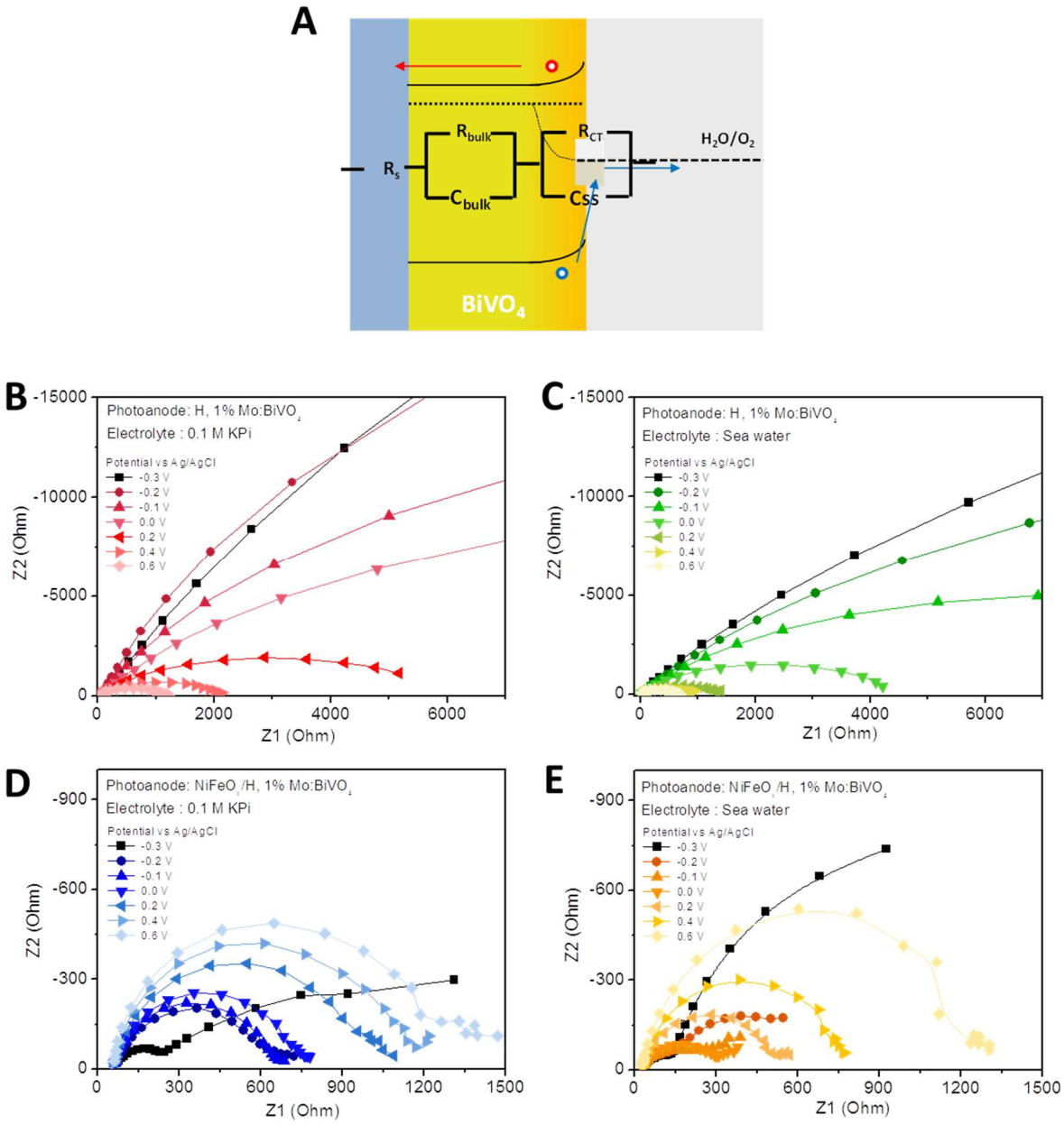

Figure S9. PEIS for $BiVO_4$ baed photoelectrodes, related to Figure 3. (A) Equivalent (modified Randle) circuit model for curve fitting and (B-E) PEIS of H, 1% Mo:$BiVO_4$ (B) in 0.1 M KPi, (C) in sea water and $NiFeO_x$/H, 1% Mo:$BiVO_4$ (D) in 0.1 M KPi and (E) sea water with different bias range (-0.3 – 0.6 V vs. Ag/AgCl).

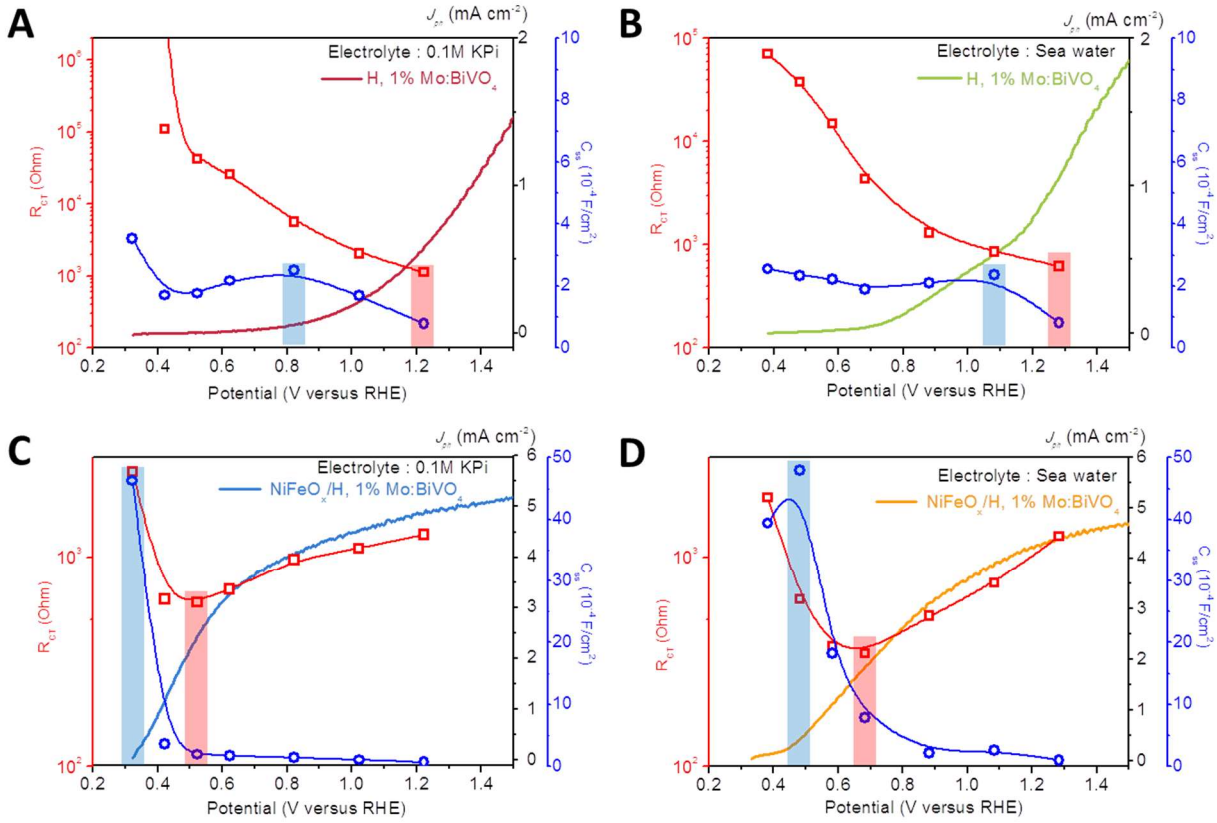

E

	H, 1% Mo:$BiVO_4$ (KPi)	H, 1% Mo:$BiVO_4$ (Sea water)	NiFeOx/H, 1% Mo:$BiVO_4$ (KPi)	NiFeOx/H, 1% Mo:$BiVO_4$ (Sea water)
Minimum R_{CT} (Ω) (potential)	1752	854	652	467
	~1.2	~1.2	0.45	0.66
Maximum C_{ss} (10^{4-} F/cm^2) (potential)	2.78	2.14	More than 50	48.3
	0.80	1.05	Less than 0.3	0.45
J (mA/cm^2) at 1.23 V_{RHE}	0.75	1.05	5.0	4.56
Onset potential (V_{RHE})	0.75	0.72	0.31	0.35

Figure S10. J-V curve of PE and its calculated capacitance of surface states (C_{ss}) and impedance (R_{CT}) calculated by equivalent circuit fitting of PEIS data in Figure S9, related to Figure 3. H, 1% Mo:$BiVO_4$ (A) in 0.1 M KPi, (B) in sea water and $NiFeO_x$/H, 1% Mo:$BiVO_4$ (C) in 0.1 M KPi and (D) sea water. (E) Table with parameters extracted from PEIS data.

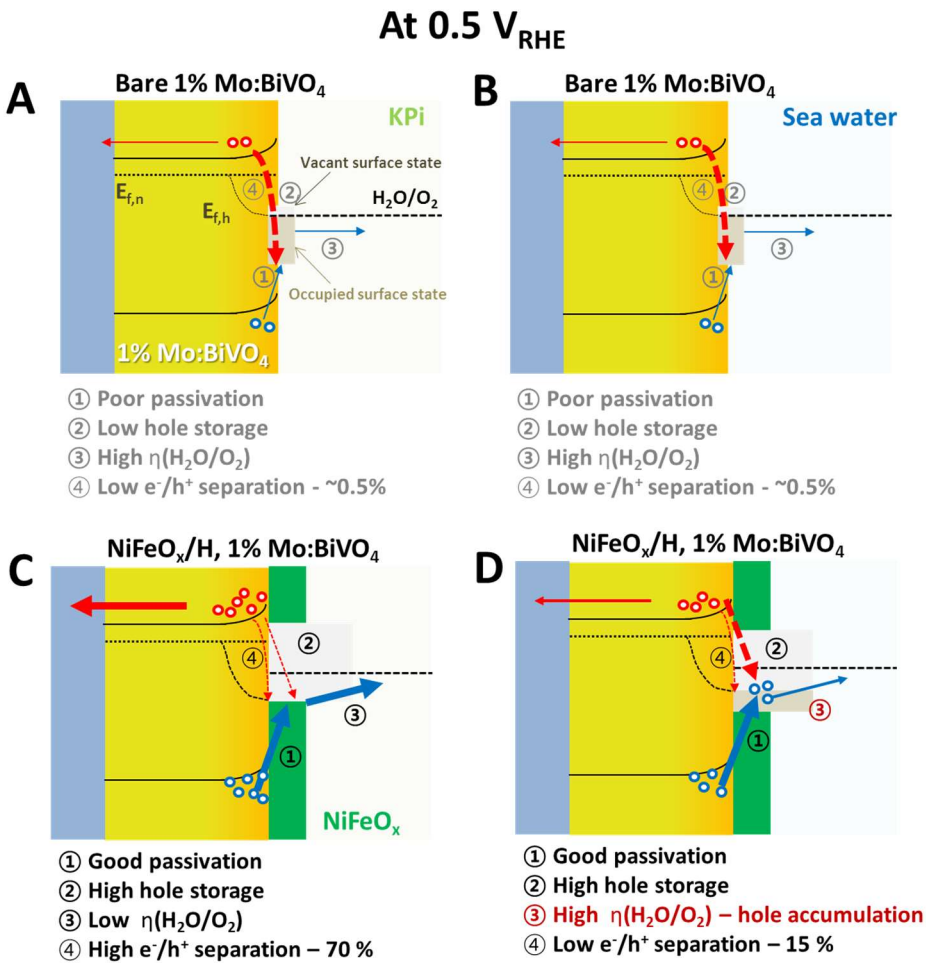

Figure S11. Schematic energy diagram showing the band bending and hole transfer pathway between the $BiVO_4$ PE and electrolyte ((A, B) in 0.1 M KPi and (C, D) in sea water), related to Figure 3. Bias applied for band bending was assumed to be ~0.5 V_{RHE}. Red and blue solid arrows represent electron and hole transfer pathways, respectively. Dotted arrows represent recombination pathways (backward from intended polarization of charge carriers).

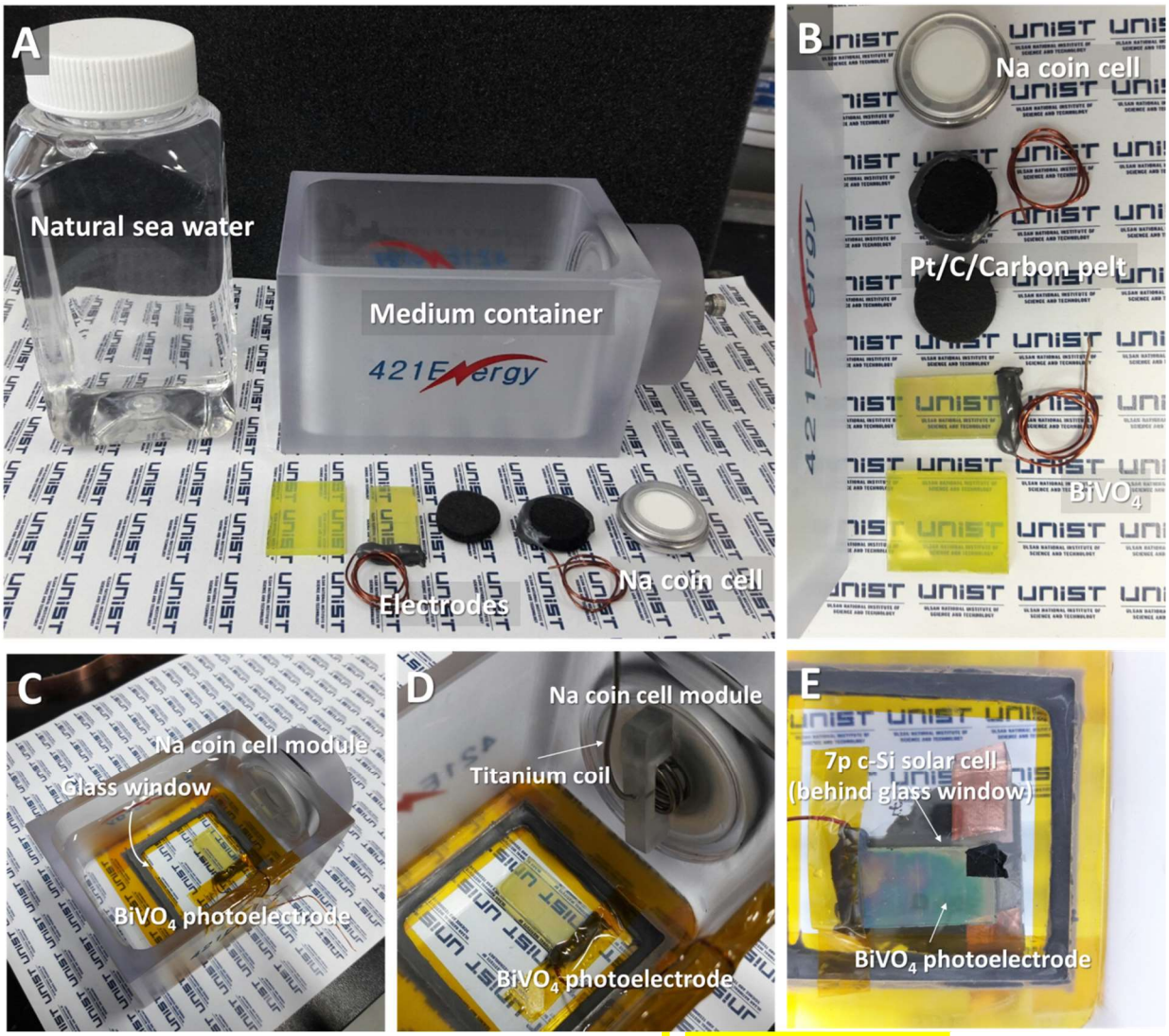

Figure S12. Basic setup for solar seawater battery, related to Figure 5. (A) Module composed of a seawater cell containing a Na metal anode, with only NASICON exposed to seawater, in which a PE and a cathode. (B) Magnified image. (C-E) PE – PV arrangement for unbiased sea water battery charge operation.

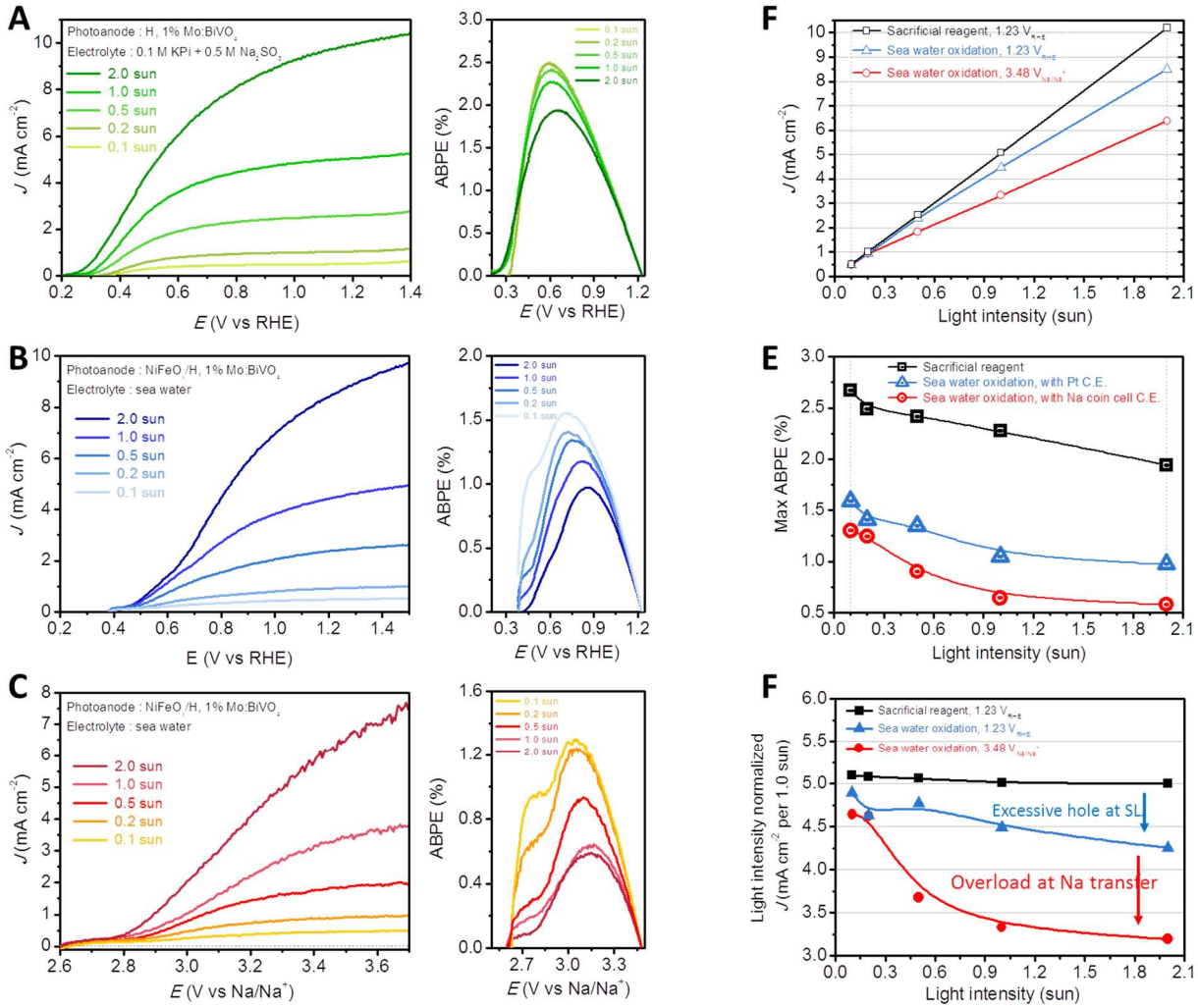

Figure S13. Light intensity dependence of overall performance of $BiVO_4$ PE and solar-seawater battery, related to Figure 4. (A) J-V curves and ABPE of $BiVO_4$ photoelectrode with various light intensities in a sacrificial reagent (0.1 M KPi + 0.5 M Na_2SO_3), (B) $NiFeO_x/BiVO_4$ in seawater (three-electrode configuration with a Pt counter electrode), and (C) solar-seawater cell with the $NiFeO_x/BiVO_4$ PE in seawater (two-electrode configuration). (D) Photocurrent density at short circuit condition (1.23 V_{RHE} or 3.48 V_{Na/Na^+}). (E) Maximum ABPE values. (F) Normalized photocurrent density (per 1.0 sun) of bare $BiVO_4$ PE in 0.1 M KPi+0.5M Na_2SO_3 sacrificial reagent (bare PE), $NiFeO_x$/ $BiVO_4$ PE in sea-water in a three-electrode system with a Pt counter electrode, and $NiFeO_x$/ $BiVO_4$ PE in the solar-seawater battery.

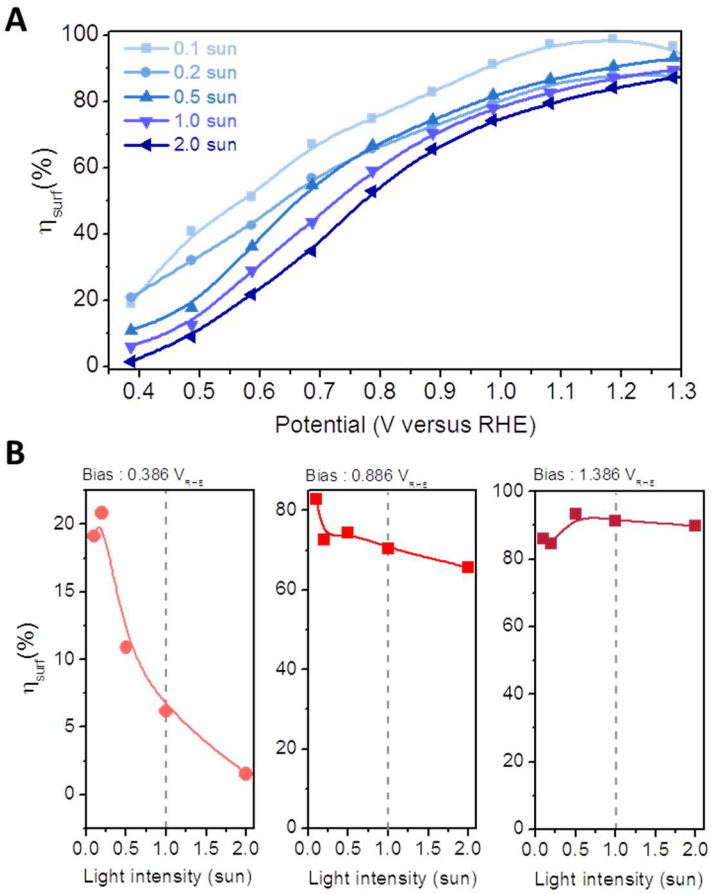

Figure S14. Surface charge separation efficiency (η_{surf}) of $NiFeO_x$/H, 1% Mo:$BiVO_4$ PE in seawater under various light intensities, related to Figure 4. The calculation of η_{surf} (A) depending on bias and (B) light intensity with different bias region (low/mid/high) which was made according to the procedure described in Materials and Methods section.

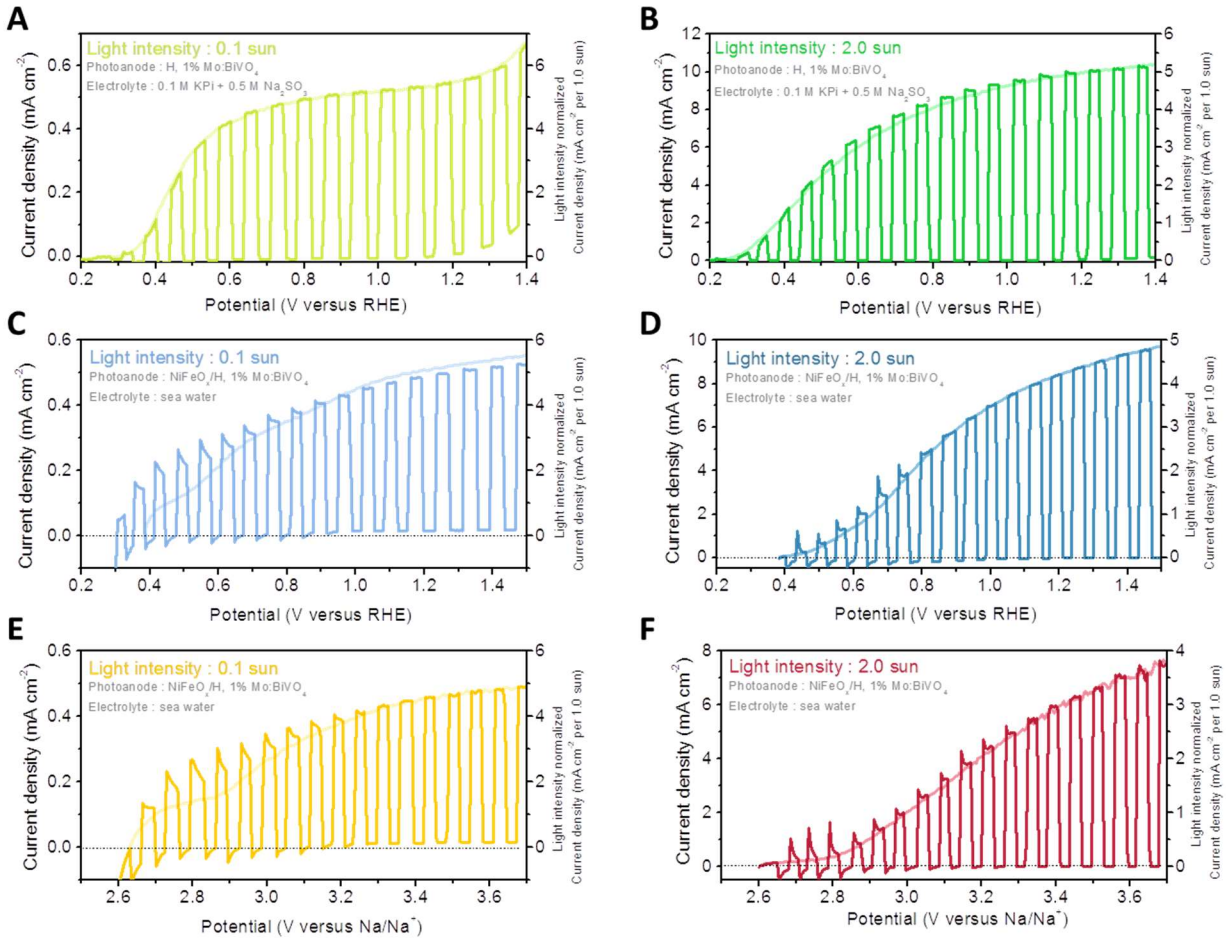

Figure S15. J-V curve of $BiVO_4$-based PE and solar-seawater battery under chopped illuminations of attenuated (0.1 sun) or intensified (2.0 sun) light source, related to Figure 4. J-V curve of the $BiVO_4$-based PE in (A, B) sacrificial reagent (0.1 M KPi + 0.5 M Na_2SO_3) and (C, D) seawater (in a three-electrode configuration with a Pt counter electrode) and (E, F) J-V curve of the solar-seawater battery with the $BiVO_4$ PE. Scan rate: 20 mV, forward scan.

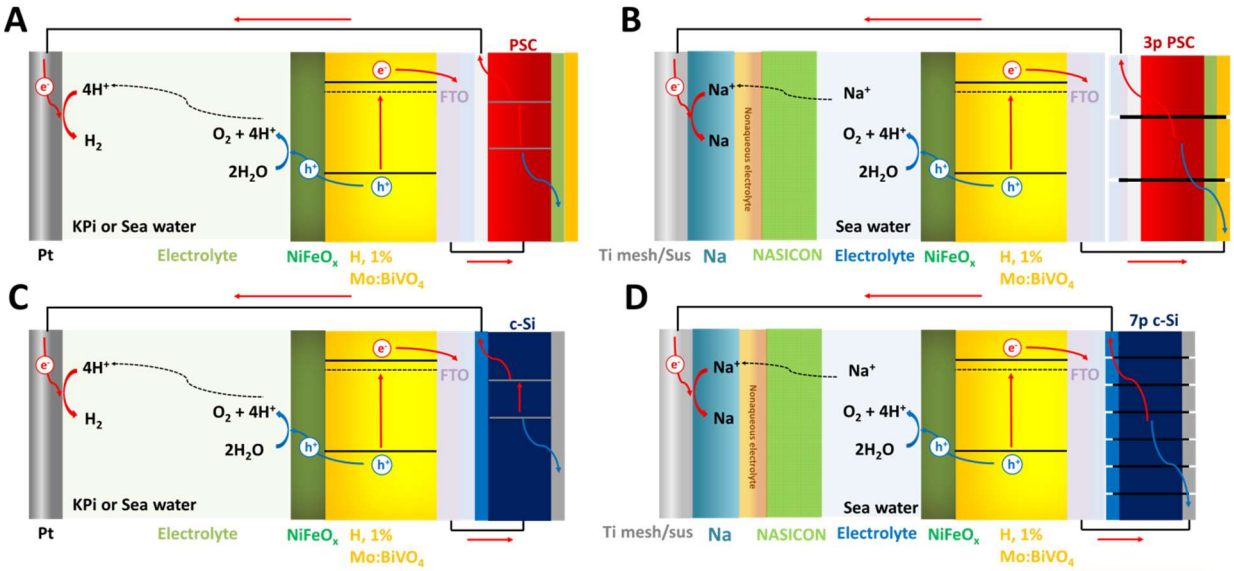

Figure S16. Schematics of tandem devices with a combination of PE-PV systems, related to Figure 5. (A, C) overall water splitting (redox system of H_2/O_2; E_{redox}=1.23 V) and (B, D) photo-charging of solar-seawater battery (redox system of Na/O_2; E_{redox}=3.48 V). The PE is $NiFeO_x$/H, 1% Mo:$BiVO_4$ and the PVs are PSC (A, B) or c-Si solar cell (C, D).

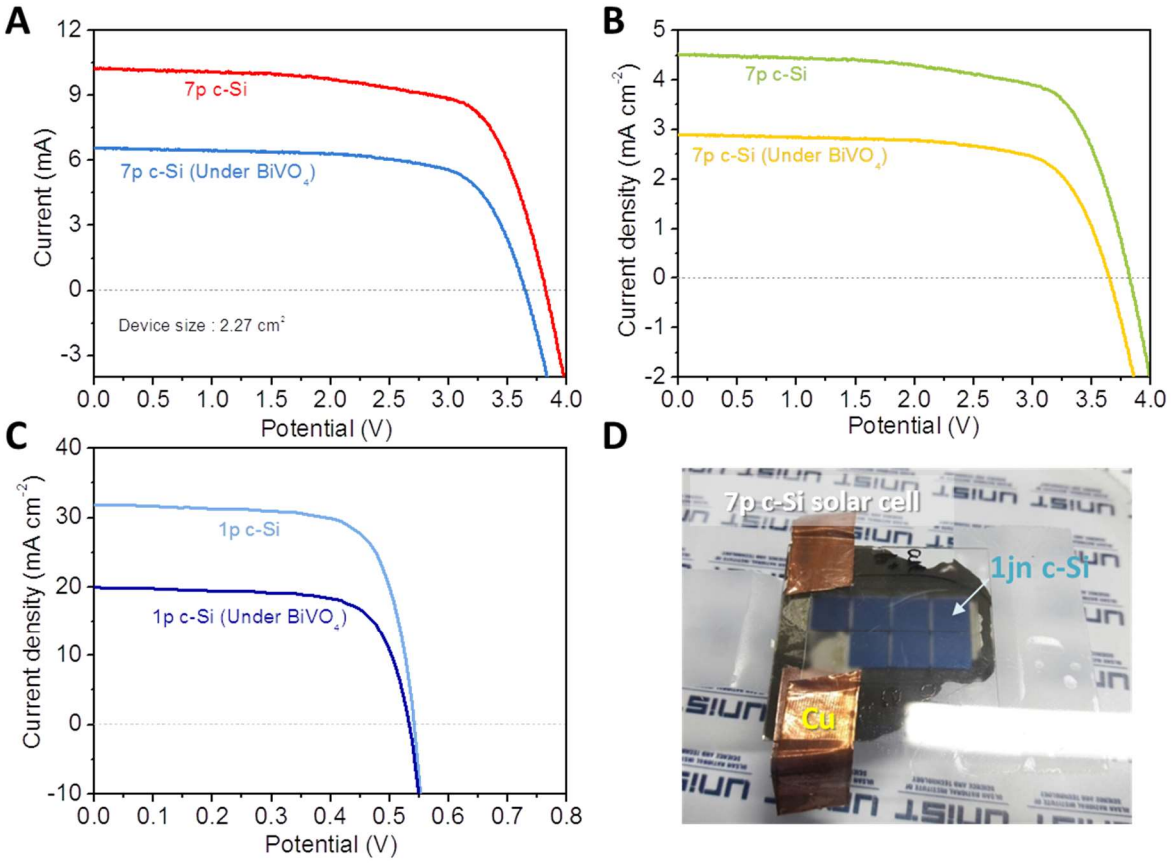

E

	V_{oc} (V)	J_{sc} (mA/cm²)	FF (%)	η (%)
1p c-Si Reference	0.58	31.3	72.2	12.6
1p c-Si Under $BiVO_4$	0.538	19.9	70.8	7.6
7p c-Si Reference	3.82	4.51	69.2	11.94
7p c-Si Under $BiVO_4$	3.64	2.89	70.0	7.37

Figure S17. **Performance of crystalline silicon PV, related to Figure 5.** J-V curves of 7 pieces crystalline silicon (denoted as 7 p c-Si) solar cell with/without the overlap of $NiFeO_x$/H, 1% Mo:$BiVO_4$ PE as front absorber for (A) per device (active area : 2.27 cm^2) and (B) per centimeter square unit (1.0 cm^2). (C) J-V curves of single piece c-Si solar cell with/without the overlap of $NiFeO_x$/H, 1% Mo:$BiVO_4$ PE. (D) Picture image of actual device of 7 p c-Si. (E) Performance of single or 7 pieces c-Si solar cell with/without H, 1% Mo:$BiVO_4$ film cover. Light intensity was 1 sun (AM 1.5G. 100 mW/cm^2).

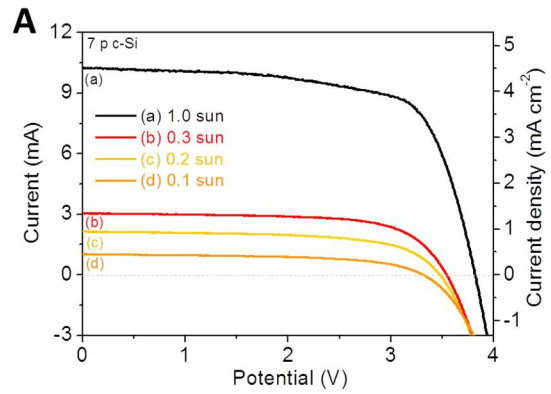

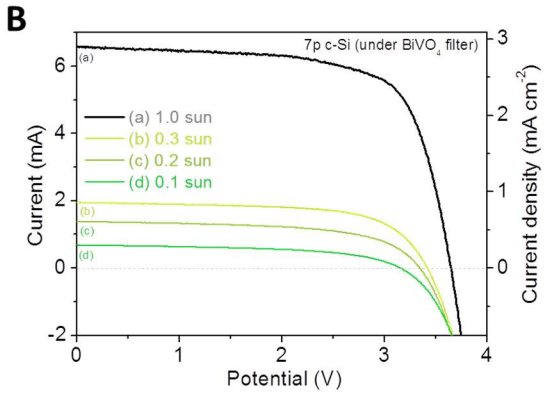

Light intensity	Power density (mW/cm²)	η (%)	J_{sc} (mA/cm²)	J_{sc} device	V_{oc} (V)	FF (%)
1.0 sun	11.94	11.94	4.51	10.24	3.82	69.2
0.3 sun	3.23	10.75	1.34	3.04	3.54	67.9
0.2 sun	2.07	10.35	0.95	2.15	3.47	62.9
0.1 sun	0.87	8.713	0.45	1.03	3.315	58.2

Light intensity	Power density (mW/cm²)	η (%)	J_{sc} (mA/cm²)	J_{sc} device	V_{oc} (V)	FF (%)
1.0 sun	7.37	7.37	2.89	6.56	3.64	70.0
0.3 sun	1.92	6.40	0.86	1.94	3.415	65.6
0.2 sun	1.21	6.09	0.61	1.38	3.345	60.1
0.1 sun	0.51	5.12	0.299	0.68	3.155	54.0

Figure S18. Effect of light intensity for crystalline silicon PV, related to Figure 5. J-V curves of 7p c-Si solar cell (A) without and (B) with the overlayer of $NiFeO_x$/H, 1% Mo:$BiVO_4$ PE under various light intensities (1.0, 0.3, 0.2, and 0.1 sun). The inset table indicates performance of device accordingly.

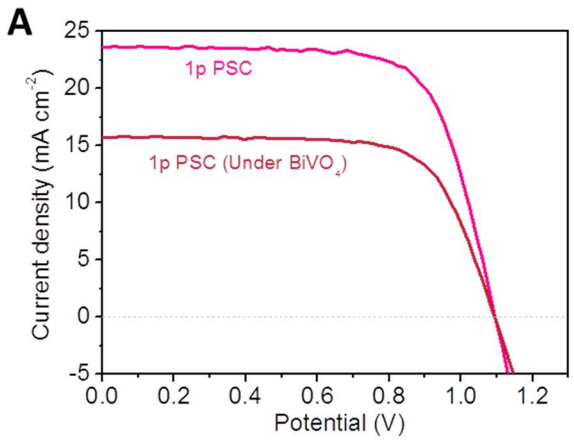

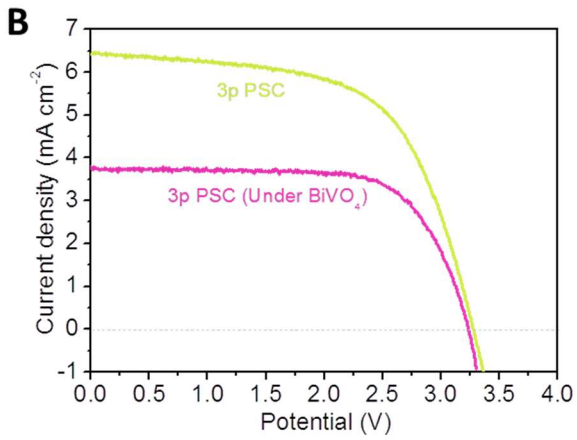

	V_{oc} (V)	J_{sc} (mA/cm²)	FF (%)	η (%)
Reference	1.096	23.59	71.25	18.43
With $BiVO_4$	1.094	15.71	70.60	12.14

	V_{oc} (V)	J_{sc} (mA/cm²)	FF (%)	η (%)
Reference	3.28	6.49	61.3	12.05
With $BiVO_4$	3.23	3.64	68.2	7.73

Figure S19. Performance of lead halide based pervoskite PV, related to Figure 5. J-V curves of (A) single piece and (B) 3 pieces PSCs connected in series with/without the overlay of $NiFeO_x$/H, 1% Mo:$BiVO_4$ PE. Inset table indicates performance of devices. Light intensity was 1 sun (AM 1.5G, 100 mW/cm²).

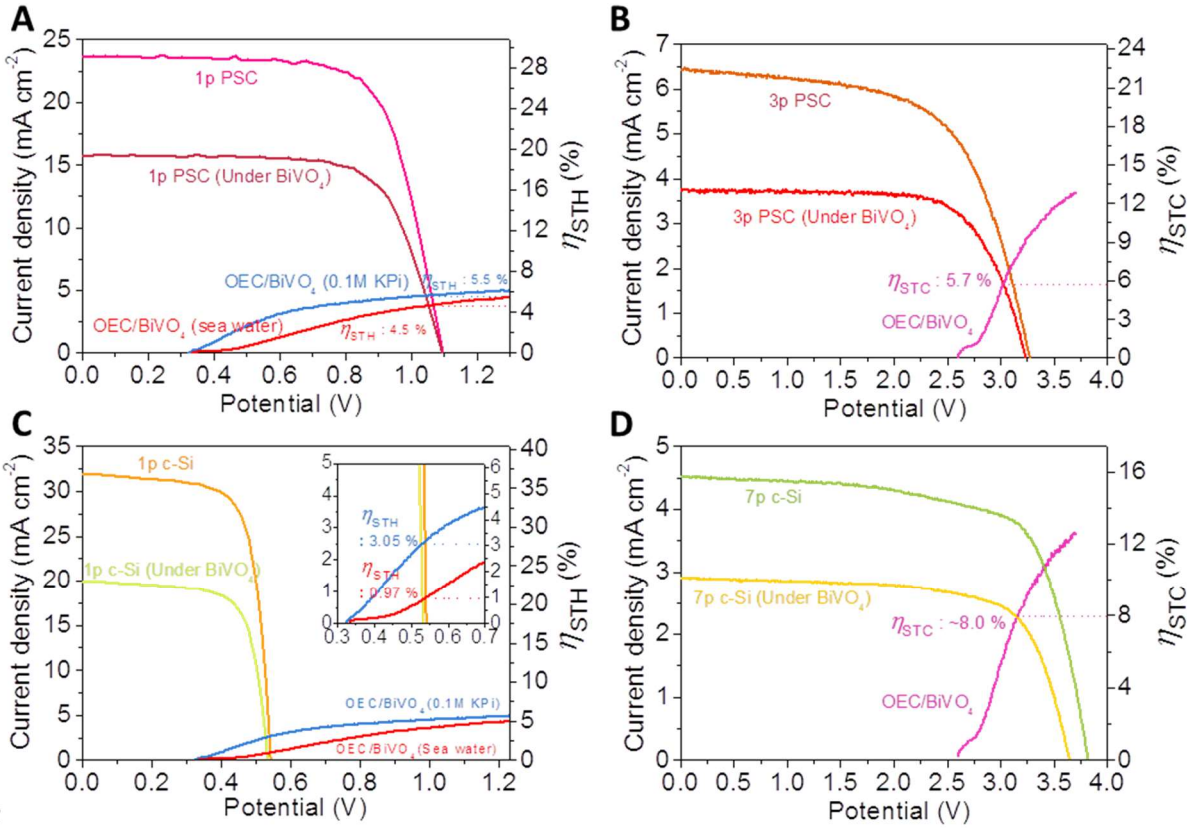

E

Device (operating electrolyte)	*Solar cell PCE (%)*	Redox system (voltage)	*Solar to energy (%)*	Solar to energy/solar cell PCE (%)
$BiVO_4$- 1p Perovskite (0.1 M KPi)	18.43	H_2/O_2 (1.23)	5.5	29.84
$BiVO_4$- 1p Perovskite (sea water)	18.43		4.05	21.98
$BiVO_4$- 1p c-Si (0.1 M KPi)	12.6		3.05	24.21
$BiVO_4$- 1p c-Si (sea water)	12.6		0.97	7.69
$BiVO_4$- 3p Perovskite (sea water)	12.05	Na/O_2 (3.48)	5.7	47.30
$BiVO_4$- 7p c-Si (sea water)	11.94		8.0	67.00

Figure S20. Comparison of PE-PV system for solar hydrogen production or solar battery charging, related to Figure 5. J-V curves of photoelectrodes (three electrode for (A, C), two electrode for (B, D) with Na coin cell counter electrode) and PV device (two electrode configuration). Photoelectrode – PSC for (A) overall water splitting and (B) photo-charging of solar-seawater battery with photoelectrode – c-Si solar cell for (B) overall water splitting and (D) solar-sea battery. Device size: $NiFeO_x$/H, 1% Mo:$BiVO_4$ (0.25 cm^2), 1p PSC (0.15 cm^2), 3p PSC (0.45 cm^2), 1p c-Si (0.324 cm^2), 7p c-Si (2.27 cm^2). (E) Table for comparison of efficiency (PCE, η_{STH}, η_{STC}) of device types.

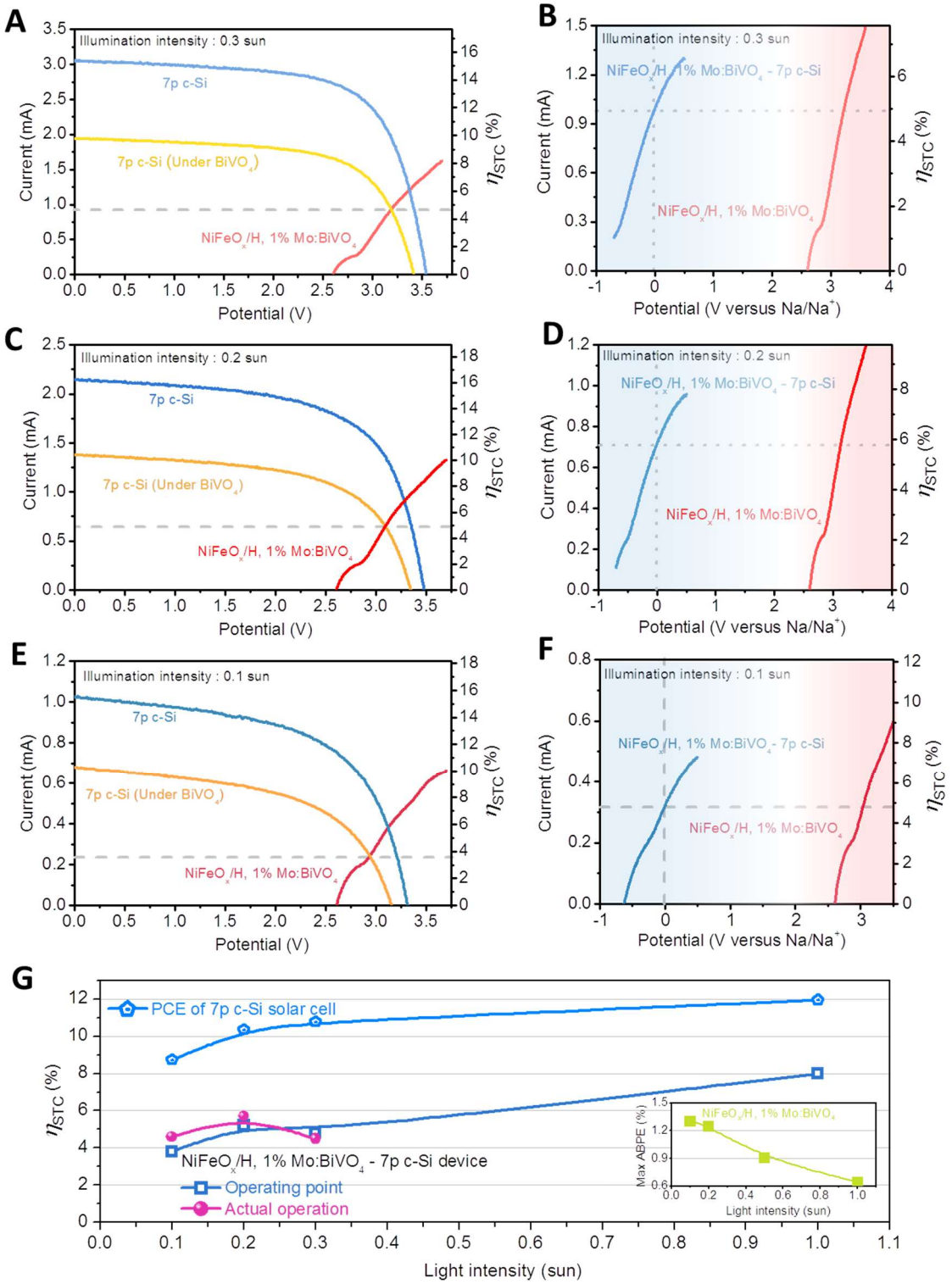

Figure S21. Performance of solar-seawater battery with PE-PV tandem assemblies under attenuated sun, related to Figure 5. (A, C, E) operating point and (B, D, F) actual operation. (A, B – 0.3 sun, C, D – 0.2 sun, E, F – 0.1 sun). (G) Summarized power conversion efficiency (PCE) of PV (7p c-Si solar cell module) and solar to chemical conversion efficiency of PE – PV device under various light intensities (the inset shows the PE's ABPE value under various light intensities). PE: $NiFeO_x$/H, 1% Mo:$BiVO_4$; operating electrolyte: natural seawater. The actual photo-charging operation was conducted with illumination areas of 2.30 cm^2 for the PE and 2.27 cm^2 for the PV.

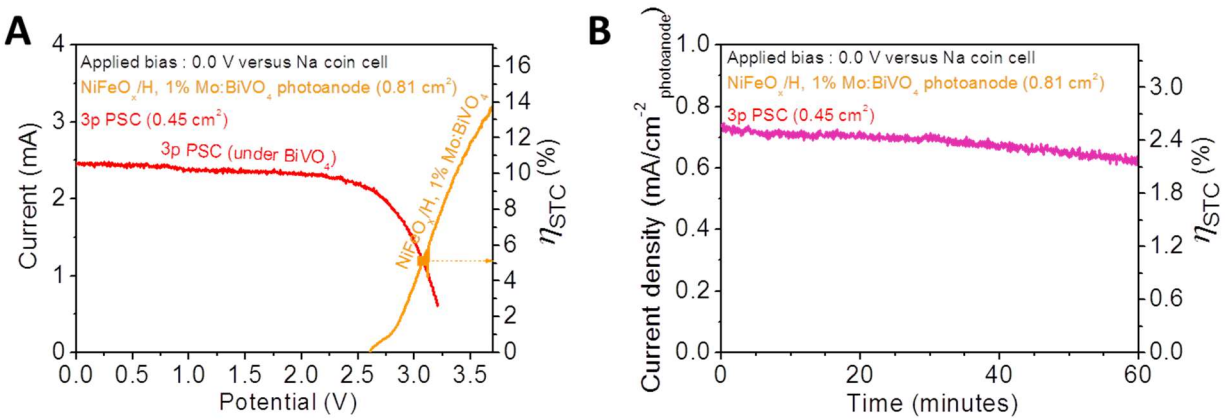

Figure S22. $BiVO_4$ – 3p PSC for unbiased solar battery charge, related to Figure 5. J-V curves of photoelectrode and PV device (two electrode configuration). Device size: $NiFeO_x$/H, 1% Mo:$BiVO_4$ (0.81 cm^2), 3p perovskite (0.45 cm^2). Solar–to-chemical energy conversion efficiency was calculated by using the illumination area of the $BiVO_4$ photoelectrode (0.81 cm^2)

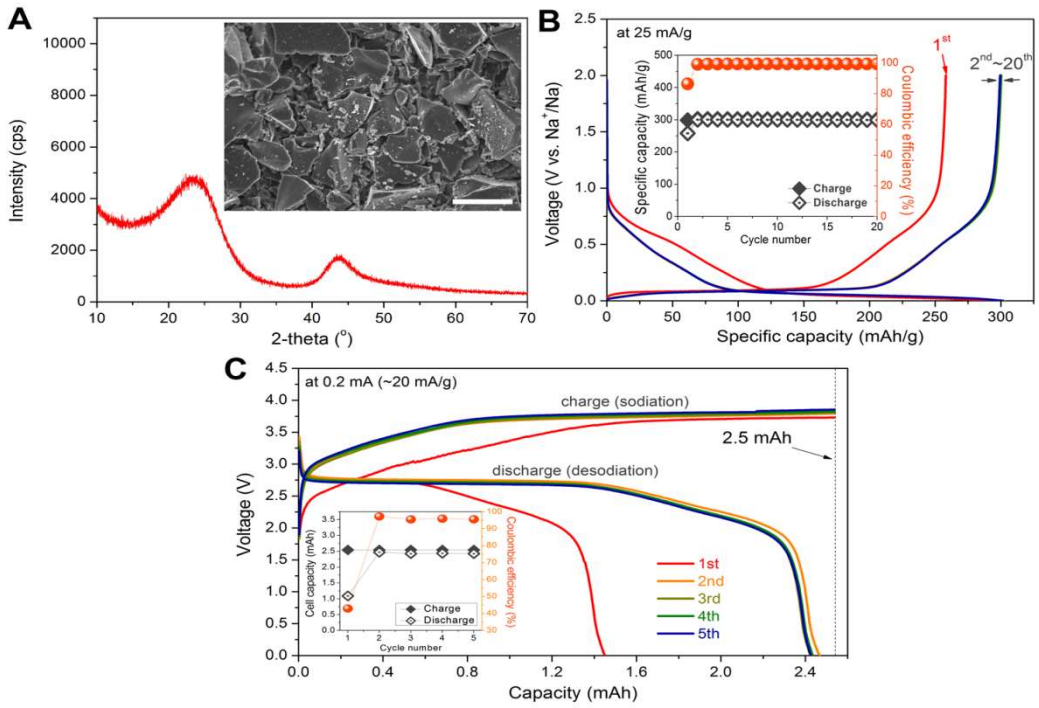

Figure S23. Structural and electrochemical characterizations of hard carbon anode as charge storage electrode, related to Figure 5. (A) XRD pattern and SEM image (inset) of hard carbon particles. The scale bar indicate 10 µm. (B) Galvanostatic charge-discharge voltage profile measured using a 2032 coin-type half cell (Na|hard carbon) at a current rate of 25 mA/g,$_{\text{hard carbon}}$. The inset shows the reversible a specific capacity of ~300 mAh/g and a coulombic efficiency of ~100% of the hard carbon anode during 20 cycles. (C) Galvanostatic charge-discharge voltage profile of a seawater battery with the hard carbon anode (hard carbon|seawater) at a current of 0.2 mA (~20 mA/g,$_{\text{hard carbon}}$) with a capacity cut-off of 2.5 mAh (~250 mAh·g^{-1},$_{\text{hard carbon}}$) upon charging and at a voltage cut-off of 0 V upon discharging. The inset shows the charge/discharge capacity and coulombic efficiency of the hard carbon anode during 5 cycles.

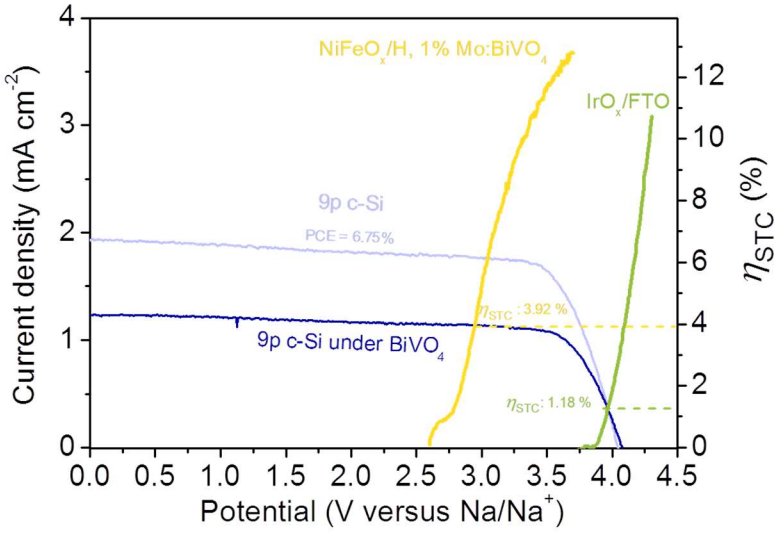

Figure S24. Comparison of PV-EC and PE-PV for solar battery charge, related to Figure 5. Operating point for simple connection of PV and IrO_x/FTO OEC-derived Na production compared with NiFeOx/$BiVO_4$ PE-seawater cell**.** As PV, 9p c-Si was used under attenuated 0.1 sun. Nearly 3 times higher efficiency is expected for PE-PV device (η_{STC} = 3.92 %) than that for OEC-PV device (η_{STC} = 1.18 %). Since PE has larger band gap as well as high photovoltage by itself (1.3 V), it is energetically more favorable to combine dual light absorber system instead of single one for maximizing solar energy harvesting.

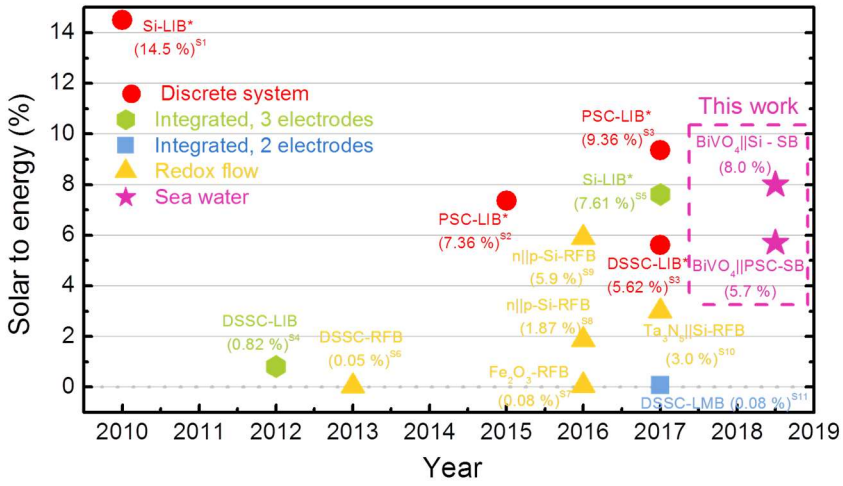

Figure S25. Comparison of solar energy conversion efficiency achieved by various light absorbers and battery systems, related to Figure 5. Si - silicon solar cell, DSSC: dye sensitized solar cell, PSC, perovskite solar cell, LIB: lithium ion battery, RFB: redox flow battery, LMB: lithium-metal battery, SB: sea water battery, respectively. The figure is based on Gurung and Qiao in "Progress of Solar Charging Batteries over the Years"(Gurung and Qiao, 2018). The superscripts denote references S1(Gibson and Kelly, 2010), S2(Xu et al., 2015a), S3(Ashim et al., 2017), S4(Guo et al., 2012), S5(Um et al., 2017), S6(Liu et al., 2013), S7(Wedege et al., 2016), S8(Li et al., 2016c), S9(Liao et al., 2016), S10(Cheng et al., 2017), S11(Ashim et al., 2017). The references highlighted by asterisk (*) indicates solar to electricity conversion efficiency.

Supplementary Video

Movie S1 Outdoor solar energy charged Na coin cell, related to Figure 5

References

Abirami, M., Hwang, S.M., Yang, J., Senthilkumar, S.T., Kim, J., Go, W.-S., Senthilkumar, B., Song, H.-K., and Kim, Y. (2016). A Metal–Organic Framework Derived Porous Cobalt Manganese Oxide Bifunctional Electrocatalyst for Hybrid Na–Air/Seawater Batteries. ACS Appl Mater Interfaces *8*, 32778-32787.

Akuto, K., and Sakurai, Y. (2001). A Photorechargeable Metal Hydride/Air Battery. J Electrochem Soc *148*, A121-A125.

Akuto, K., Takahashi, M., and Sakurai, Y. (2001). Photo-electrochemical characteristics of a cobalt–air cell using an anode active material–semiconductor (Co–GaP) hybrid electrode. J Power Sources *103*, 72-79.

Ashim, G., Ke, C., Reza, K., Saad, A.S., Geetha, V., Rajesh, P., Roya, N., and Qiquan, Q. (2017). Highly Efficient Perovskite Solar Cell Photocharging of Lithium Ion Battery Using DC–DC Booster. Adv Energy Mater *7*, 1602105.

Azevedo, J., Seipp, T., Burfeind, J., Sousa, C., Bentien, A., Araújo, J.P., and Mendes, A. (2016). Unbiased solar energy storage: Photoelectrochemical redox flow battery. Nano Energy *22*, 396-405.

Blankenship, R.E., Tiede, D.M., Barber, J., Brudvig, G.W., Fleming, G., Ghirardi, M., Gunner, M.R., Junge, W., Kramer, D.M., Melis, A.*, et al.* (2011). Comparing Photosynthetic and Photovoltaic Efficiencies and Recognizing the Potential for Improvement. Science *332*, 805-809.

Chen, Z., Concepcion, J.J., Song, N., and Meyer, T.J. (2014). Chloride-assisted catalytic water oxidation. Chem Commun *50*, 8053-8056.

Cheng, Q., Fan, W., He, Y., Ma, P., Vanka, S., Fan, S., Mi, Z., and Wang, D. (2017). Photorechargeable High Voltage Redox Battery Enabled by Ta3N5 and GaN/Si Dual-Photoelectrode. Adv Mater *29*, 1700312-n/a.

Cook, T.R., Dogutan, D.K., Reece, S.Y., Surendranath, Y., Teets, T.S., and Nocera, D.G. (2010). Solar Energy Supply and Storage for the Legacy and Nonlegacy Worlds. Chem Rev *110*, 6474-6502.

Dionigi, F., Reier, T., Pawolek, Z., Gliech, M., and Strasser, P. (2016). Design Criteria, Operating Conditions, and Nickel–Iron Hydroxide Catalyst Materials for Selective Seawater Electrolysis. ChemSusChem *9*, 962-972.

Fan, L., Jia, C., Zhu, Y.G., and Wang, Q. (2017). Redox Targeting of Prussian Blue: Toward Low-Cost and High Energy Density Redox Flow Battery and Solar Rechargeable Battery. ACS Energy Lett *2*, 615-621.

Gibson, T.L., and Kelly, N.A. (2010). Solar photovoltaic charging of lithium-ion batteries. J Power Sources *195*, 3928-3932.

Guo, W., Xue, X., Wang, S., Lin, C., and Wang, Z.L. (2012). An Integrated Power Pack of Dye-Sensitized Solar Cell and Li Battery Based on Double-Sided TiO2 Nanotube Arrays. Nano Lett *12*, 2520-2523.

Gurung, A., and Qiao, Q. (2018). Solar Charging Batteries: Advances, Challenges, and Opportunities. Joule *2*, 1217-1230.

Huang, L., Li, R., Chong, R., Liu, G., Han, J., and Li, C. (2014). Cl- making overall water splitting possible on TiO2-based photocatalysts. Catalysis Science & Technology *4*, 2913-2918.

Iguchi, S., Miseki, Y., and Sayama, K. (2018). Efficient hypochlorous acid (HClO) production via photoelectrochemical solar energy conversion using a BiVO4-based photoanode. Sustainable Energy & Fuels *2*, 155-162.
Kim, G., Oh, M., and Park, Y. (2016a). Solar-rechargeable battery based on photoelectrochemical water oxidation: Solar water battery. Sci Rep *6*, 33400.
Kim, J.-K., Mueller, F., Kim, H., Bresser, D., Park, J.-S., Lim, D.-H., Kim, G.-T., Passerini, S., and Kim, Y. (2014a). Rechargeable-hybrid-seawater fuel cell. Npg Asia Materials *6*, e144.
Kim, J.H., Hansora, D., Sharma, P., Jang, J.-W., and Lee, J.S. (2019). Toward practical solar hydrogen production – an artificial photosynthetic leaf-to-farm challenge. Chem Soc Rev *48*, 1908-1971.
Kim, J.H., Jang, J.-W., Jo, Y.H., Abdi, F.F., Lee, Y.H., van de Krol, R., and Lee, J.S. (2016b). Hetero-type dual photoanodes for unbiased solar water splitting with extended light harvesting. Nat Commun *7*, 13380.
Kim, J.H., Jang, J.W., Kang, H.J., Magesh, G., Kim, J.Y., Kim, J.H., Lee, J., and Lee, J.S. (2014b). Palladium oxide as a novel oxygen evolution catalyst on BiVO4 photoanode for photoelectrochemical water splitting. J Catal *317*, 126-134.
Kim, J.H., Jo, Y., Kim, J.H., Jang, J.W., Kang, H.J., Lee, Y.H., Kim, D.S., Jun, Y., and Lee, J.S. (2015a). Wireless Solar Water Splitting Device with Robust Cobalt-Catalyzed, Dual-Doped BiVO4 Photoanode and Perovskite Solar Cell in Tandem: A Dual Absorber Artificial Leaf. ACS Nano *9*, 11820-11829.
Kim, J.H., Lee, B.J., Wang, P., Son, M.H., and Lee, J.S. (2016c). Facile surfactant driven fabrication of transparent WO3 photoanodes for improved photoelectrochemical properties. Applied Catalysis A: General *521*, 233-239.
Kim, J.H., and Lee, J.S. (2019). Elaborately Modified BiVO4 Photoanodes for Solar Water Splitting. Adv Mater *0*, 1806938.
Kim, J.H., Magesh, G., Kang, H.J., Banu, M., Kim, J.H., Lee, J., and Lee, J.S. (2015b). Carbonate-coordinated cobalt co-catalyzed BiVO4/WO3 composite photoanode tailored for CO2 reduction to fuels. Nano Energy *15*, 153-163.
Kim, T.W., and Choi, K.-S. (2014). Nanoporous BiVO4 Photoanodes with Dual-Layer Oxygen Evolution Catalysts for Solar Water Splitting. Science *343*, 990-994.
Kim, T.W., Ping, Y., Galli, G.A., and Choi, K.-S. (2015c). Simultaneous enhancements in photon absorption and charge transport of bismuth vanadate photoanodes for solar water splitting. Nat Commun *6*, 8769.
Kim, Y., Kim, H., Park, S., Seo, I., and Kim, Y. (2016d). Na ion- Conducting Ceramic as Solid Electrolyte for Rechargeable Seawater Batteries. Electrochim Acta *191*, 1-7.
Kuang, Y., Jia, Q., Ma, G., Hisatomi, T., Minegishi, T., Nishiyama, H., Nakabayashi, M., Shibata, N., Yamada, T., Kudo, A*., et al.* (2016). Ultrastable low-bias water splitting photoanodes via photocorrosion inhibition and in situ catalyst regeneration. Nat Energy *2*, 16191.
Kurtz, S., Haegel, N., Sinton, R., and Margolis, R. (2017). A new era for solar. Nat Photon *11*, 3-5.
Lee, D.K., and Choi, K.-S. (2017). Enhancing long-term photostability of BiVO4 photoanodes for solar water splitting by tuning electrolyte composition. Nat Energy.
Lewis, N.S. (2016). Research opportunities to advance solar energy utilization. Science *351*, aad1920.
Li, F., Bai, L., Li, H., Wang, Y., Yu, F., and Sun, L. (2016a). An iron-based thin film as a highly efficient catalyst for electrochemical water oxidation in a carbonate electrolyte. Chem Commun *52*, 5753-5756.

Li, N., Wang, Y., Tang, D., and Zhou, H. (2015a). Integrating a Photocatalyst into a Hybrid Lithium–Sulfur Battery for Direct Storage of Solar Energy. Angew Chem Int Ed *54*, 9271-9274.
Li, Q., Li, N., Ishida, M., and Zhou, H. (2015b). Saving electric energy by integrating a photoelectrode into a Li-ion battery. J Mater Chem A *3*, 20903-20907.
Li, Q., Li, N., Liu, Y., Wang, Y., and Zhou, H. (2016b). High-Safety and Low-Cost Photoassisted Chargeable Aqueous Sodium-Ion Batteries with 90% Input Electric Energy Savings. Adv Energy Mater *6*, 1600632-n/a.
Li, Q., Liu, Y., Guo, S., and Zhou, H. (2017). Solar energy storage in the rechargeable batteries. Nano Today *16*, 46-60.
Li, W., Fu, H.-C., Li, L., Cabán-Acevedo, M., He, J.-H., and Jin, S. (2016c). Integrated Photoelectrochemical Solar Energy Conversion and Organic Redox Flow Battery Devices. Angew Chem Int Ed *55*, 13104-13108.
Li, W., Fu, H.-C., Zhao, Y., He, J.-H., and Jin, S. (2018). 14.1% Efficient Monolithically Integrated Solar Flow Battery. Chem *4*, 2644-2657.
Liao, S., Zong, X., Seger, B., Pedersen, T., Yao, T., Ding, C., Shi, J., Chen, J., and Li, C. (2016). Integrating a dual-silicon photoelectrochemical cell into a redox flow battery for unassisted photocharging. Nat Commun *7*, 11474.
Liu, D., Wei, Z., Hsu, C.-j., Shen, Y., and Liu, F. (2014a). Efficient Solar Energy Storage Using A TiO2/WO3 Tandem Photoelectrode in An All-vanadium Photoelectrochemical Cell. Electrochim Acta *136*, 435-441.
Liu, D., Wei, Z., Shen, Y., Sajjad, S.D., Hao, Y., and Liu, F. (2015a). Ultra-long electron lifetime induced efficient solar energy storage by an all-vanadium photoelectrochemical storage cell using methanesulfonic acid. J Mater Chem A *3*, 20322-20329.
Liu, D., Zi, W., Sajjad, S.D., Hsu, C., Shen, Y., Wei, M., and Liu, F. (2015b). Reversible Electron Storage in an All-Vanadium Photoelectrochemical Storage Cell: Synergy between Vanadium Redox and Hybrid Photocatalyst. ACS Catal *5*, 2632-2639.
Liu, G., Shi, J., Zhang, F., Chen, Z., Han, J., Ding, C., Chen, S., Wang, Z., Han, H., and Li, C. (2014b). A Tantalum Nitride Photoanode Modified with a Hole-Storage Layer for Highly Stable Solar Water Splitting. Angew Chem Int Ed *53*, 7295-7299.
Liu, P., Cao, Y.l., Li, G.R., Gao, X.P., Ai, X.P., and Yang, H.X. (2013). A Solar Rechargeable Flow Battery Based on Photoregeneration of Two Soluble Redox Couples. ChemSusChem *6*, 802-806.
Liu, P., Yang, H.X., Ai, X.P., Li, G.R., and Gao, X.P. (2012). A solar rechargeable battery based on polymeric charge storage electrodes. Electrochem Commun *16*, 69-72.
Liu, Y., Li, N., Liao, K., Li, Q., Ishida, M., and Zhou, H. (2016). Lowering the charge voltage of Li-O2 batteries via an unmediated photoelectrochemical oxidation approach. J Mater Chem A *4*, 12411-12415.
Liu, Y., Li, N., Wu, S., Liao, K., Zhu, K., Yi, J., and Zhou, H. (2015c). Reducing the charging voltage of a Li-O2 battery to 1.9 V by incorporating a photocatalyst. Energy Envrion Sci *8*, 2664-2667.
Luo, W., Yang, Z., Li, Z., Zhang, J., Liu, J., Zhao, Z., Wang, Z., Yan, S., Yu, T., and Zou, Z. (2011). Solar hydrogen generation from seawater with a modified BiVO4 photoanode. Energy Envrion Sci *4*, 4046-4051.
Ma, Y., Kafizas, A., Pendlebury, S.R., Le Formal, F., and Durrant, J.R. (2016). Photoinduced Absorption Spectroscopy of CoPi on BiVO4: The Function of CoPi during Water Oxidation. Adv Funct Mater *26*, 4951-4960.

Ma, Y., Pendlebury, S.R., Reynal, A., Le Formal, F., and Durrant, J.R. (2014). Dynamics of photogenerated holes in undoped BiVO4 photoanodes for solar water oxidation. Chemical Science *5*, 2964-2973.
Mahmoudzadeh, M.A., Usgaocar, A.R., Giorgio, J., Officer, D.L., Wallace, G.G., and Madden, J.D.W. (2016). A high energy density solar rechargeable redox battery. J Mater Chem A *4*, 3446-3452.
Mase, K., Yoneda, M., Yamada, Y., and Fukuzumi, S. (2016). Seawater usable for production and consumption of hydrogen peroxide as a solar fuel. Nat Commun *7*, 11470.
Mayer, M.T. (2017). Photovoltage at semiconductor–electrolyte junctions. Current Opinion in Electrochemistry *2*, 104-110.
McCulloch, W.D., Yu, M., and Wu, Y. (2016). pH-Tuning a Solar Redox Flow Battery for Integrated Energy Conversion and Storage. ACS Energy Lett *1*, 578-582.
Montoya, J.H., Seitz, L.C., Chakthranont, P., Vojvodic, A., Jaramillo, T.F., and Nørskov, J.K. (2016). Materials for solar fuels and chemicals. Nat Mater *16*, 70-81.
Morales-Guio, C.G., Mayer, M.T., Yella, A., Tilley, S.D., Grätzel, M., and Hu, X. (2015). An Optically Transparent Iron Nickel Oxide Catalyst for Solar Water Splitting. J Am Chem Soc *137*, 9927-9936.
Nikiforidis, G., Tajima, K., and Byon, H.R. (2016). High Energy Efficiency and Stability for Photoassisted Aqueous Lithium–Iodine Redox Batteries. ACS Energy Lett *1*, 806-813.
Nocera, D.G. (2017). Solar Fuels and Solar Chemicals Industry. Acc Chem Res *50*, 616-619.
Pan, L., Kim, J.H., Mayer, M.T., Son, M.-K., Ummadisingu, A., Lee, J.S., Hagfeldt, A., Luo, J., and Grätzel, M. (2018). Boosting the performance of Cu2O photocathodes for unassisted solar water splitting devices. Nat Cat.
Paolella, A., Faure, C., Bertoni, G., Marras, S., Guerfi, A., Darwiche, A., Hovington, P., Commarieu, B., Wang, Z., Prato, M*., et al.* (2017). Light-assisted delithiation of lithium iron phosphate nanocrystals towards photo-rechargeable lithium ion batteries. Nat Commun *8*, 14643.
Pellow, M.A., Emmott, C.J.M., Barnhart, C.J., and Benson, S.M. (2015). Hydrogen or batteries for grid storage? A net energy analysis. Energy Envrion Sci *8*, 1938-1952.
Pilli, S.K., Furtak, T.E., Brown, L.D., Deutsch, T.G., Turner, J.A., and Herring, A.M. (2011). Cobalt-phosphate (Co-Pi) catalyst modified Mo-doped BiVO4 photoelectrodes for solar water oxidation. Energy Envrion Sci *4*, 5028-5034.
Pilli, S.K., Summers, K., and Chidambaram, D. (2015). Ni-Ci oxygen evolution catalyst integrated BiVO4 photoanodes for solar induced water oxidation. RSC Adv *5*, 47080-47089.
Qin, D.-D., Wang, T., Song, Y.-M., and Tao, C.-L. (2014). Reduced monoclinic BiVO4 for improved photoelectrochemical oxidation of water under visible light. Dalton Transactions *43*, 7691-7694.
Roger, I., Shipman, M.A., and Symes, M.D. (2017). Earth-abundant catalysts for electrochemical and photoelectrochemical water splitting. Nat Rev Chem *1*, 0003.
Rongé, J., Bosserez, T., Huguenin, L., Dumortier, M., Haussener, S., and Martens, J.A. (2015). Solar Hydrogen Reaching Maturity. Oil Gas Sci Technol – Rev IFP Energies nouvelles *70*, 863-876.
Sayama, K., Nomura, A., Zou, Z., Abe, R., Abe, Y., and Arakawa, H. (2003). Photoelectrochemical decomposition of water on nanocrystalline BiVO4 film electrodes under visible light. Chem Commun, 2908-2909.
Seabold, J.A., and Choi, K.-S. (2012). Efficient and Stable Photo-Oxidation of Water by a Bismuth Vanadate Photoanode Coupled with an Iron Oxyhydroxide Oxygen Evolution Catalyst. J Am Chem Soc *134*, 2186-2192.

Seitz, L.C., Chen, Z., Forman, A.J., Pinaud, B.A., Benck, J.D., and Jaramillo, T.F. (2014). Modeling Practical Performance Limits of Photoelectrochemical Water Splitting Based on the Current State of Materials Research. ChemSusChem *7*, 1372-1385.
Sharon, M., and Sinha, A. (1982). A rechargeable photo-electrochemical solar cell (saur viddyut kosh—III). Int J Hydrogen Energy *7*, 557-562.
Shinagawa, T., Ng, M.T.-K., and Takanabe, K. (2017). Electrolyte Engineering towards Efficient Water Splitting at Mild pH. ChemSusChem *10*, 4155-4162.
Sivula, K., and van de Krol, R. (2016). Semiconducting materials for photoelectrochemical energy conversion. Nat Rev Mat *1*, 15010.
Sun, K., Saadi, F.H., Lichterman, M.F., Hale, W.G., Wang, H.-P., Zhou, X., Plymale, N.T., Omelchenko, S.T., He, J.-H., Papadantonakis, K.M*., et al.* (2015). Stable solar-driven oxidation of water by semiconducting photoanodes protected by transparent catalytic nickel oxide films. Proc Natl Acad Sci *112*, 3612.
Um, H.-D., Choi, K.-H., Hwang, I., Kim, S.-H., Seo, K., and Lee, S.-Y. (2017). Monolithically integrated, photo-rechargeable portable power sources based on miniaturized Si solar cells and printed solid-state lithium-ion batteries. Energy Envrion Sci *10*, 931-940.
Wang, Z., Fan, F., Wang, S., Ding, C., Zhao, Y., and Li, C. (2016). Bridging surface states and current-potential response over hematite-based photoelectrochemical water oxidation. RSC Adv *6*, 85582-85586.
Wedege, K., Azevedo, J., Khataee, A., Bentien, A., and Mendes, A. (2016). Direct Solar Charging of an Organic–Inorganic, Stable, and Aqueous Alkaline Redox Flow Battery with a Hematite Photoanode. Angew Chem Int Ed *55*, 7142-7147.
Wei, Z., Liu, D., Hsu, C., and Liu, F. (2014). All-vanadium redox photoelectrochemical cell: An approach to store solar energy. Electrochem Commun *45*, 79-82.
Wei, Z., Shen, Y., Liu, D., Hsu, C., Sajjad, S.D., Rajeshwar, K., and Liu, F. (2016). Geometry-enhanced ultra-long TiO2 nanobelts in an all-vanadium photoelectrochemical cell for efficient storage of solar energy. Nano Energy *26*, 200-207.
Wei, Z., Shen, Y., Liu, D., and Liu, F. (2017). An All-vanadium Continuous-flow Photoelectrochemical Cell for Extending State-of-charge in Solar Energy Storage. Sci Rep *7*, 629.
Xu, J., Chen, Y., and Dai, L. (2015a). Efficiently photo-charging lithium-ion battery by perovskite solar cell. Nat Commun *6*, 8103.
Xu, X., Li, S., Zhang, H., Shen, Y., Zakeeruddin, S.M., Graetzel, M., Cheng, Y.-B., and Wang, M. (2015b). A Power Pack Based on Organometallic Perovskite Solar Cell and Supercapacitor. ACS Nano *9*, 1782-1787.
Yan, N.F., Li, G.R., and Gao, X.P. (2013). Solar rechargeable redox flow battery based on Li2WO4/LiI couples in dual-phase electrolytes. J Mater Chem A *1*, 7012-7015.
Yan, N.F., Li, G.R., Pan, G.L., and Gao, X.P. (2012). TiN Nanotube Arrays as Electrocatalytic Electrode for Solar Storable Rechargeable Battery. J Electrochem Soc *159*, A1770-A1774.
Yang, Z., Zhang, J., Kintner-Meyer, M.C.W., Lu, X., Choi, D., Lemmon, J.P., and Liu, J. (2011). Electrochemical Energy Storage for Green Grid. Chem Rev *111*, 3577-3613.
Yoshiro, Y., Makoto, O., Masato, I., and Hiroshi, H. (1983). A Photochemical Storage Battery with an n-GaP Photoelectrode. Bull Chem Soc Jpn *56*, 2873-2876.
Yu, M., McCulloch, W.D., Beauchamp, D.R., Huang, Z., Ren, X., and Wu, Y. (2015). Aqueous Lithium–Iodine Solar Flow Battery for the Simultaneous Conversion and Storage of Solar Energy. J Am Chem Soc *137*, 8332-8335.

Yu, M., McCulloch, W.D., Huang, Z., Trang, B.B., Lu, J., Amine, K., and Wu, Y. (2016). Solar-powered electrochemical energy storage: an alternative to solar fuels. J Mater Chem A *4*, 2766-2782.
Yu, M., Ren, X., Ma, L., and Wu, Y. (2014). Integrating a redox-coupled dye-sensitized photoelectrode into a lithium–oxygen battery for photoassisted charging. Nat Commun *5*, 5111.
Zhou, X., Liu, R., Sun, K., Papadantonakis, K.M., Brunschwig, B.S., and Lewis, N.S. (2016). 570 mV photovoltage, stabilized n-Si/CoOx heterojunction photoanodes fabricated using atomic layer deposition. Energy Envrion Sci *9*, 892-897.